THE STRUCTURE OF (NUCLEAR) GRAPHITE

FROM THE ATOMIC TO THE MACRO SCALES

THE STRUCTURE OF (NUCLEAR) GRAPHITE

FROM THE ATOMIC TO THE MACRO SCALES

Proefschrift

ter verkrijging van de graad van doctor
aan de Technische Universiteit Delft,
op gezag van de Rector Magnificus prof. ir. K.C.A.M. Luyben,
voorzitter van het College voor Promoties,
in het openbaar te verdedigen op woensdag 9 maart 2016 om 12:30 uur

door

Zhou ZHOU

Master in Materials Science & Engineering,
Tsinghua University, Beijing, China.

This dissertation has been approved by the

promotor: prof. dr. C. Pappas
copromotor: dr. W.G. Bouwman
copromoter: dr. H. Schut

Composition of the doctoral committee:

Rector Magnificus,	voorzitter
Prof. dr. C. Pappas,	Technische Universiteit Delft
Dr. W.G. Bouwman,	Technische Universiteit Delft
Dr. H. Schut,	Technische Universiteit Delft

Independent members:

Prof. dr. Z. Li	Tsinghua University
Prof. dr. E. Schlangen	Technische Universiteit Delft
Prof. dr. P. Mummery	University of Manchester
Dr. M. Heijna	Nuclear Research and consultancy Group
Prof. dr. E.H. Brück	Technische Universiteit Delft (reserve)

CONTENTS

i

1

INTRODUCTION

In thermal nuclear reactors, a self-sustaining nuclear chain reaction can be only achieved when the fast neutrons released during the fission reactions are slowed down or moderated into thermal neutrons. Commonly used moderators include regular/heavy water (H_2O/D_2O) and graphite (C). Graphite has been used as a neutron moderator in the first artificial nuclear reactor Chicago Pile 1 in 1942. Since then several types of graphite-moderated nuclear reactors have been developed, e.g., Magnox reactors and Advanced Gas-cooled Reactors (AGR) in UK. Based on the experience on the long term operation of these reactors, graphite presently is considered to be the material of choice as a moderator as well as a major structural component for the next generation Very High Temperature Reactors (VHTR).

Graphite is an ideal moderator material for nuclear reactors because it has low atomic mass, a high scattering cross section and a negligible absorption cross section for neutrons. It is one of the purest materials that can be manufactured at industrial scale. These features are necessary for efficient and successful moderation. In addition, graphite has excellent mechanical and physical properties, e.g., it does not melt and it retains its strength at high temperatures. Furthermore, it is easy to machine into complicated shapes.

In graphite-moderated nuclear reactors, the graphite core provides structural support and the channels for fuel, control rods and coolant flow. During the operation of these reactors, the neutron radiation leads to significant changes in the dimensional, physical and mechanical properties of the graphite. The behaviour of the irreplaceable graphite determines the lifetime of such reactors, so an accurate estimation and prediction of its performance is required for the design and safe operation of the nuclear plants. As the graphite behaviour is determined by its structure and irradiation conditions, e.g., dose, dose rate and temperature, it is thus essential to establish a link between the structure and behaviour of graphite.

Although single crystalline graphite has a well-understood layered crystal structure, for serving as material for structural components in a reactor it has some drawbacks. It has a week inter-layer binding (which makes it slippery) and shows a distinct undesired

anisotropic behaviour. Therefore, the material of choice should be polycrystalline and when used for nuclear applications this synthetic, high-purity polycrystalline graphite is denoted as nuclear graphite. Owing to its manufacturing process, it has a complex structure and the complexity refers to two main aspects: defects and disorder within the crystallites, and porosity structure containing cracks and pores with various sizes extending from the nanometre to the millimetre length scale between the crystallites.

To investigate (changes in) the complex structure, techniques such as X-ray diffraction (XRD) and scanning/transmission electron microscopy (SEM/TEM) are widely used. XRD is the most common method for studying the crystal structure of a material. However, correctly interpreting the XRD patterns of nuclear graphites is not trivial because of the inherent disorder, which can significantly affect the shape of the diffracted peaks. Electron microscopy techniques enable the investigation on the defects and porous structure. However, it is confined to surface layers and cannot offer a quantitative description for the bulk material, and therefore the interpretation of the results may not be applied directly to the graphite blocks inside a nuclear reactor. Due to these limitations, a comprehensive description of the complicated structure of nuclear graphite is still lacking.

In this work, the crystal structure of nuclear graphite has been investigated by both X-ray and neutron diffraction. The diffraction patterns have been analysed by a structural model which provides the ability to quantify the disorder in the atomic structure. In addition, the porous structure has been studied using several neutron techniques such as (spin-echo) small angle neutron scattering (SE)SANS and neutron imaging, since the high penetration capability of neutrons allows an investigation on the bulk material. The combination of these techniques provides new insights in the understanding of the graphite structure, and is expected to establish a link between the changes in structure and macroscopic behaviour of nuclear graphite.

This thesis presents the experimental findings and interpretations and is structured as follows.

Chapter 2 gives an introduction on the nuclear graphite. The dimensional changes caused by neutron irradiation in the atomic lattice, crystallites and polycrystalline bulk material, respectively, are briefly introduced as well.

Chapter 3 presents an introduction on the experimental methods used in this work, including X-ray/neutron diffraction, (spin echo) small angle neutron scattering and neutron imaging. These techniques provide complementary structural information at different length scales.

Chapter 4 presents an X-ray diffraction study of the atomic structure of (nuclear) graphite. The XRD patterns have been interpreted using a structural model, which takes into account the effects of disorder and the penetration depth of X-rays. In this way a comprehensive quantitative description of the atomic structure is achieved. The same methodology has been successfully applied in a study on the neutron irradiated graphites, which is described in Chapter 5. It allows for the first time to quantify the effect of irradiation damage on the atomic structure of graphite investigated by X-ray diffraction. To complement the XRD results, neutron diffraction studies on graphite samples are presented and interpreted in Chapter 6.

Chapter 7 presents a comprehensive study combining SANS, SESANS and neutron

imaging. The experimental findings from these different techniques are interpreted by a fractal model revealing a fractal nature of graphite over an extraordinary broad range of 6 orders of magnitude in length from microscopic to macroscopic length scales.

<div align="right">

2

</div>

NUCLEAR GRAPHITE

2.1. STRUCTURE AND MANUFACTURING

Nuclear graphite is a polycrystalline material consisting of a large number of crystallites. The ideal crystal structure of the crystallites consists of graphene layers, in which the carbon atoms are arranged in a honeycomb network, as shown in Fig. 2.1(a) and (b). Stacking of these layers in the ...ABAB... sequence results in a hexagonal unit cell with dimensions $a = 2.461$ Å and $c = 6.708$ Å. Within the plane, each atom is covalently bonded to three others, while between layers only weak van der Waals interactions are present. Because of this, some of the basal planes may slip out of the perfect alignment and so-called stacking faults are introduced. These may lead to an ABC stacking sequence (i.e. rhombohedral graphite phase, see Fig. 2.1(c)) or to more complex turbostratic disorder caused by random shifts or rotations between adjacent layers.

**(a)**   **(b)**   **(c)**
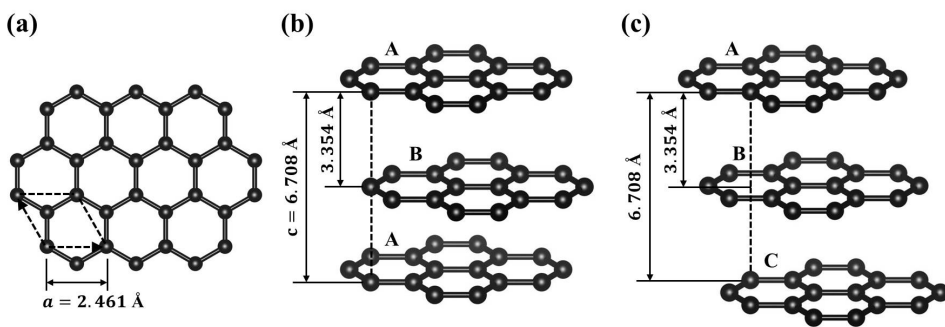
Figure 2.1: Crystal structure of graphite. (a) A graphene layer with carbon atoms arranged in a honeycomb network. The layers are stacked (b) in the ABAB sequence or (c) in the ABCABC sequence.

It also should be noted that the layered crystal structure exhibits high anisotropy, e.g., the thermal expansion coefficient is very anisotropic. It is high and positive along
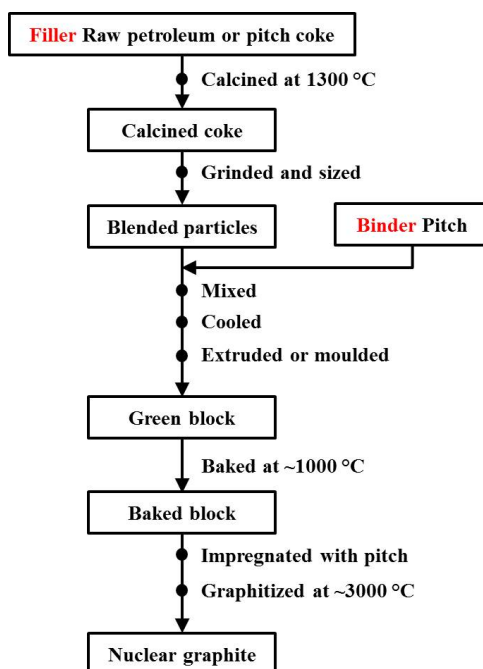
Figure 2.2: Manufacturing process of nuclear graphite.

the *c*-axis. However, it is low and negative in the planes from room temperature to about 500°C, and the value becomes slightly positive at higher temperatures.

Nuclear graphite has a complex microstructure owing to its manufacturing process, as shown in Fig. 2.2. It is mainly produced from a coke filler and pitch binder. The coke (usually petroleum coke) is an easily graphitized material and forms the primary component, while the pitch (usually coal tar pitch) is used to bind the coke particles. After the filler and binder are mixed, so-called green blocks are formed by either extrusion or moulding. The forming methods affect the orientation of the grains and thus the isotropy of the bulk material. During the extrusion process the elongated filler coke particles are aligned with their longitudinal axis parallel to the extrusion direction. On the other hand, the anisotropy in the moulded graphite is generally less than that found in the extruded graphite. Since isotropic graphite has high dimensional stability under neutron irradiation, the spherical coke particles are preferred for developing nuclear graphite (e.g. Gilsonite graphites). Therefore recent forming methods such as isostatic moulding and vibration moulding are preferably used for manufacturing isotropic graphite. After a green block is baked at ~ 1000°C, it is one or more times impregnated with pitch to reduce the porosity, thereby increasing the bulk density. Next the material is graphitized at ~3000°C. During this essential step most of the hydrogen is removed. Further it invokes crystal growth and the annealing of crystallite imperfections.

Due to the choice of raw materials and manufacturing process, nuclear graphite contains a large volume of pores and cracks with various shapes and sizes spanning from
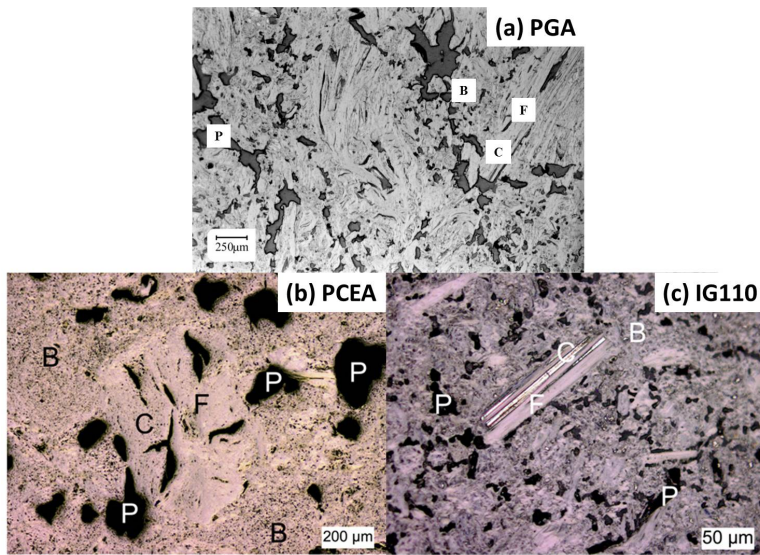
Figure 2.3: Optical micrographs of (a) PGA (after [1]), (b) PCEA (after [2]) and (c) IG110 (after [2]). F-filler, B-binder, P-pores and C-cracks.

several nanometres to hundreds of micrometres. The complex microstructure can be explored by optical microscopy, as shown in Fig. 2.3 [1, 2]. The elongated filler particles are surrounded by the binder. The large pores present in the binder are formed by gas evolution during the heating treatments. The cracks in the filler are result of shrinkage during cooling after the graphitization treatment. These cracks are mainly parallel to the crystallites basal planes because of the high thermal expansion coefficient along *c*-axis leading to a large contraction during cooling. In addition, there are also regions of amorphous carbon containing micropores in the filler particles [3], as shown in Fig. 2.4.
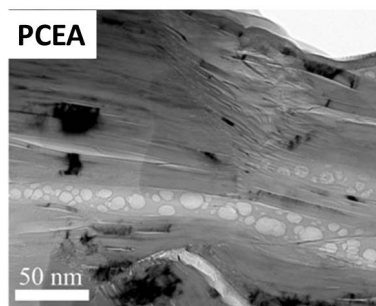
Figure 2.4: (after [3]) TEM micrograph of a filler particle with cracks filled with porous amorphous carbon in PCEA graphite.

2.2. IRRADIATION EFFECTS ON NUCLEAR GRAPHITE

ATOM DISPLACEMENT

During reactor operation, the fast neutrons slow down to thermal energies through collisions with the carbon atoms of nuclear graphite. In this moderation process a large number of atoms are displaced leading to irradiation defects on the graphite structure.

A schematic of the mechanism of atom displacement is illustrated in Fig. 2.5 [4]. The initial collision displaces a carbon atom, which is referred to as the primary knock-on atom (PKA). This high energy PKA travels through the lattice and may displace further atoms producing a number of secondary displacement groups (SDG). Although some of the displaced atoms will recombine with nearby vacant lattice cites, interstitials and vacancies are produced by the collision cascade.
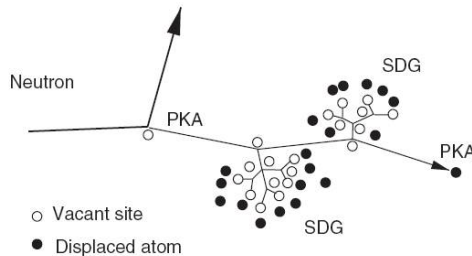

Figure 2.5: (after [4]) Schematic of the mechanism of atoms displacement due to fast neutrons. The initial collision creates the primary knock-on atom (PKA) leading to the secondary displacement groups (SDG).

STRUCTURAL CHANGES DUE TO IRRADIATION

The interstitial and vacancy defects created during irradiation can behave independently or may coalesce into interstitial or vacancy clusters which may consequently deform the crystal lattice leading to structural changes of graphite. Typically, the in-plane lattice parameter a decreases while the interlayer spacing c increases, as shown in Fig. 2.6 [5]. These changes are temperature dependent and tend to increase with dose and saturate at high dose levels.

Besides the changes in lattice, the carbon atom displacements result in dimensional change of the graphite crystals. The interstitials between carbon layers lead to crystallite growth along the c-axis, whereas coalescence of in-plane vacancies will cause a shrinkage along a-axis [6–10], as illustrated in Fig. 2.7.

Nuclear graphite is a polygranular material exhibiting a polycrystalline structure. This implies that its dimensional changes are a result of the overall effect of the dimensional change of the individual crystallites and the complex microstructure. As already mentioned, in the bulk material the cracks formed by thermal shrinkage are parallel to the basal planes. These cracks initially accommodate the expansion along c-axis, so mainly the shrinkage along a-axis can be observed. This behaviour is illustrated by the data from H451 nuclear graphite, as shown in Fig. 2.8 [10]. H451 is an extruded graphite, and thus the crystallographic a-axis of crystallites in coke particles is preferentially aligned parallel to the extrusion direction. Consequently the shrinkage of the
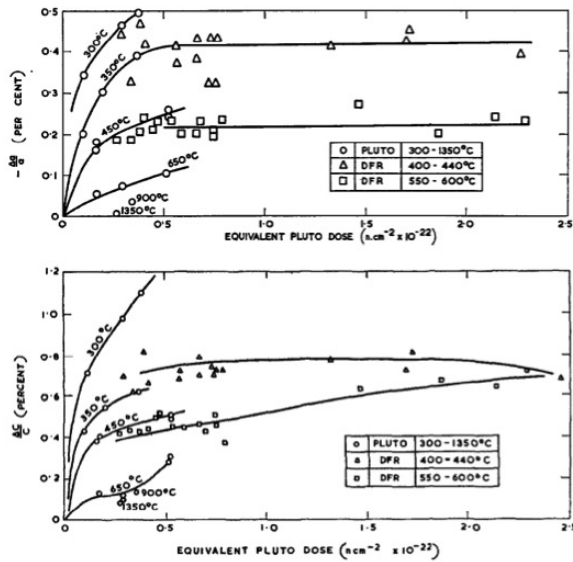
Figure 2.6: (after [5]) Changes in lattice constant (a) *a* and (b) *c* as a function of equivalent dose.
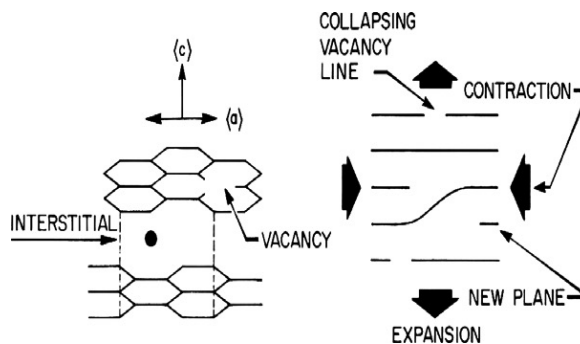
Figure 2.7: (after [10]) The mechanism of neutron irradiation damage induced crystal dimension changes.

bulk graphite parallel to the extrusion direction is more prominent. As the irradiation dose increases, a large fraction of accommodation porosity is closed, and new pores are generated. Consequently, the shrinkage rate falls, and eventually the graphite begins to swell.

2.3. SAMPLES

In this thesis, several nuclear graphites have been studied and they will be introduced below.

Pile Grade A (PGA) graphite was used in the early gas-cooled Magnox reactors in UK, and manufactured by British Acheson Electrodes, Ltd. and Anglo Great Lakes. It was
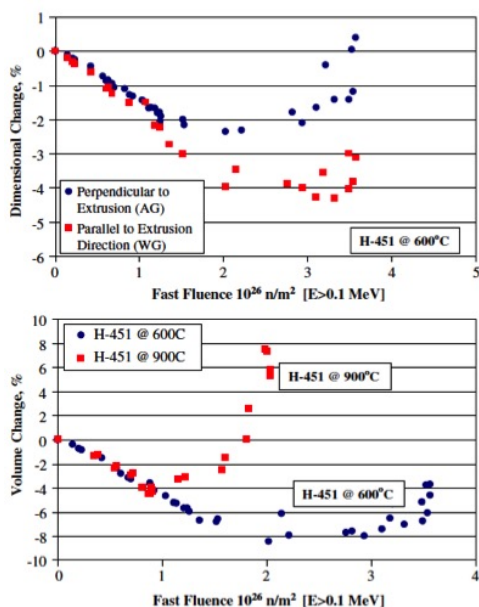
Figure 2.8: (after [10]) Dimensional change behaviour of H451 graphite.

produced from elongated needle shaped coke derived from the petroleum industry. The filler particles tended to be aligned by extrusion process, and the bulk material is thus anisotropic.

PCEA graphite is a candidate for the very high temperature reactor in USA and manufactured by GrafTech. It is an nearly-isotropic produced from petroleum coke source by extrusion.

RID graphite was used at the Reactor Institute Delft to optimize thermal neutron yield and manufactured by Pechiney SA in the 1960's. It was produced by baking a paste made of oil coke and pitch, graphitized by electrical heating.

IG110 graphite is currently used in HTGR reactors in Japan and manufactured by Toyo Tanso. It is a fine-grained isotropic graphite from petroleum coke formed by isostatic pressing.

1940 PT is a high-density(non-nuclear)graphite with very fine grains manufactured for refractory applications.

REFERENCES

[1] P. J. Hacker, G. B. Neighbour, and B. McEnaney, *The coefficient of thermal expansion of nuclear graphite with increasing thermal oxidation,* J. Phys. D: Appl. Phys **33**, 991 (2000).

[2] J. Kane, C. Karthik, D. P. Butt, W. E. Windes, and R. Ubic, *Microstructural characterization and pore structure analysis of nuclear graphite,* J. Nucl. Mater. **415**, 189 (2011).

[3] C. Karthik, J. Kane, D. P. Butt, W. E. Windes, and R. Ubic, *Microstructural characterization of next generation nuclear graphites,* Microsc. Microanal. **18**, 272 (2012).

[4] R. H. Telling and M. I. Heggie, *Radiation defects in graphite,* Philosophical Magazine **87**, 4797 (2007).

[5] R. W. Henson, A. J. Perks, and J. H. W. Simmons, *Lattice Parameter and Dimensional Changes in Graphite Irradiated between 300 and 1350 Degrees C,* Carbon **6**, 789 (1968).

[6] B. T. Kelly, W. H. Martin, and P. T. Nettley, *Dimensional Changes in Pyrolytic Graphite under Fast-Neutron Irradiation,* Philosophical Transactions of the Royal Society A: Mathematical, Physical and Engineering Sciences **260**, 37 (1966).

[7] B. Kelly and J. Brocklehurst, *High dose fast neutron irradiation of highly oriented pyrolytic graphite,* Carbon **9**, 783 (1971).

[8] P. R. Goggin, R. W. Henson, A. J. Perks, and W. N. Reynolds, *Dimensional changes in the irradiated graphite lattice,* Carbon **1**, 189 (1964).

[9] B. Kelly, *The theory of irradiation damage in graphite,* Carbon **15**, 117 (1977).

[10] T. D. Burchell and L. L. Snead, *The effect of neutron irradiation damage on the properties of grade NBG-10 graphite,* Journal of Nuclear Materials **371**, 18 (2007).

3

METHODS USED IN THIS WORK

In the work described in this thesis, several techniques including X-ray/Neutron diffraction, (spin echo) small angle neutron scattering and neutron imaging, are used to investigate the structure of (nuclear) graphite samples. Each technique probes the structural information on different length scale, as shown in Fig. 3.1. The combination of these techniques enable a comprehensive investigation covering 8 orders of magnitude in the length scale.
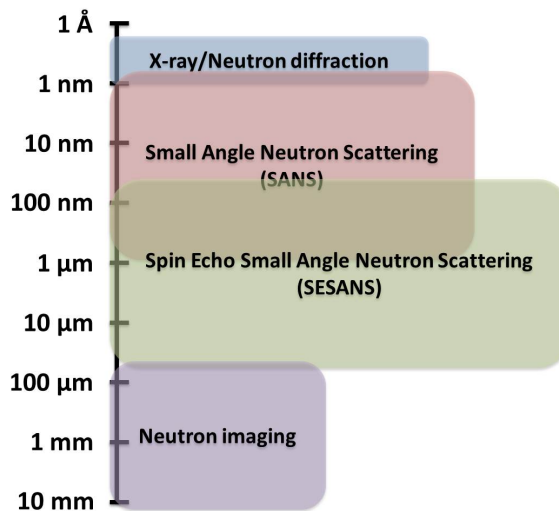
Figure 3.1: Typical length scales covered by the experimental techniques used in this thesis research.

All the characterization techniques are based on the interaction of neutrons (X-rays) with matter. Since neutrons have no electrical charge, they only interact with the nucleii. Given the fact that the space in matter is mostly occupied by the electron clouds,

13
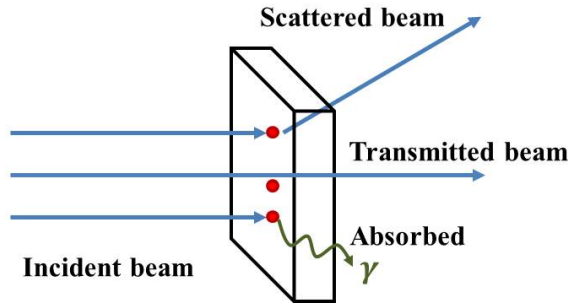
Figure 3.2: Illustration of neutron-matter interactions.

neutrons thus have high penetration capacity. When a neutron beam is directed into a sample, a large fraction of the neutrons may pass through with no interactions, and some may be scattered or absorbed, as illustrated in Fig. 3.2. The probability for each of these events is given by cross sections of specific elements and isotopes in the sample. In neutron-based techniques, the scattered or transmitted beam is measured to provide information about the structure of materials.

3.1. ELASTIC NEUTRON SCATTERING TECHNIQUES

As schematically shown in Fig. 3.3, when a monochromatic neutron beam (with wavelength λ) is scattered elastically (no energy transfer), the scattering vector $\boldsymbol{Q}$ is given by $\boldsymbol{Q} = \boldsymbol{k'} - \boldsymbol{k}$ with $Q = 4\pi \sin\theta/\lambda$. Here 2θ is the scattering angle; $\boldsymbol{k} = 2\pi/\boldsymbol{\lambda}$ is the wavevector of the incident neutrons and $\boldsymbol{k'}$ is that of the scattered neutrons and $k = k'$. In most elastic neutron scattering techniques (diffraction and small angle scattering), the intensity of scattered beam as a function of the scattering vector Q is measured by a detector.
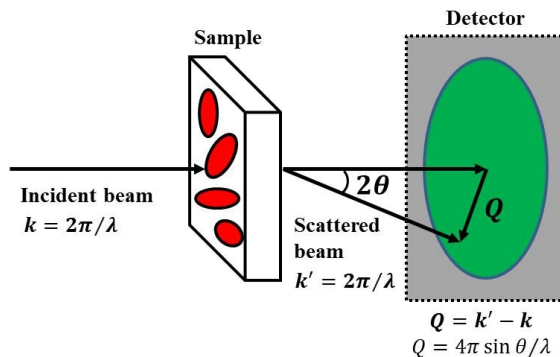
Figure 3.3: Schematic representation of the elastic neutron scattering.
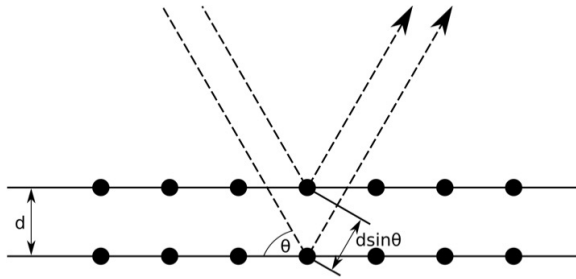
Figure 3.4: Schematic of Bragg's law.

3.1.1. X-ray/Neutron diffraction

X-ray/Neutron diffraction is a standard method to investigate the atomic structure of materials. The basic principle of this methodology can be explained by Bragg's law, as illustrated in Fig. 3.4. X-rays/neutrons are scattered by lattice planes, and interfere constructively only when the path difference between reflected waves is an integral multiple of the incident beam wavelength λ:

$$2d\sin\theta = n\lambda \tag{3.1}$$

where d is the distance between lattice planes, θ is the incidence/scattering angle, and n is an integer. Thus diffraction peaks on the diffraction pattern at specific angles reveal the periodic arrangement of atoms in a crystal.
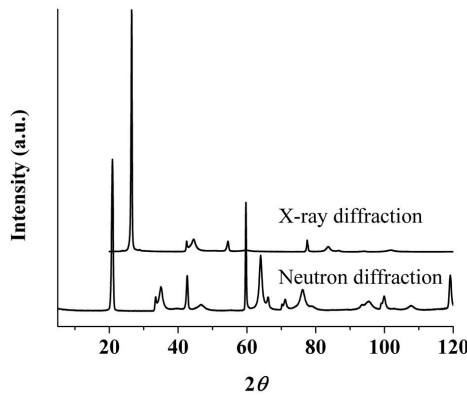
Figure 3.5: X-ray and neutron diffraction patterns from PCEA nuclear graphite.

Fig. 3.5 shows X-ray and neutron diffraction patterns from a PCEA graphite sample, in which the peaks positions are shifted due to the different wavelengths of X-rays and neutrons used. In addition, the intensity of X-ray diffraction falls off at high scattering angle. This is because the scattering power of an atom for X-rays (i.e. atomic form factor) decreases with increasing scattering angle. On the other hand, the neutron scattering

strength (given by the scattering length) of an atom is a property of the nucleus and thus does not vary with the scattering angle.

3.1.2. SMALL ANGLE NEUTRON SCATTERING (SANS)

In the diffraction experiment, the elastic scattering at a scattering vector $Q = 4\pi \sin\theta/\lambda$ results from periodic modulations of the neutron scattering lengths with period $d = 2\pi/Q$, where d is interpreted as the distance between lattice planes. To measure structures that are larger than typical interatomic distances, smaller Q is required either by increasing the neutron wavelength λ, or by decreasing the scattering angle 2θ. The technique measuring elastic scattering at small angles to examine larger structures is known as small angle neutron scattering (SANS). The typical range of Q covered is from about 0.005 to 0.5 Å^{-1}, corresponding to a range in real space ($= 2\pi/Q$) from 10 to 1000 Å. In this case, SANS is not directly related to the scattering from individual planes of atoms as diffraction is. Instead, the scattering takes place from aggregates of atoms (e.g. molecules) and thus the inhomogeneities of scattering length densities over that range are measured. In many cases, samples measured by SANS can be considered to consist of "particles" (with a constant scattering length density) dispersed in a uniform medium (with another constant scattering length density), as shown the illustration in Fig. 3.3; an example is the presence of pores in graphite. The measured intensity of the scattered beam $I(Q)$, i.e. the scattering cross section, as a function of the scattering vector Q is given by:

$$I(Q) \propto P(Q)S(Q), \tag{3.2}$$

where $P(Q)$ is the so-called form factor characterizing the morphology/shape of the particles, and $S(Q)$ is the structure factor reflecting the correlations between the particles.

3.1.3. SPIN ECHO SMALL ANGLE NEUTRON SCATTERING (SESANS)

As already mentioned, measuring large structures involves small $Q's$. To measure the elastic scattering at smaller angles in a conventional SANS set-up requires a highly collimated incident neutron beam, which will lead to a great loss in intensity. In order to overcome this trade-off between high resolution in Q and beam intensity, the spin echo small angle neutron scattering technique has been developed. This method is based on the Larmor precession of polarized neutrons in a magnetic field, which encodes the scattering angle of neutrons through a precession device. This technique has several advantages: large length scales up to 20 μm can be reached; high intensity of the beam because collimation is not needed; multiple scattering can be easily taken into account. Unlike SANS which measures the scattering intensity as a function of scattering vector Q, SESANS measures a function in real-space.

In a SESANS experiment, the incoming neutrons are polarized and the polarization echo can be broken down by the scattering leading to depolarization. The resulting polarization P_S, which is related to the scattering length density correlation function, is then measured as a function of the spin echo length z, a length scale in real space over which the correlations are measured, as shown the example measurements in Fig. 3.6.
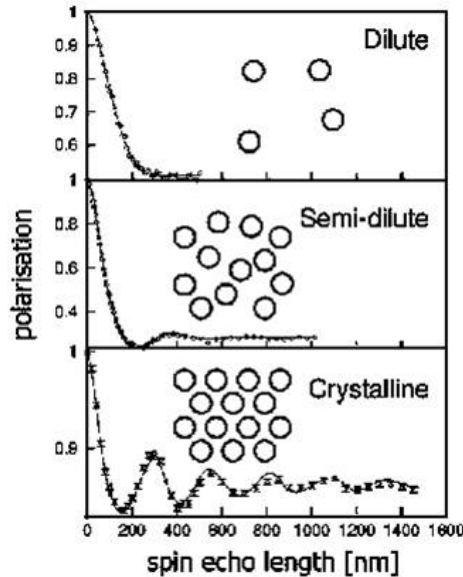
Figure 3.6: (after [1]) Example SESANS measurements on a solution prepared with three concentrations: (i) dilute, (ii) semi-dilute and (iii) concentrated (behaves like a crystalline). The results indicate that the correlations in the sample are measured by SESANS.
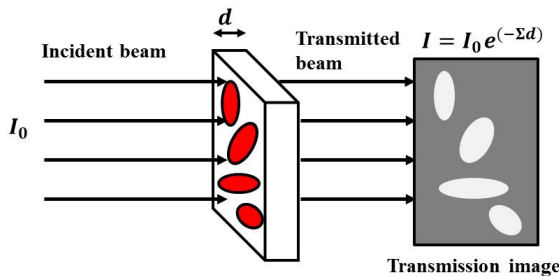
Figure 3.7: Illustration of the attenuation of an incident neutron beam by a sample.

3.2. NEUTRON IMAGING

Besides the elastic neutron scattering techniques, neutron imaging has been used in this work to provide structural information at length scales from tens of micrometres to millimetres. This technique is based on the neutron attenuation properties of the imaged object in the sample. As shown in Fig. 3.7, the incident neutron flux I_0 is attenuated by the sample with a thickness of d, resulting the transmitted neutron flux given by $I = I_0 \exp(-\Sigma d)$, where Σ is the macroscopic cross section describing the attenuation capability of the material. Since different materials vary in their ability to attenuate neutrons through both scattering and absorption, the resulting image thus visualises the

internal materials or components and their structure. Instead of the monochromatic neutron beam needed for elastic scattering methods, the white beam is used for the attenuated-based neutron imaging technique.

REFERENCES

[1] T. Krouglov, W. G. Bouwman, J. Plomp, M. T. Rekveldt, G. J. Vroege, A. V. Petukhov, and D. M. E. Thies-Weesie, *Structural transitions of hard-sphere colloids studied by spin-echo small-angle neutron scattering,* Journal of Applied Crystallography **36**, 1417 (2003).

4

INTERPRETATION OF X-RAY DIFFRACTION PATTERNS OF (NUCLEAR) GRAPHITE

The atomic structure of several nuclear graphite samples, an essential moderator material for nuclear reactors, has been investigated by X-ray diffraction. The patterns were analyzed by the conventional Rietveld refinement approach as well as by the CARBONXS model, which takes into account disorder and stacking faults. The refined parameters compiled with those from literature reveal a generic picture for the structure of all graphite specimens.

4.1. Introduction

Since the world's first man-made nuclear reactor, Chicago Pile 1 in 1942, several types of graphite moderated nuclear reactors have been developed. Graphite is a good moderator because it has low atomic mass, a high scattering cross section and a negligible absorption cross section for neutrons [2]. In addition graphite has excellent mechanical and physical properties, e.g. it does not melt, which make it a perfect choice for moderating neutrons in the very high temperature reactor (VHTR) or the high temperature gas-cooled Generation IV reactor (HTGR). For the safe operation of these reactors it is important to understand this moderator material with the aim of being able to predict and control the changes occurring under long term irradiation [3].

Nuclear graphite is a complex polygranular system, with a very high chemical purity and a high degree of graphitization due to its specific application requirement [4]. The crystal structure consists of series of layers of carbon atoms, which form the 2D hexagonal network of graphene layers. These layers are stacked either in the ABAB sequence leading to the hexagonal 2H structure or in the ABCABC arrangement for the rhombohedral 3R structure. Normally, highly ordered or highly oriented graphite has the 2H hexagonal structure but even high quality samples still contain a non-negligible fraction of the 3R rhombohedral phase [5–7]. This is because graphite cannot be produced out of the melt at ambient pressure.

X-ray diffraction (XRD) is the standard method for investigating the microscopic structure of bulk graphite. The analysis of XRD patterns, however, is not trivial because the Bragg peaks are asymmetric and broad due to several factors, such as the high penetration depth of X-rays, the fluctuations in lattice spacing and the stacking disorder between the carbon layers. The combination of these effects has not always been taken into account properly. In particular, earlier studies [6–16] focused only on the influence of the stacking faults and random shifts between adjacent carbon layers. This disordered layered structure was described by the term "turbostratic" and it was supposed that graphite contains nearly perfect segments of carbon layers, but without correlation between adjacent layers. The relative displacements between layers were assumed to be translations or rotations with the resulting strains leading to fluctuations of interlayer spacing.

Other studies focused on the influence of the high penetration depth of X-rays on both the positions and widths of the Bragg peaks. For this purpose samples consisting of a mixture of graphite and silicon powders were measured [17–20]. The graphite Bragg peak positions and widths were then corrected on the basis of the effects found for silicon. From these studies it became clear that the broadened diffraction patterns cannot be solely attributed to the penetration depth of X-rays, because in this case non-physical results such as interlayer spacing and crystallite size that depend on the specific diffraction line used are obtained [18].

It is therefore obvious that a correct analysis of graphite XRD patterns must include both disorder and the high penetration of X-rays. However, disorder in graphite is complex due to the inherent anisotropy of the layered structure, with strong covalent bonding in the (graphene) layers and weak van der Waals interactions between the layers. For this reason the standard Rietveld refinement [21], which implicitly assumes isotropic crystallite size, perfect tri-periodicity and disorder at atomic scale, cannot properly re-
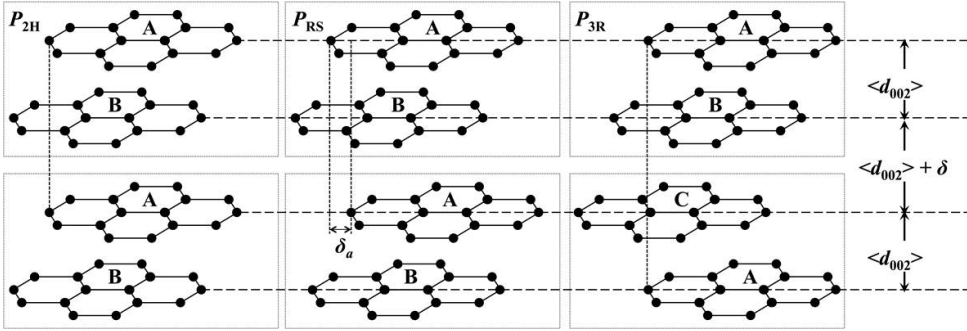
Figure 4.1: Schematic drawing of three stacking sequences of hexagonal carbon planes characteristic graphite structure. The dotted squares illustrate the two-layer units assumed by the model of Shi et al [25]. The parameter δ is defined as $\delta = d_{002} - \langle d_{002} \rangle$ and can take positive or negative values (see text). The parameter δ_a is related to the probability of random shift stacking faults P_{RS} (see text).

produce the observed broadening and intensities of the Bragg peaks and fails in giving reliable structural information [22–24]. In order to overcome these limitations Shi introduced a structural model that incorporates disorder and the anisotropy of the graphite structure [25, 26]. This model has been successfully applied to both X-ray and neutron diffraction patterns of carbon materials. It will be introduced in the following section and will be used to analyze our XRD patterns of nuclear graphite. The resulting refined parameters reveal a generic picture for the structural properties of all graphites including nuclear graphites.

4.2. THE DISORDERED GRAPHITE MODEL CARBONXS

Shi considered a two-layer model to describe the structure of graphitic carbon. In this model an ideal and rigid AB stacking sequence forms a primary building block of the structure as illustrated by Fig. 4.1. Then the blocks are stacked as follows:

1. a random shift between adjacent blocks with probability P_{RS}, accounting for the stacking faults with a random translational component in basal plane;

2. a registered shift between adjacent blocks leading to a local 3R rhombohedral order with probability P_{3R}, describing the ABC stacking faults with a fixed translational component;

3. no shift at all between adjacent blocks with probability $P_{2H} = 1 - P_{3R} - P_{RS}$, giving the 2H ABAB order.

Obviously, for $P_{RS} = 0$, $P_{3R} = 0$, $P_{2H} = 1$, this model produces the 2H ABAB stacking sequence of perfect graphite, whereas when $P_{RS} = 0$, $P_{2H} = 0$, $P_{3R} = 1$, a perfect rhombohedral 3R ABCABC sequence is obtained.

As already mentioned, the stacking faults result in strains and thus fluctuations of the interlayer spacing, which lead to a broadening of all (00l) peaks. The model assumes a Gaussian distribution of the lattice parameter along the c-axis around the mean value

$\langle d_{002} \rangle$ as illustrated by Fig. 4.1, with $\delta = d_{002} - \langle d_{002} \rangle$ and characterized by the standard deviation $\sigma = \sqrt{\langle \delta \rangle^2}$:

$$P(\delta) = \frac{1}{\sqrt{2\pi} \exp(-\delta^2/2\sigma^2)} \qquad (4.1)$$

According to [16, 22], the probability of random shift stacking faults $P_{[RS]}$ is directly related to δ_a, the fluctuations of the in-plane lattice constant a, through the Gaussian:

$$1 - P_{RS} = \exp[-2(\frac{\delta_a}{\langle a \rangle/2\pi})^2] \qquad (4.2)$$

This expression appears slightly different from the one in [22] because here the d_{110} is substituted by $\langle a \rangle/2$. Note that because of the presence of the fluctuations in the in-plane lattice parameter a, we have used $\langle a \rangle$ to make it consistent with $\langle d_{002} \rangle$.

Besides the average lattice constants $\langle d_{002} \rangle$ along the c-axis and $\langle a \rangle$ for the hexagonal network in the planes, the model introduces two different characteristic lengths, one along the c-axis L_c and one in the plane L_a, to quantify the volumes over which X-rays (or neutrons) are diffracted coherently. This assumption is justified by the anisotropy of the graphite structure and thus offers additional flexibility as compared to the Rietveld method, which provides only one average crystallite size. We note that the coherent lengths (crystallite size), which are calculated from the widths of the diffraction peaks, are often confused with the grain size. Indeed the coherent lengths are typically of the order of several nanometres, whereas the grain size seen by optical or electron microscopy is several orders of magnitudes larger, typically of the orders of tens of micrometers (see e.g. Table 1). Thus, as pointed out in [24] and illustrated by Fig. 4.2 (after [13]), each grain consists of many small coherent volumes characterized by the average sizes L_a and L_c. From L_c and $\langle d_{002} \rangle$ one can deduce $M = L_c/\langle d_{002} \rangle$, the average number of layers stacking in the coherent regions.

This structural model introduced above had been incorporated in a refinement program CARBONXS by Shi and coworkers. In addition to the parameters of the model, CARBONXS also includes corrections for the X-ray polarization, the Lorentz factor, preferred sample orientation and an isotropic temperature (Debye-Waller) factor. The effect of the high penetration depth of X-rays on the peak positions and shapes is accounted for by convoluting the patterns with a function, which includes absorption and sample size.

4.3. EXPERIMENTAL

The XRD measurements in this work were done with a Panalytical X'pert Pro diffractometer in the Bragg-Brentano $\theta - \theta$ geometry using X-ray radiation from a Cu anode (45 kV, 40 mA, $\lambda = 1.54187$ Å). The XRD patterns for 2θ from 20 to 120° were collected in continuous-scanning mode with interval of 0.02° at a speed of 3°/min. All measurements were done using the same configuration and all samples had a disk-shape with dimensions of ϕ 20 mm × 2.0 mm cut from the respective raw block materials. The resolution function for this configuration was derived from the refinement of a standard LaB$_6$ sample. This resolution function was included in the instrument parameter file for GSAS fitting. We investigated 4 different nuclear graphites (PGA, PCEA, IG110 and RID) and a non-nuclear graphite (1940 PT) as a reference.
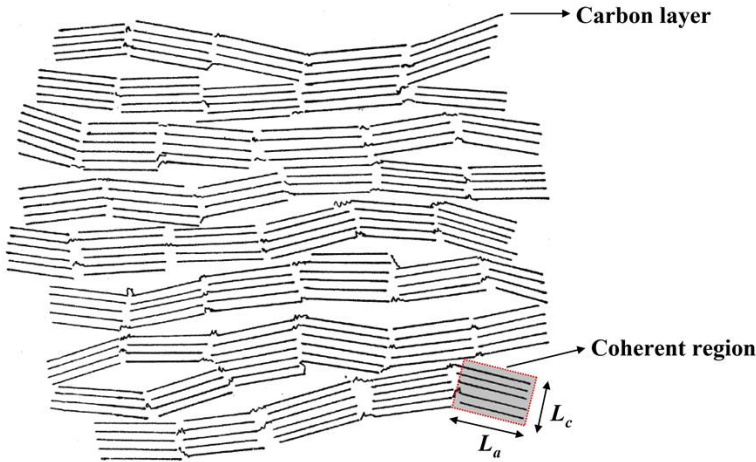
Figure 4.2: (after [14]): Schematic representation of the disordered stacking of layers within a grain of graphite illustrating the existence of coherent regions, the extend of which is characterized by the coherent lengths L_a and L_c.

1. **PGA** manufactured using filler particles derived from the petroleum industry and used in the early gas-cooled reactors in UK.

2. **PCEA** manufactured by GrafTech from petroleum coke by extrusion, a candidate for the Very High Temperature Reactor in USA.

3. **IG110** a near-isotropic grade nuclear graphite produced by isostatic molding based on fine petroleum coke manufactured by Toyo Tanso Ltd. and currently used in the Japanese High Temperature Test Reactor.

4. **RID** manufactured by Pechiney SA in the 1960's and used at the Reactor Institute Delft to optimize thermal neutron yield.

5. **1940 PT** a high-density (non-nuclear) graphite with very fine grains manufactured for refractory applications.

The bulk density and grain size of these graphites are listed in Table 1. For all samples, except the RID graphite, the values are copied from the product sheets of the manufacturing companies. The density of the RID samples was deduced from their mass over volume ratio. This method was also used to confirm the densities given by the manufacturers for all other graphites.

Due to disorder and inhomogeneity, each graphite sample is unique. Thus two samples from the same original material may exhibit slightly different structural and physical properties [27]. It has even been suggested that no two graphite samples would ever have identical X-ray diffraction patterns in every detail. In order to increase the reliability of the XRD results, and also take into account systematic errors, at least two samples

Table 4.1: Characteristics of nuclear graphite used for this study.

Graphite grade	Bulk density (g/cm^3)	Grain size
PGA	1.74	0.1-1 mm
PCEA	1.79	0.4 mm (Max. 0.8 mm)
RID	1.64	-
IG110	1.77	20 μm (Max. 0.04 mm)
1940 PT	1.80	15 μm
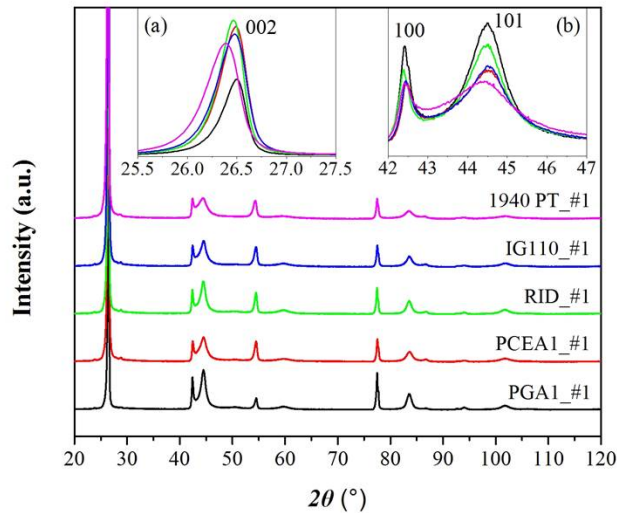
Figure 4.3: Measured X-ray diffraction patterns of five representative graphite samples studied in this work.

for each type of graphite were measured and for PGA and PCEA manufactured by extrusion, several samples were cut in two different directions (along or perpendicular to the extrusion direction).

4.4. RESULTS

Fig. 4.3 displays measured X-ray diffraction patterns of five representative graphite samples (PGA1_#1, PCEA1_#1, RID_#1, IG110_#1 and 1940 PT_#1), from which no significant differences can be observed visually. However, as shown in the inserts (a) and (b), the (002) peaks of the nuclear graphites occur at higher diffraction angles than of 1940 PT. In addition, the nuclear graphites show sharper (101) peaks. Both effects indicate that the nuclear graphites studied in this work have a different structure than 1940 PT.

The XRD patterns were analyzed by both the standard Rietveld refinement program GSAS and CARBONXS. Fig. 4.4 shows the X-ray diffraction patterns of PGA1_1# fitted by (a) GSAS based on the standard 2H structure with ABAB sequence and (c) the program
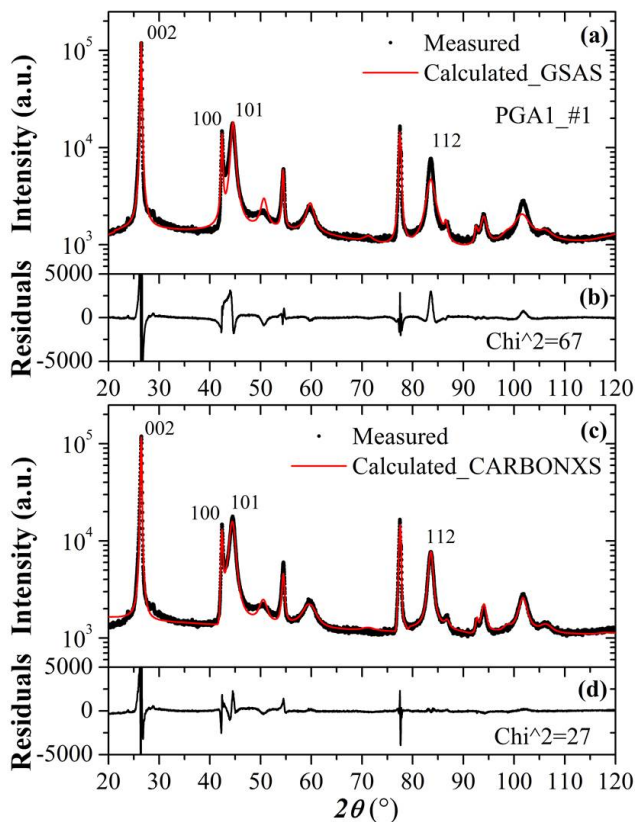
Figure 4.4: Measured and calculated X-ray diffraction patterns of PGA. The data were fitted using (a) Rietveld refinement method and the program GSAS and (c) Shi's model and the program CARBONXS. The residuals between measured and calculated intensities are given in (b) and (d) for GSAS and CARBONXS respectively.

CARBONXS. GSAS does not properly reproduce the measured peaks e.g. (100/101) and (112), which are characteristic of stacking disorder. This is illustrated by the residuals shown in Fig 4.4(b).

A major improvement is achieved by CARBONXS, which reproduces accurately the merging of the (100) and (101) peaks and the shape of the (112) peak. The better quality of the fit is illustrated by the residuals given in Fig. 4.4(d), which have decreased significantly in the range of 30-120°. The resulting goodness of the fit decreases from $\chi^2 = 67$ for GSAS to $\chi^2 = 27$ for CARBONXS. The fits of other samples by both GSAS and CARBONXS are provided in the supplementary material. Table 4.2 gives the refined parameters in CARBONXS for each sample, from which mean values and the corresponding standard deviations for the different samples of each type of graphite can be obtained.

Zheng and Dahn [28] as well as Babu and Seehra [22] analysed XRD patterns of several graphitic samples using CARBONXS. In addition, DiJulio and Hawari [23] refined

Table 4.2: CARBONXS refined parameters of the graphite samples.

	$\langle a \rangle$ (Å)	$\langle d_{002} \rangle$ (Å)	L_a (Å)	M	L_c (Å)	σ (Å)	P_{RS}	P_{3R}
PGA1_#1	2.45918(1)	3.35805(6)	245(1)	105.4(6)	353.9(6)	0.0511(1)	0.154(1)	0.0701(7)
PGA1_#2	2.45983(1)	3.36054(6)	248(1)	112.2(6)	377.0(7)	0.0504(1)	0.153(1)	0.0679(7)
PGA2_#1	2.45946(6)	3.35735(1)	240(1)	124.0(1)	416.2(3)	0.0434(1)	0.170(1)	0.0620(8)
PGA2_#2	2.45976(6)	3.36006(1)	243(1)	120.8(1)	405.7(3)	0.0434(1)	0.171(1)	0.0613(8)
PCEA1_#1	2.45874(6)	3.36181(1)	233(1)	94.4(1)	317.3(3)	0.0524(1)	0.202(1)	0.0746(8)
PCEA1_#2	2.45845(6)	3.36128(6)	234(1)	94.2(1)	316.6(3)	0.0523(1)	0.199(1)	0.0760(8)
PCEA2_#1	2.45910(6)	3.36255(1)	231(1)	95.3(1)	320.4(3)	0.0512(1)	0.212(1)	0.0707(8)
PCEA2_#2	2.45879(6)	3.36133(1)	228(1)	95.4(1)	320.8(3)	0.0519(1)	0.209(1)	0.0719(8)
RID_#1	2.46033(6)	3.36326(1)	245(1)	107.6(6)	361.9(4)	0.0479(1)	0.161(1)	0.0682(8)
RID_#2	2.45998(6)	3.36114(1)	246(1)	107.8(6)	362.4(4)	0.0478(1)	0.162(1)	0.0676(8)
IG110_#1	2.45886(6)	3.36339(6)	223(1)	82.7(1)	278.1(2)	0.0551(1)	0.204(1)	0.0706(8)
IG110_#2	2.45880(6)	3.36236(6)	220(1)	83.2(1)	279.7(2)	0.0541(1)	0.206(1)	0.0703(8)
1940 PT_#1	2.46017(6)	3.37472(6)	209(1)	75.1(1)	253.4(3)	0.0644(1)	0.265(1)	0.0668(9)
1940 PT_#2	2.45959(6)	3.37250(6)	209(1)	74.5(1)	251.4(2)	0.0639(1)	0.265(1)	0.0668(9)

neutron diffraction data of a nuclear graphite with the same model. In the following, we will present our findings and compare them with the results of these previous studies.

Fig. 4.5 displays the average values of interlayer spacing $\langle d_{002} \rangle$ and the in-plane lattice parameter $\langle a \rangle$. For all samples $\langle a \rangle$ varies within 0.2% around the value of single crystalline graphite 2.461 Å. As expected, this parameter cannot fluctuate too much due to the strong covalent in-plane bonding and we attribute the weak scattering of the data to systematic errors. The situation is different for the interlayer spacing $\langle d_{002} \rangle$, which varies over a much larger range from 3.357 Åto 3.403 Å. We point out that this large scatter is mainly due to the data of [22], where values of $\langle d_{002} \rangle$ much higher than $d_{002}^{\text{crystal}} = 3.354$ Å, the interlayer spacing between two perfectly oriented layers, have been found. This is also the case for our non-nuclear graphite 1940 PT sample. In contrast, the scatter for the nuclear graphites is weak and for all samples $\langle d_{002} \rangle$ is close to 3.360 Å, i.e. slightly larger than d_{002}^{crystal}. This behavior indicates that nuclear graphites have a more perfect and compact structure, resulting from the fact that they are all produced out of easily graphitized raw material. This high graphitization degree makes these graphites suitable for high efficiency neutron moderation.

Additional important parameters are the coherent lengths L_a and L_c, which both increase when the interlayer spacing $\langle d_{002} \rangle$ decreases as shown in Fig. 4.6. This is an important but not unexpected result since low values of $\langle d_{002} \rangle$ imply higher degree of order and thus more perfect graphite structures and longer coherent lengths both in the plane and between planes. The fact that L_c varies over a slightly larger range than L_a may be attributed to the inherent anisotropy of the structure.

Fig. 4.7 displays $\langle d_{002} \rangle$ as a function of the standard deviation of interlayer spacing fluctuations σ. There is a strong scatter of the data in agreement with [16] and we do not clearly see the linear relationship found in [22]. The dashed line corresponds to the deviation of $\langle d_{002} \rangle$ from the possible minimum value d_{002}^{crystal}: $\xi = \langle d_{002} \rangle - d_{002}^{\text{crystal}}$, which implicitly assumes that fluctuations cannot lead to interlayer spacing smaller than d_{002}^{crystal}. From the figure it is clear that for all samples, including nuclear graphite, $\sigma \gg \xi$. This is consistent with [16], where it was argued that the disorder in the graphite structure is
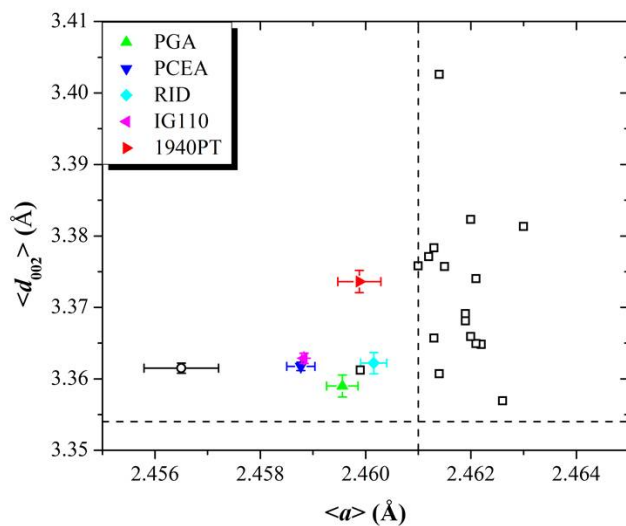
Figure 4.5: Average interlayer spacing $\langle d_{002} \rangle$ and the average in-plane lattice constant $\langle a \rangle$. The open squares are from [22] and the open star from [23]. The dashed lines represent the respective values for the perfect single crystalline graphite structure.
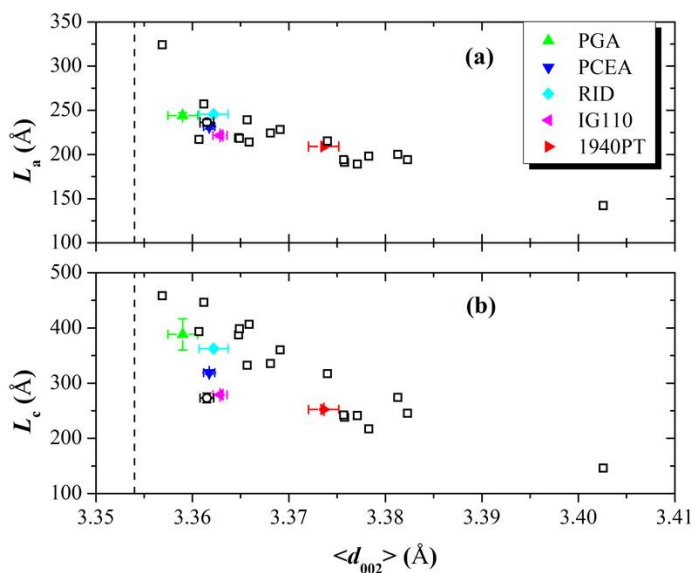
Figure 4.6: Coherent lengths (a) in plane L_a and (b) inter-plane length L_c plotted versus the average interlayer spacing $\langle d_{002} \rangle$. The open squares are from [22] and the open star from [23]. Both L_a and L_c increase as $\langle d_{002} \rangle$ decreases and approaches the value of the perfect crystalline structure represented by the dashed line. L_c grows faster than L_a, which may be attributed to the inherent anisotropy of the graphite structure.
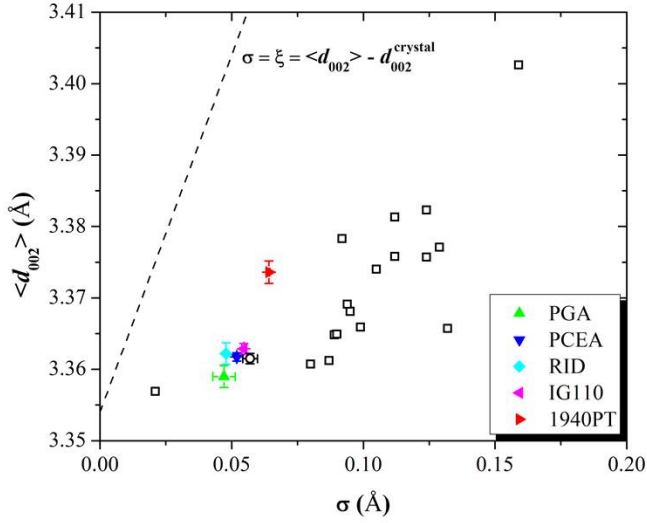
Figure 4.7: Average interlayer spacing $\langle d_{002} \rangle$ plotted against the standard deviation σ of fluctuations in the interlayer spacing. The open squares are from [22] and the open star from [23]. The dashed line represents the limit value $\sigma = \xi = \langle d_{002} \rangle - d_{002}^{\text{crystal}}$. For all samples $\sigma \gg \xi$.

not simply due to the stacking faults, in which case the standard deviation of interlayer spacing fluctuations σ should be equal to ξ. Disorder can also occur due to other causes, such as dislocations, crosslinks, vacancies and interstitial defects. The differences in the types and quantities of disorder for various samples might result in the scatter of the data points [16].

Fig. 4.8 displays the dependence of $\langle d_{002} \rangle$ on the parameter P_3R, which quantifies the probability of 3R stacking sequence. As already mentioned most graphite samples contain a non-negligible fraction of rhombohedral phase and for all samples investigated in this work: $P_{3R} \sim 0.07$. The compilation with the other data from the literature does not show a significant correlation between $\langle d_{002} \rangle$ and P_{3R}. To validate this result, X-ray diffraction patterns were calculated with the computer program DIFFaX, which can simulate diffraction patterns of structures with stacking faults [29]. The resulting patterns are given in Fig. 4.9 and show indeed that both (002) and (004) peaks are independent of P_{3R}, which increases from 0% to 100%.

Several empirical approaches [12, 13] correlate the interlayer spacing $\langle d_{002} \rangle$ with the proportion of random disoriented layers P_{RS}. The approach adopted by R. Franklin [13] assumed that the average interlayer spacing varies between two extreme values: 3.354 Å, the spacing of ideally oriented layers (ideal ABAB stacking) and 3.440 Å, the spacing between two disoriented layers. Moreover, in case a group of oriented layers is adjacent to a disoriented layer, the spacing between the two is smaller than the spacing in a fully disoriented structure (3.440 Å). The average interlayer spacing was then described as a
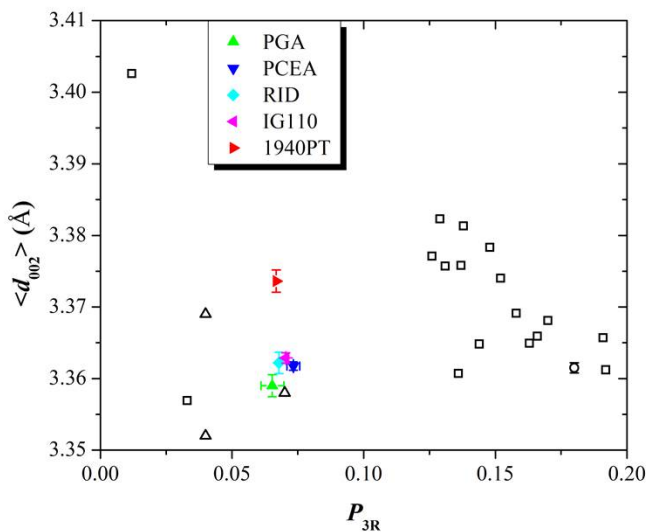
Figure 4.8: Average interlayer spacing $\langle d_{002} \rangle$ plotted versus the probability of 3R stacking faults P_{3R}. The open squares are from [22], the open star from [23] and the open triangles from [28].
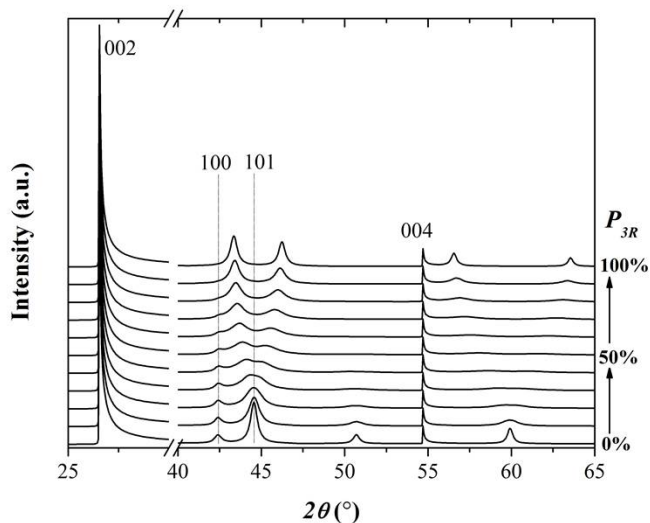
Figure 4.9: Simulated X-ray diffraction patterns for a graphite structure containing 3R stacking faults, with a probability P_{3R}, which increases from 0% to 100%. All patterns show the same (002) and (004) peaks, which are thus independent of P_{3R}.
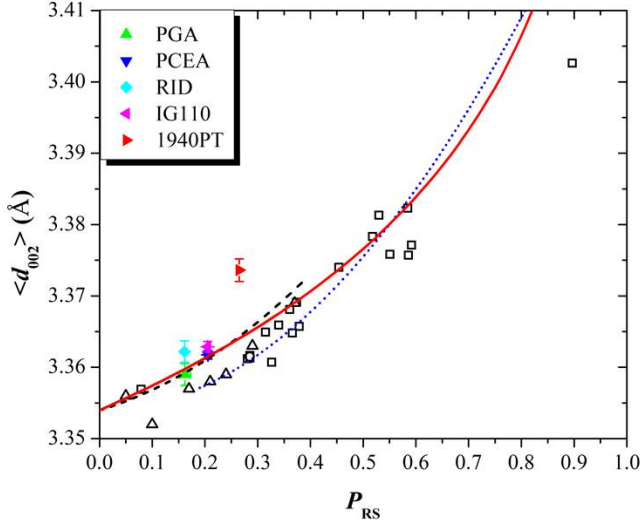
Figure 4.10: Average interlayer spacing $\langle d_{002} \rangle$ plotted versus the probability of random shifts P_{RS}. The open squares are from [22], the open star from [23] and the open triangles from [28]. The dotted line corresponds to Eq. 4.3; the dashed line to Eq. 4.4 (the parameter p in Eq. 4.3 and 4.4 is substituted by P_{RS}); and the solid line to Eq. 4.6 respectively.

function of the probability, p, that a disorientation occurs between any two given neighboring layers:

$$\langle d_{002} \rangle [\text{Å}] = 3.440 - 0.086(1 - p^2) \equiv d_{002}^{\text{crystal}} + 0.086 p^2 \tag{4.3}$$

This empirical relation is satisfied for large p ($p \geq 0.2$) as pointed out in [11]. To give a better fit to the experimental data, it was proposed in [12] that for small p ($p \leq 0.2$) the reduction of the spacing between the disoriented layer and the nearest oriented group may be weaker, resulting a similar relationship:

$$\langle d_{002} \rangle [\text{Å}] = 3.440 - 0.086(1 - p) - 0.064p(1 - p) \equiv d_{002}^{\text{crystal}} + 0.022 p + 0.064 p^2 \tag{4.4}$$

Since 3R stacking faults do not affect the average interlayer spacing $\langle d_{002} \rangle$, which has been discussed above, the disorder parameter p in Eq. 4.3 and 4.4 is substituted by P_{RS} from the model used in this work. As shown in Fig. 4.10, the compiled experimental results agree well with both formulas, which are represented by the dotted and dashed lines respectively.

A more general model for the disorder structure of graphite was developed in [16], where by averaging over all pairs of layers the relative position of adjacent layers follow a three-dimensional Gaussian distribution with mean square deviations δ_a^2 parallel and δ^2 perpendicular to the basal plane. The experimental data show a strong correlation between $\langle d_{002} \rangle$ and the square of in-plane fluctuation parameter δ_a^2 has been reported
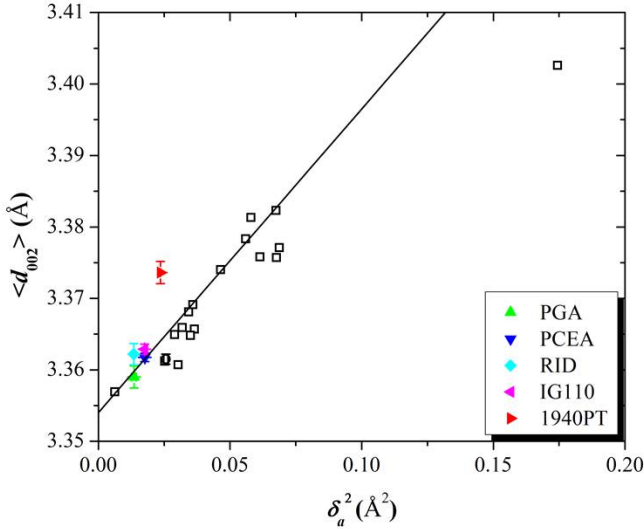
Figure 4.11: Average interlayer spacing $\langle d_{002} \rangle$ plotted against the fluctuations of the intra-layer spacing δ_a^2. The open squares are from [22] and the open star from [23]. The solid line corresponds to Eq. 4.5.

in [16]:

$$\langle d_{002} \rangle = d_{002}^{\text{crystal}} + 0.425 \delta_a^2 \tag{4.5}$$

To confirm this relation, $\langle d_{002} \rangle$ is plotted against δ_a^2 in Fig. 4.11, whose values were calculated through Eq. 4.2, and the line corresponds to Eq. 4.5. It is clear that the data are in agreement with this formula. There is no obvious explanation for this systematic behavior which seems to be a genuine feature of graphite as suggested by [16]. The combination of equations (2) and (5) under the condition that $\langle a \rangle = 2.461$ Å, justified by the fact that all graphite samples have the same in-plane lattice constant as mentioned above, leads to:

$$\langle d_{002} \rangle = d_{002}^{\text{crystal}} - 0.0326 \ln(1 - P_{RS}) \tag{4.6}$$

This equation is represented by the solid line in Fig. 4.10 and describes well the observed behavior. However, the extrapolation the limit $P_{RS} \rightarrow 1$ leads to the non-physical result $\langle d_{002} \rangle \rightarrow \infty$. This is indeed a non-realistic situation because graphite is typically produced at high temperatures and thus it is impossible to obtain a sample with such a high concentration of random shift stacking faults.

4.5. DISCUSSION-CONCLUSION

Our results show that Shi's model and program CARBONXS can well interpret the X-ray diffraction patterns of graphite samples and is superior to the conventional Rietveld method and the GSAS refinement program. This is because CARBONXS properly takes into account the effects of stacking disorder, fluctuations of interlayer spacing and the

penetration depth of X-rays on the intensities and broadenings of diffraction peaks. The resulting refinement not only provides the basic lattice parameters but also quantifies the disorder properties of the structure.

The interdependency of refined parameters discussed in the previous section shows that $\langle d_{002} \rangle$ is the key indicator for the perfection/graphitization degree of the structure. The higher the degree of perfection, the smaller is the average interlayer spacing $\langle d_{002} \rangle$. The smaller the $\langle d_{002} \rangle$ the larger are the coherent regions L_a and L_c, and the smaller is the fraction of stacking faults and random shifts. The generic behavior illustrated by Fig. 4.10 and 4.11 makes it thus possible to predict the degree of random stacking faults disorder from the value of $\langle d_{002} \rangle$. The average interlayer spacing $\langle d_{002} \rangle$ of all nuclear graphite samples was found to be close to 3.360 Å, which is slightly higher than the lowest possible value of 3.354 Å. Our results show that the structure of nuclear graphite is far from being perfectly ordered, with around 7% of 3R stacking faults and 15-25% random shifts. However, $\langle d_{002} \rangle$ is correlated only with the random shifts and not with the 3R stacking faults.

Of particular interest for applications is the fact that the model quantifies two different coherent lengths, one in-plane and one inter-plane, which can be directly related to the mechanical properties, irradiation damage and dimensionality of graphite [30]. The small values of L_a and L_c obtained in this work imply that despite its high degree of graphitization nuclear graphite is still highly disordered.

The significant consistency between our refined parameters and previous work indicates that the parameters obtained by this method are universal. Thus the microscopic structural properties revealed by XRD of nuclear graphites studied in our work and graphites from the references follow a generic behavior, despite the fact that they are made from different precursors and manufactured by different processing methods resulting in different physical properties.

Future work will focus on a similar analysis of XRD patterns from neutron-irradiated samples. By comparing the results obtained on virgin and irradiated samples we should be able to investigate the effects of irradiation damage at the microscopic level.

Last but not least, the refinement program CARBONXS will be further improved to include the sample displacement error for taking into account errors related to the precise sample position in the X-ray diffractometer. In this way it will be possible to account for an offset due to imprecise diffraction geometry. To obtain more accurate structural parameters, the effect of instrument resolution will also be included.

4.6. ACKNOWLEDGEMENTS
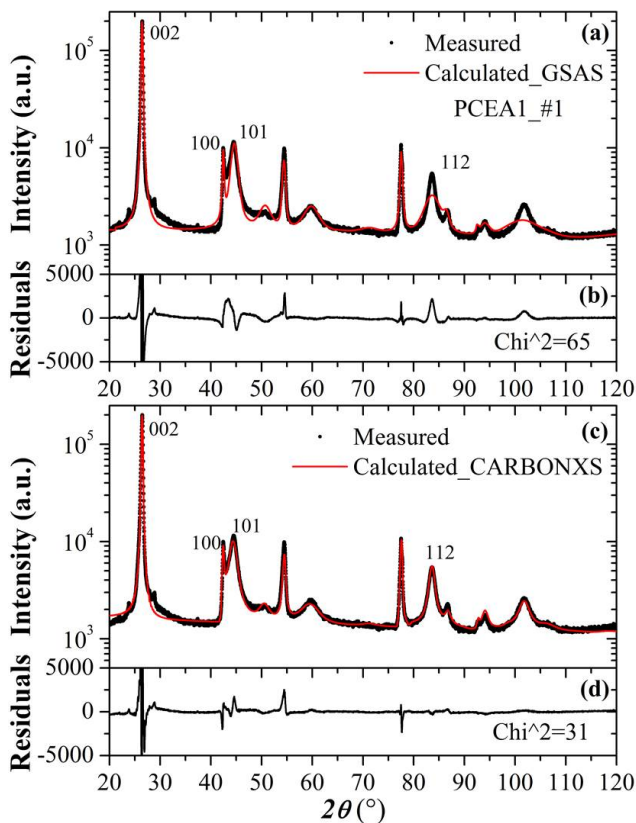
Figure 4.12: Measured and calculated X-ray diffraction patterns of PCEA1_#1. The data were fitted using (a) Rietveld refinement method and the program GSAS and (c) Shi's model and the program CARBONXS. The residuals between measured and calculated intensities are given in (b) and (d) for GSAS and CARBONXS respectively.

4.7. SUPPLEMENT

Fig. 4.12-4.15 show the fits of other 4 representative samples (PCEA1_#1, RID_#1, IG110_#1 and 1940 PT_#1). Both by visual inspection and comparison of χ^2, it is clear that CARBONXS gives better fitting results as compared to GSAS.
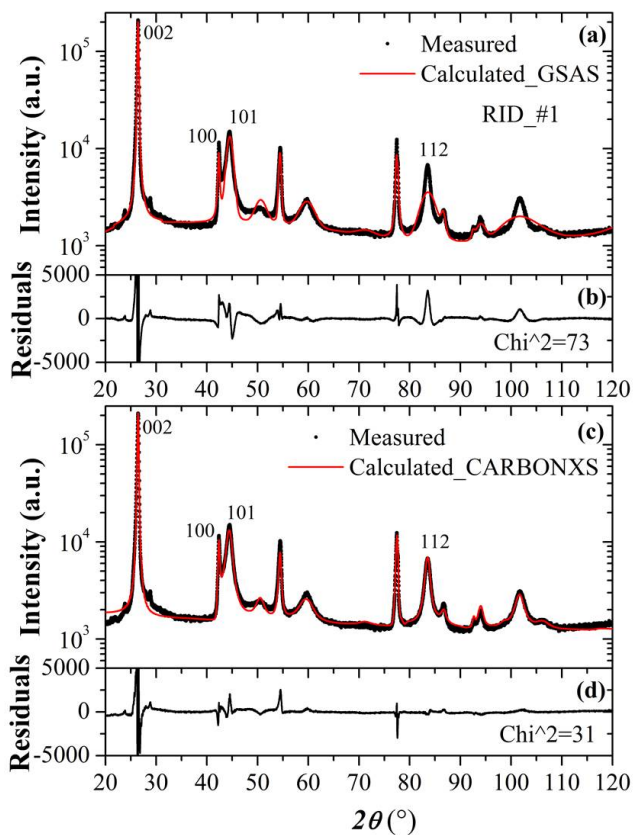
Figure 4.13: Measured and calculated X-ray diffraction patterns of RID_#1. The data were fitted using (a) Rietveld refinement method and the program GSAS and (c) Shi's model and the program CARBONXS. The residuals between measured and calculated intensities are given in (b) and (d) for GSAS and CARBONXS respectively.
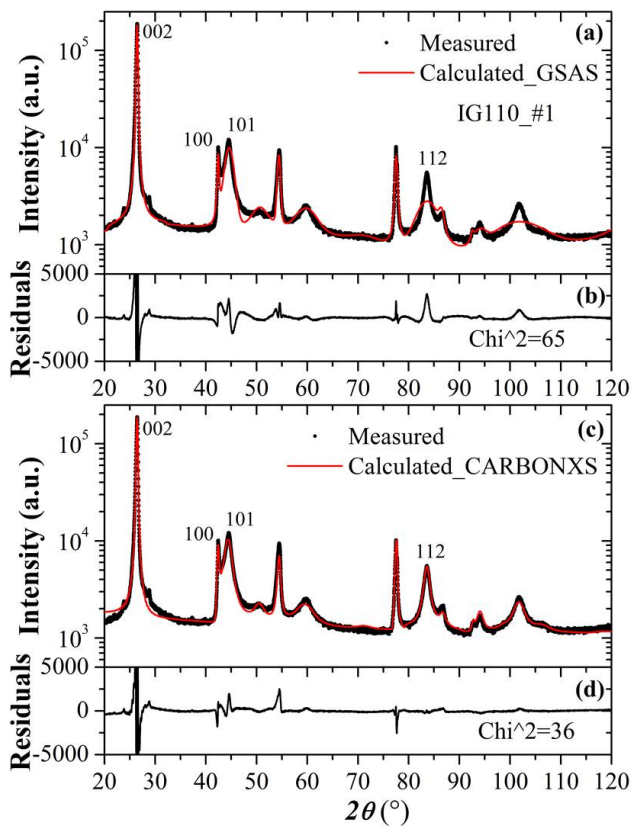
Figure 4.14: Measured and calculated X-ray diffraction patterns of IG110_#1. The data were fitted using (a) Rietveld refinement method and the program GSAS and (c) Shi's model and the program CARBONXS. The residuals between measured and calculated intensities are given in (b) and (d) for GSAS and CARBONXS respectively.
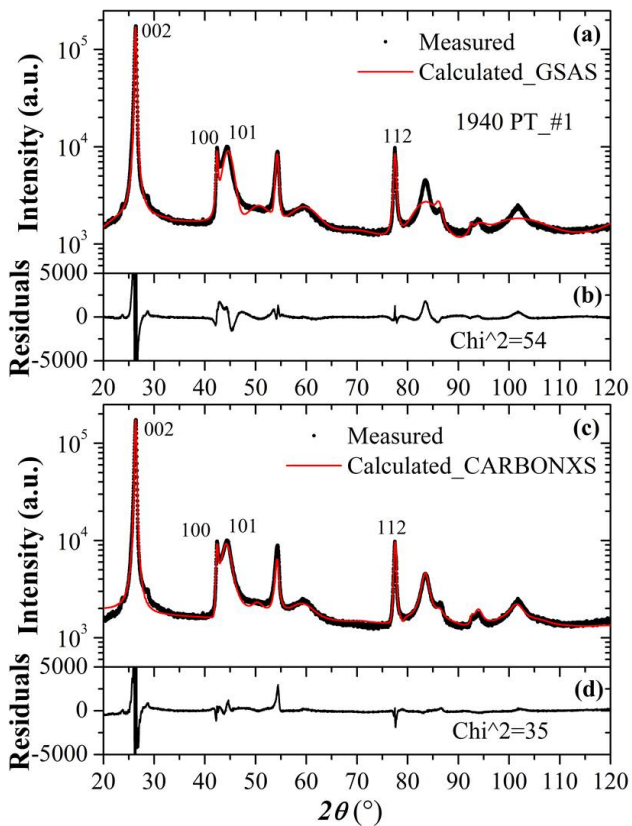
Figure 4.15: Measured and calculated X-ray diffraction patterns of 1940 PT_#1. The data were fitted using (a) Rietveld refinement method and the program GSAS and (c) Shi's model and the program CARBONXS. The residuals between measured and calculated intensities are given in (b) and (d) for GSAS and CARBONXS respectively.
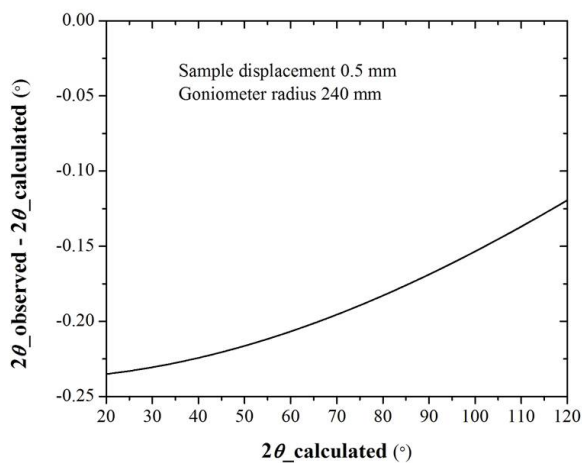
Figure 4.16: The peak positions are affected by the sample displacement error in XRD measurement: $\Delta 2\theta = -\frac{2s}{R}\cos\theta$ (s is the sample displacement; R is the radius of the goniometer). Since carbon has a low absorption coefficient for X-rays, it can penetrate deeply into the graphite sample and the scattering from particles below the sample surface are not strongly attenuated. Thus the high penetration depth of X-rays affects the peak positions, shapes and also causes broadenings.
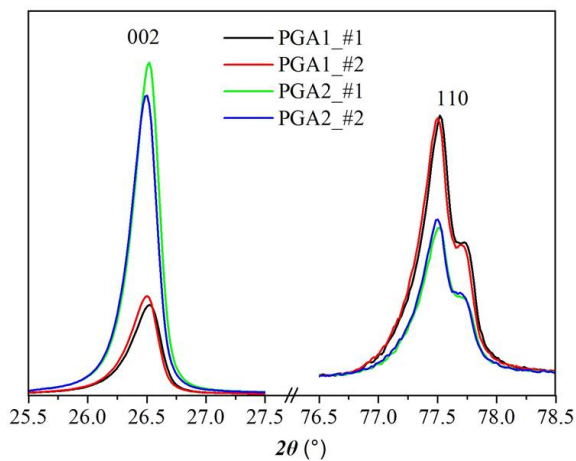
Figure 4.17: Measured X-ray diffraction patterns of PGA samples. PGA is of high an-isotropic, because of which, the intensities of (110) peaks are enhanced in PGA1 samples, and the intensities of (002) peaks of PGA2 samples are likewise much higher than PGA1. The relatively large discrepancies between refinement parameters of PGA1 and PGA2 may be due to the significant differences in diffraction patterns.

REFERENCES

[1] Z. Zhou, W. Bouwman, H. Schut, and C. Pappas, *Interpretation of x-ray diffraction patterns of (nuclear) graphite,* Carbon **69**, 17 (2014).

[2] B. Marsden and A. J. Wickham, *Characterization, treatment and conditioning of radioactive graphite from decommissioning of nuclear reactors,* TECDOC (2006).

[3] R. Telling and M. Heggie, *Radiation defects in graphite,* Philosophical Magazine **87**, 4797 (2007).

[4] J. H. W. Simmons, *Radiation Damage in Graphite: International Series of Monographs in Nuclear Energy,* Vol. 102 (Elsevier, 1965).

[5] B. Kelly, B. Marsden, K. Hall, D. Martin, A. Harper, and A. Blanchard, *Irradiation damage in graphite due to fast neutrons in fission and fusion systems,* IAEA Tecdoc **1154** (2000).

[6] G. Bacon, *A note on the rhombohedral modification of graphite,* Acta Crystallographica **3**, 320 (1950).

[7] E. Freise and A. Kelly, *The deformation of graphite crystals and the production of the rhombohedral form,* Philosophical Magazine **8**, 1519 (1963).

[8] J. Biscoe and B. Warren, *An x-ray study of carbon black,* Journal of Applied Physics **13**, 364 (1942).

[9] G. Bacon, *Unit-cell dimensions of graphite,* Acta Crystallographica **3**, 137 (1950).

[10] G. Bacon and B. Warren, *X-ray diffraction studies of neutron-irradiated graphite,* Acta Crystallographica **9**, 1029 (1956).

[11] G. Bacon, *The a dimension of graphite,* Acta Crystallographica **4**, 561 (1951).

[12] G. Bacon, *The interlayer spacing of graphite,* Acta Crystallographica **4**, 558 (1951).

[13] R. E. Franklin, *The structure of graphitic carbons,* Acta Crystallographica **4**, 253 (1951).

[14] R. E. Franklin, *Crystallite growth in graphitizing and non-graphitizing carbons,* in *Proceedings of the Royal Society of London A: Mathematical, Physical and Engineering Sciences*, Vol. 209 (The Royal Society, 1951) pp. 196–218.

[15] G. Bacon, *The reduction of the crystalline perfection of graphite by grinding,* Acta Crystallographica **5**, 392 (1952).

[16] W. Ruland, *X-ray studies on the structure of graphitic carbons,* Acta Crystallographica **18**, 992 (1965).

[17] N. Iwashita and M. Inagaki, *Relations between structural parameters obtained by x-ray powder diffraction of various carbon materials,* Carbon **31**, 1107 (1993).

[18] N. Iwashita, C. R. Park, H. Fujimoto, M. Shiraishi, and M. Inagaki, *Specification for a standard procedure of x-ray diffraction measurements on carbon materials,* Carbon **42**, 701 (2004).

[19] S.-H. Chi and G.-C. Kim, *Comparison of the oxidation rate and degree of graphitization of selected ig and nbg nuclear graphite grades,* Journal of nuclear materials **381**, 9 (2008).

[20] S.-H. Chi and G.-C. Kim, *Comparison of 3mev c+ ion-irradiation effects between the nuclear graphites made of pitch and petroleum cokes,* Journal of nuclear materials **381**, 98 (2008).

[21] H. Rietveld, *A profile refinement method for nuclear and magnetic structures,* Journal of applied Crystallography **2**, 65 (1969).

[22] V. S. Babu and M. Seehra, *Modeling of disorder and x-ray diffraction in coal-based graphitic carbons,* Carbon **34**, 1259 (1996).

[23] D. DiJulio and A. Hawari, *Examination of reactor grade graphite using neutron powder diffraction,* Journal of Nuclear Materials **392**, 225 (2009).

[24] T. Lokajicek, P. Lukas, A. N. Nikitin, I. V. Papushkin, V. V. Sumin, and R. N. Vasin, *The determination of the elastic properties of an anisotropic polycrystalline graphite using neutron diffraction and ultrasonic measurements,* Carbon **49**, 1374 (2011).

[25] H. Shi, *Disordered carbons and battery applications,* Ph.D. thesis, Simon Fraser University (1993).

[26] H. Shi, J. Reimers, and J. Dahn, *Structure-refinement program for disordered carbons,* Journal of applied crystallography **26**, 827 (1993).

[27] G. Haag, *Properties of ATR-2E graphite and property changes due to fast neutron irradiation,* Ph.D. thesis, Forschungszentrum Jülich GmbH, Zentralbibliothek (2005).

[28] T. Zheng and J. Dahn, *The effect of turbostratic disorder on the staging transitions in lithium intercalated graphite,* Synthetic metals **73**, 1 (1995).

[29] M. Treacy, J. Newsam, and M. Deem, *A general recursion method for calculating diffracted intensities from crystals containing planar faults,* in *Proceedings of the Royal Society of London A: Mathematical, Physical and Engineering Sciences,* Vol. 433 (The Royal Society, 1991) pp. 499–520.

[30] Y. I. Shtrombakh, B. Gurovich, P. Platonov, and V. Alekseev, *Radiation damage of graphite and carbon-graphite materials,* Journal of nuclear materials **225**, 273 (1995).

5

INFLUENCE OF NEUTRON IRRADIATION ON THE MICROSTRUCTURE OF NUCLEAR GRAPHITE: AN X-RAY DIFFRACTION STUDY

The neutron irradiation effects on the microstructure of (nuclear) graphite have been investigated by X-ray diffraction on virgin and low doses (~ 1.3 and ~ 2.2 dpa), high temperature (750° C) irradiated samples. The diffraction patterns were interpreted using a model, which takes into account the relative amount of stacking faults and turbostratic disorder. Besides the lattice constants, the model introduces coherent lengths in the c-axis and the basal plane, that characterise the volumes from which X-rays are scattered coherently. The deduced model parameters show that in the basal plane the lattice constant remains unchanged while the coherent length decreases. Along the c-axis the lattice constant increases but the coherent length first increases and then decreases. In addition, the higher dose increases the degree of turbostratic disorder. Our results are in agreement with previous observations from electron microscopy, and the methodology used in this work allows to quantify the effect of irradiation damage on the microstructure of nuclear graphite seen by X-ray diffraction.

5.1. INTRODUCTION

For more than 70 years, from the first man-made nuclear reactor Chicago Pile 1 to the very recent high temperature gas-cooled reactors, graphite has been used as a neutron moderator. During reactor operations the high energy neutrons induce changes in the structural, dimensional and physical properties of graphite, e.g. stacking faults, density and thermal conductivity, which adversely affect the behaviour of the moderator and ultimately the safe operation of the reactor. Thus it is important to have a better understanding of the effects of the irradiation damage and to establish a link between the structure and behaviour of the graphite.

Radiation damage in the graphite structure arises when fast fission neutrons displace carbon atoms from their lattice positions, thereby creating interstitials and vacancies, which may ultimately form large defects, such as interstitial and vacancy loops. These extended defects lead to dimensional changes in graphite crystals commonly observed as expansion in c-axis perpendicular to the basal plane due to the accumulation of interstitials, and shrinkage in the basal plane due to the presence of vacancies [2–6]. To investigate the structural changes transmission electron microscopy (TEM) and X-ray diffraction (XRD) have been extensively used. TEM studies of irradiated graphite revealed the formation of interstitial dislocation loops and the breaking, bending and displacement of basal planes [7–9]. With XRD, the standard tool for studying the crystallographic structure of materials, it has been found that the neutron irradiated graphite leads to changes in lattice parameters [4, 10–14], which depend on the irradiation conditions such as flux, fluence and temperature. In general, up to a critical dose, the in-plane lattice constant a decreases while the interlayer spacing d_{002} increases. For irradiations at higher temperatures, these effects are less pronounced.

As we have discussed in [15], a proper analysis of XRD patterns from graphite requires a model that incorporates not only the anisotropy of the structure but also disorder. Such a model has been proposed by Shi [16, 17] and will be introduced below. Besides the basic lattice constants, a and d_{002}, the model includes variables that parametrise the effect of disorder: coherent lengths, stacking faults probabilities and lattice distance fluctuations. This approach leads to a comprehensive description of the structure and will be used in the following to analyse the XRD patterns from low-dose, high-temperature neutron irradiated graphites and investigate the effect of irradiation damage on the structure.

5.2. SHI'S DISORDERED GRAPHITE MODELS AND THE PROGRAM CARBONXS

A perfect graphite crystal consists of layers of carbon atoms, arranged in the 2D hexagonal graphene network. Stacking of these layers in the ...ABAB... sequence leads to the hexagonal 2H structure, illustrated in Fig. 5.1(a) and (b). In case (some of) the basal planes slip out of the perfect alignment so-called stacking faults are introduced. These may lead to ABC arrangements or to more complex turbostratic disorder caused by random shifts or rotations between adjacent layers. The stacking faults introduce local strains, resulting in a distribution of interlayer spacings. In the XRD pattern, this leads to a broadening and a shift of the diffraction peaks. In Shi's approach, the disorder is taken

into account in two models: a two-layer model for graphitic carbons and a single-layer model for disordered carbons [16, 17].

Both models have been integrated in the refinement program CARBONXS. In addition to the structural parameters of the models, it also includes corrections for the X-ray polarization, the Lorentz factor, preferred sample orientation and an isotropic temperature (Debye-Waller) factor. The effect of the high penetration depth of X-rays is incorporated as well by taking into account the absorption of X-rays and the sample size. The program optimizes all parameters by performing a least-squares fit between the measured and calculated XRD patterns. A comparison between the standard Rietveld refinement method and the two-layer model can be found in our previous work [15].

THE TWO-LAYER MODEL

The two-layer model has been successful in describing diffraction patterns of graphitic carbons and graphites [15–19]. It takes two adjacent layers in AB stacking as a building block of the structure. These blocks are then stacked (1) orderly leading to ABAB stacking, (2) with a specific shift resulting in ABC stacking with a probability P_{3R}, or (3) with a random shift to turbostratic disorder with a probability P_{RS}, see Fig. 5.1(c). Obviously, for $P_{RS} = P_{3R} = 0$, this model reproduces the 2H stacking sequence.

As mentioned above, the stacking faults introduce strains resulting in a distribution of local interlayer spacings d_{002} that is modelled by a Gaussian function given by:

$$p(d_{002}) = \frac{1}{\sqrt{2\pi}\sigma} \exp(\frac{-(d_{002} - \langle d_{002}\rangle)^2}{2\sigma^2}) \tag{5.1}$$

where $\langle d_{002}\rangle$ is the experimentally obtained average interlayer spacing and σ the standard deviation of the fluctuations. This model assumes that there are no fluctuations in interlayer spacing within an AB building block, as illustrated in Fig. 5.1(c).

Besides the average lattice parameters $\langle d_{002}\rangle$ and $\langle a \rangle$, the model introduces two additional characteristic lengths L_a (in the basal plane) and L_c (along c-axis), which define a volume from which X-rays may diffract coherently. Fig. 5.1(d) shows a single grain containing several independently oriented coherent scattering volumes, each of which consists of dozens of AB building blocks.

THE SINGLE-LAYER MODEL

The single-layer model has been introduced to describe the structure of highly disordered carbons, such as cokes and heat-treated pitch [16–18]. In this model, each layer is an entity independent from the surrounding ones. Starting with a specific layer at the A position, the next layer may thus occupy either a random position with a probability P_{RS}, or a B or C position, each with equal probability $(1 - P_{RS})/2$, as illustrated in Fig. 5.1(e). Similar to the case of the two-layer model, L_a and L_c are used to discriminate between regions that scatter coherently and the highly disordered unorganized non-diffracting regions. In this model, the probability of finding a given interlayer spacing d_{002} becomes:

$$p(d_{002}) = g\delta_D(d_{002} - \langle d_{002}\rangle) + (1 - g)\frac{1}{\sqrt{2\pi}\sigma} \exp(\frac{-(d_{002} - \langle d_{002}\rangle)^2}{2\sigma^2}) \tag{5.2}$$
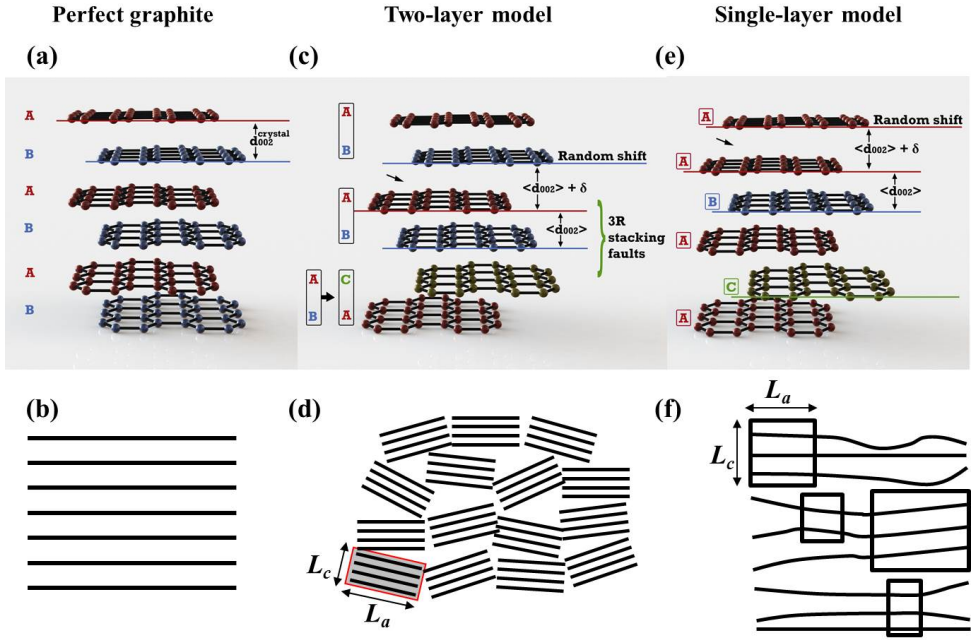
Figure 5.1: Schematic of stacking sequences of carbon layers and corresponding overview of the coherent regions in (a-b) a perfect graphite crystal, (c-d) the two-layer model and (e-f) the single-layer model, respectively.

where g corresponds to the fraction of well ordered pair of layers, similarly to the two-layer model which thus becomes a special realisation of the case g=0.5. The limits $g = 1$ and $g = 0$ correspond to perfectly ordered and disordered structures respectively. The parameter g quantifies the probability of highly ordered, low-strain regions with an interlayer spacing $\langle d_{002} \rangle$. The highly disordered, organized and thus high strain regions have the probability $(1 - g)$ and for $g = 0$ the interlayer spacing fluctuations are homogeneously spread over the entire specimen. It has been suggested that the latter case corresponds to carbons treated at high temperatures [16].

5.3. EXPERIMENTAL

As part of the Seventh Framework Programme of the European Union, the Nuclear Research and Consultancy Group (NRG) has conducted a large graphite irradiation program (called INNOGRAPH) for the development of High Temperature Reactor (HTR) technology. The program comprises five irradiation experiments executed in the High Flux Reactor (HFR) in Petten on present day available graphite grades at irradiation temperatures between 650°C and 950°C up to a received neutron dose of 23 dpa, as shown in Fig 5.2. The post-irradiation examination of the experiments yields graphite design curves reflecting the dimensional changes and changes in the dynamic Young's modulus and the coefficients of thermal expansion and thermal conductivity. The irradiation behaviour of HTR candidate graphite grades are compared with respect to the manu-
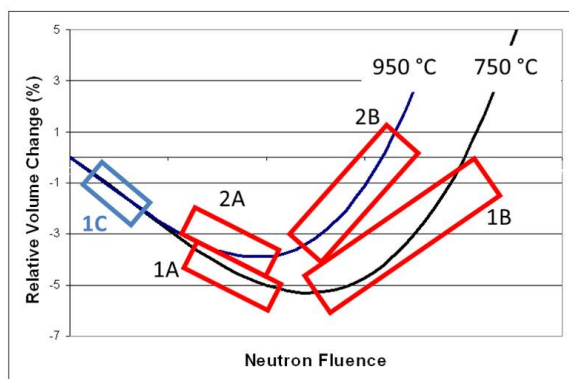
Figure 5.2: Schematic overview of the INNOGRAPH irradiation experiments [21]. 1A: 750°C low/medium dose, 1B: 750°C high dose, 2A: 950°C low/medium dose, 2B: 950°C high dose, 1C: 750°C low dose.

facturing processes and the raw coke material. The preliminary results of INNOGRAPH have been reported [20, 21] showing that the properties are more rapidly affected by neutron irradiation at the low dose of 1-2 dpa, which thus arouses interests in investigating the micro-structural changes of irradiated graphite samples from INNOGRAPH-1C.

For the current investigation XRD results on virgin and low dose (1.3 and 2.2 dpa, at 750°C) specimens are examined. The five grades of nuclear graphite considered in this work are kept anonymous and represented as A-E because the results are not public yet. The density for samples A, D and E is 1.8 g/cm^3, and for B and C is 1.9 g/cm^3. All specimens are cylindrical with a diameter of 8 mm and a length of 6 mm.

The XRD measurements were performed using a Bruker D8 Advance powder diffractometer in $\theta - 2\theta$ configuration over an angular range between $20 - 90°$ with a step size of 0.05°. A dedicated specimen holder is used to place the surface of the specimens in focal plane of the X-ray beam.

All measured XRD patterns were refined using the refinement program CARBONXS applying the two-layer model, the single-layer model with floating g, and the single-layer model with fixed $g = 0$. The results of refined parameters are averaged values obtained over several specimens of the same grade and irradiation dose, and thus the systematic and experimental errors are indicated by the corresponding standard deviations. We note that the source code of CARBONXS was provided by Prof. J.R. Dahn of Dalhousie University and it is available from the authors of [16].

5.4. Results and discussion

5.4.1. Analysis of the XRD patterns

Fig. 5.3 displays measured and calculated X-ray diffraction patterns for the non-irradiated sample 12A-0 dpa. The results show that all three refinement procedures yield fairly good fits. We note that due to the atomic scattering factor of carbon for X-rays, the intensities of diffraction peaks fall off seriously at high scattering angle 2θ, and the (002) peak dominates the diffraction pattern. Therefore, χ^2 is mainly determined by the strong
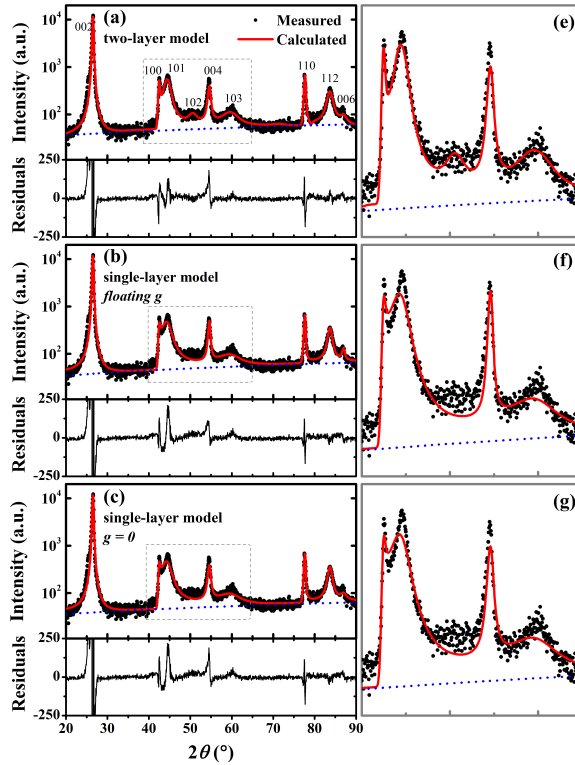
Figure 5.3: Measured and calculated XRD patterns and residuals for the non-irradiated sample 12A-0 dpa: (a) the two-layer model, (b) the single-layer model with floating g, and (c) the single-layer model with fixed $g = 0$. (e-g) show the details between $40 - 65°$. The dash lines represent the linear background used for the fits. Notice that the intensity axis is logarithmic.

(002) peak, and it is not a proper indicator of the goodness of the fit. To better examine the quality of the fits, the data and fitting profiles at 2θ between $40 - 65°$ are zoomed in Fig. 5.3(e-g). It is clear that the (100)/(101) region, and the (102) and (103) peaks are reproduced more accurately by the two-layer model. Similar behaviour has been observed for the irradiated sample 2A-2.2 dpa, as shown in Fig. 5.4.

The refined parameters for the specimens 12A-0 dpa and 2A-2.2 dpa are listed in Table 5.1. The two-layer model and the single-layer models yield to comparable values of the parameters with the exception of σ. In fact the case of the single-layer model with floating g for the irradiated sample, a large value of σ is obtained and L_c has a large uncertainty, illustrating the high inter-correlation between these three parameters.

From the above we conclude that the microstructure of graphite can be described by both models. However, on the basis of the overall agreement between the fits and measurements, the best description is provided by two-layer model. Therefore, in the following we will focus on the refined parameters obtained by the two-layer model (data are provided in the supplement). We note that the single-layer model might be more
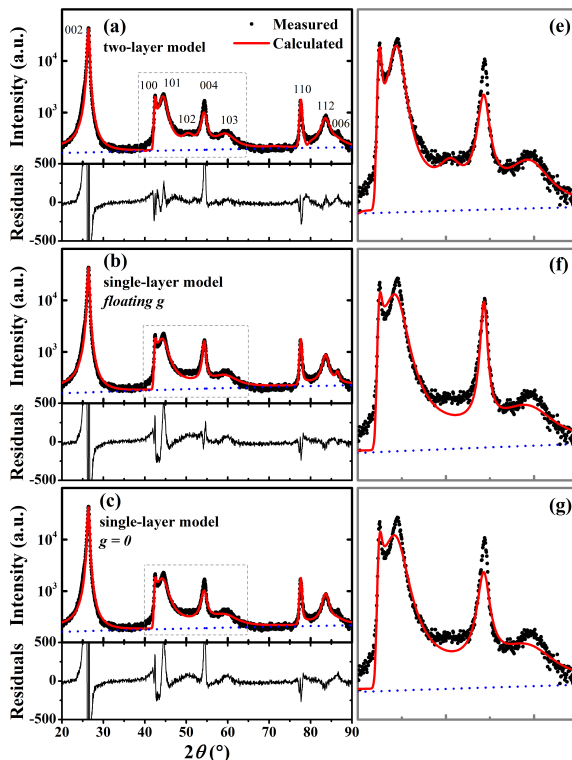
Figure 5.4: Measured and calculated XRD patterns and residuals for the irradiated sample 2A-2.2 dpa: (a) the two-layer model, (b) the single-layer model with floating g, and (c) the single-layer model with fixed $g = 0$. (e-g) show the details between $40 - 65°$. The dash lines represent the linear background used for the fits. Notice that the intensity axis is logarithmic.

promising for high dose irradiated graphite specimens, which have a highly disordered structure. This proposition has been demonstrated by the fits of XRD patterns from high dose irradiated graphite samples under oxidising conditions, as shown in the supplement.

5.4.2. IRRADIATION EFFECTS

Figures 5.5 and 5.6 summarise the changes of the refined parameters as a function of the irradiation dose. For all specimens the average in-plane lattice parameter $\langle a \rangle$ varies little with irradiation. On the other hand, at a dose of ~ 1.5 dpa the average interlayer spacing $\langle d_{002} \rangle$ has increased by ~ 0.5%. Above this dose, the increase is less pronounced. A similar trend is observed for the interlayer spacing fluctuations σ. The in-plane coherent length L_a decreases linearly with the irradiation dose, while the coherent length L_c first increases by ~ 18% at a dose of ~ 1.5 dpa and then decreases for all specimens. The probability of random shift stacking faults P_{RS} increases, while the 3R stacking disorder decreases.

Table 5.1: Refined parameters for the specimens 12A-0 and 2A-2.2.

Parameters	12A-0			2A-2.2		
	Two-layer	Single-layer *floating g*	Single-layer $g = 0$	Two-layer	Single-layer *floating g*	Single-layer $g = 0$
$\langle a \rangle$ (Å)	2.4569 (1)	2.5672 (1)	2.4572 (1)	2.4574 (1)	2.4575 (1)	2.4576 (1)
$\langle d_{002} \rangle$ (Å)	3.3561 (1)	3.3562 (1)	3.3561 (1)	3.3712 (1)	3.3710 (1)	3.3712 (1)
L_a (Å)	236 (5)	250 (6)	250 (6)	186 (2)	193 (2)	192 (2)
L_c (Å)	274.5 (1.8)	299.9 (2.8)	274.4 (1.8)	284.9 (2.5)	667 (92)	285.1 (3.3)
P_{RS}	0.241 (8)	0.199 (9)	0.207 (9)	0.322 (7)	0.272 (2)	0.285 (7)
P_{3R}	0.061 (7)	-	-	0.035 (6)	-	-
g	-	0.967 (6)	0	-	0.937 (6)	0
σ (Å)	0.0612 (9)	0.58 (7)	0.086 (1)	0.0949 (7)	0.75 (6)	0.1343 (9)
χ^2	7.2	7.6	7.8	13.1	12.6	14.8
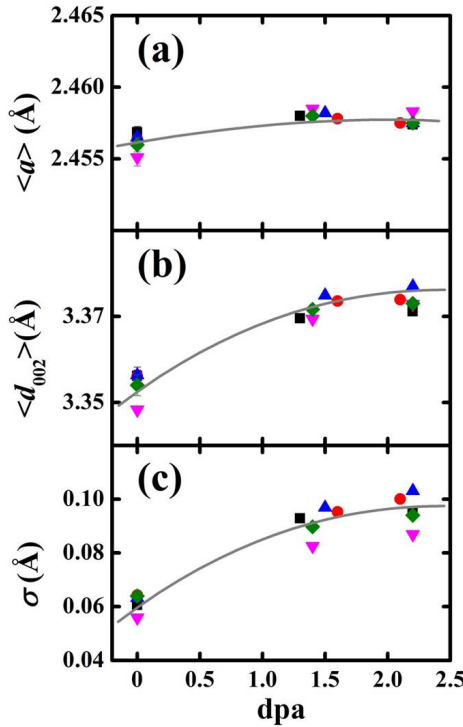
Figure 5.5: (a) The average in-plane lattice constant $\langle a \rangle$, (b) the average interlayer spacing $\langle d_{002} \rangle$ and (c) the standard deviation σ of d_{002} as a function of the irradiation dose for specimens respectively ■ A; ● B; ▲ C; ▼ D; ◆ E. The lines are guides to the eye.

With respect to the lattice parameters, similar results have been obtained for nuclear graphites irradiated at 650°C [4, 13, 14]. In addition, the increase of the interlayer spacing and the immutability of *a* have also been observed by electron microscopy during *in-situ* electron bombardment at 600°C [23].
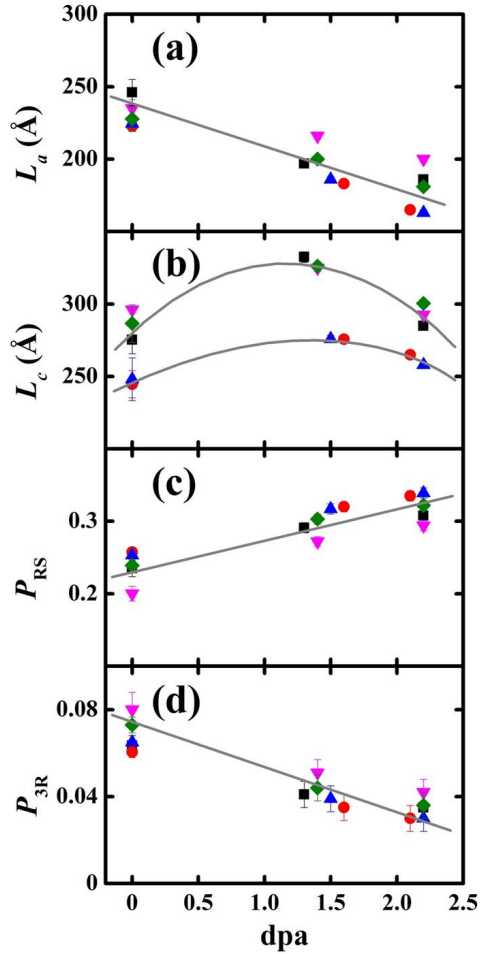
Figure 5.6: (a) The in-plane coherent length L_a, (b) the inter-plane coherent length L_c, and the probabilities of (c) random shift stacking faults P_{RS} and (d) 3R type stacking faults P_{3R} as a function of the irradiation dose for specimens respectively ■ A; ● B; ▲ C; ▼ D; ◆ E. The lines are guides to the eye.

In order to explain the increase in $\langle d_{002} \rangle$, a mechanism has been proposed [10] that involves the presence of displaced carbon atoms between carbon layers. These interstitials may deform the layers and thereby induce fluctuations in the local spacing observed by electron microscopy [7, 8], the extent of which is given by σ. Fig. 5.7(a) indeed shows the positive correlation between σ and $\langle d_{002} \rangle$, in which the data are plotted together with that from graphitic carbons [18] and several non-irradiated graphite samples [15]. As proposed by W. Ruland [24] and suggested in our previous work [15], in the plot of σ and $\langle d_{002} \rangle$ for different graphites, the data scatter relatively strongly and σ is not simply proportional to the difference between the average interlayer spacing $\langle d_{002} \rangle$ and the value for perfect graphite $d_{002}^{\text{crystal}} = 3.354$ Å, given by the dash line. This indicates
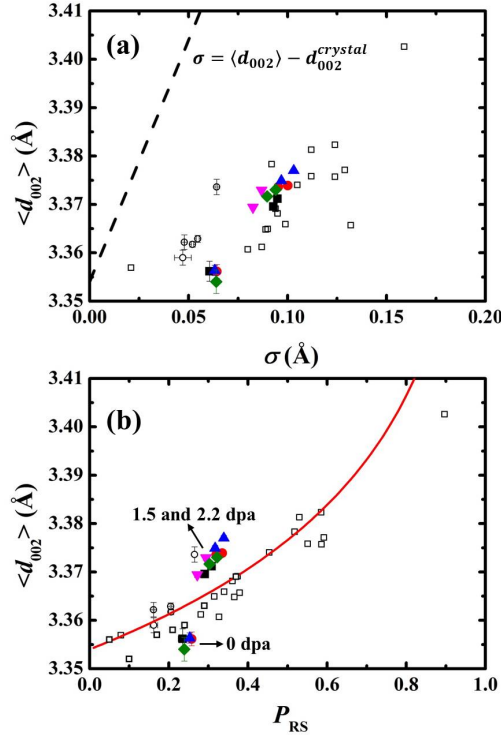
Figure 5.7: Average interlayer spacing $\langle d_{002} \rangle$ versus (a) the standard deviation σ of fluctuations in the interlayer spacing, and (b) the probability of random shift stacking faults P_{RS}. The colour solid symbols are for specimens ■ A; ● B; ▲ C; ▼ D; ◆ E. The open circles are from non-irradiated nuclear graphite specimens [15], the open squares from several graphitic carbons [18, 22]. The red line corresponds to Eq. 5.3.

that the disorder is not simply due to stacking faults, but also to other effects, such as dislocations, crosslinks, vacancies and interstitial defects. The scatter of the data could be partly attributed to basic differences in the types of disorder present in the various samples. However, in this work the data for the virgin and low doses irradiated graphite samples show a linear relationship between σ and $\langle d_{002} \rangle$. It is possible that the neutron irradiation disorders the structure in a genetic way for different nuclear graphites.

The behaviour of the coherent lengths shown in Fig. 5.6(a) and (b) is in agreement with the observations of electron microscopy [7–9], as illustrated in Fig. 5.8. At the dose of ∼ 1.5 dpa, L_a decreases because the graphite lattice of coherent regions tends to lose ordering in the basal plane, which is attributed to the induced in-plane defects, as well as the breaking, bending and displacement of the basal planes. However, L_c shows an increase at this low dose, which will be discussed below. On the one hand, the layered structure can be retained even after the irradiation of several dpa [8], which thus would not reduce the correlation length along c-axis. On the other hand, in the models L_c is given by $L_c = M \times \langle d_{002} \rangle$, with M the number of layers in the coherent region. Since
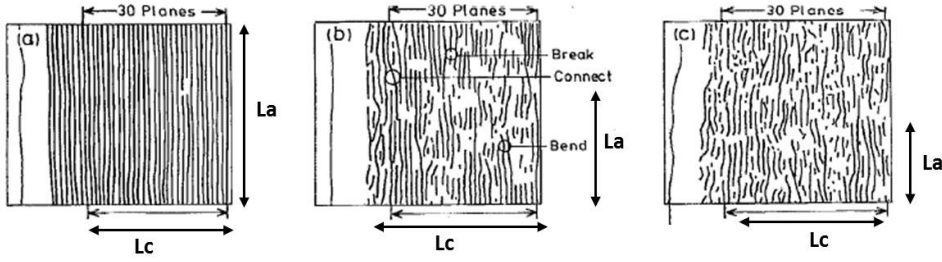
Figure 5.8: (after [8]) Visualization of the basal planes under electron irradiation observed by HRTEM. The coherent lengths L_a and L_c are illustrated in the figure.
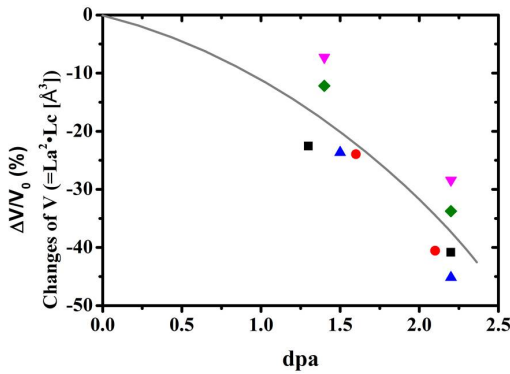
Figure 5.9: The relative changes of the size of coherent regions, which is obtained through $V = L_a^2 \cdot L_c$, as a function of the irradiation dose for specimens respectively ■ A; ● B; ▲ C; ▼ D; ◆ E. The line is a guide to the eye.

L_c and $\langle d_{002} \rangle$ increase by 18% and 0.5% respectively, M increases at this low irradiation dose. Possible mechanisms for this are (1) the formation of interstitial dislocation loops as observed by HRTEM [25] and (2) the closing of micro-cracks [25] between slightly disoriented coherent regions. When the irradiation dose increases from ∼ 1.5 to ∼ 2.2 dpa, L_c starts to decrease, which indicates that the extent of induced disorder leads to the fragmentation of coherent regions into smaller ones. This is similar to the TEM observations on a neutron irradiated highly oriented pyrolytic graphite (HOPG) [7].

We note that the changes of coherent lengths observed in this work differ with the dimensional changes in graphite crystals, i.e. elongation in the direction perpendicular and shrinkage parallel to the basal planes [2–6], and differ with bulk dimensional changes of the irradiated graphite as well, i.e. initial shrinkage of the volume at these low doses [21]. The bulk dimensional changes have been considered to be a convolution of the dimensional changes of the component crystals and the evolution of the porosity [26–28]. For modelling the bulk dimensional change, the behaviour of single graphite crystals during the irradiation conditions is in need of [29]. However, the co-

herent lengths obtained in X-ray diffraction are the average size of the regions within which X-rays scatter coherently, and thus they are different with, or more accurately, smaller than the dimensional of the crystals. This is also revealed by the significant relative change of the size of coherent regions $V = L_a^2 \cdot L_c$, as shown in Fig. 5.9, which is up to 40% at the dose of ~ 2.2 dpa, while the bulk dimensional change for the irradiated samples is only 0.6% [21]. Therefore, we suggest that the microscopic structural changes observed from X-ray diffraction could be hardly related to the volume change at the macroscopic scale.

The increase of P_{RS} seen in Fig. 5.6(c) is mainly due to the loss of the ABAB stacking sequence. In addition, half of the ABC stacked regions are converted into regions with turbostratic disorder (see Fig. 5.6(d)).

In our previous work [15] we validated a simple relation between $\langle d_{002} \rangle$ and P_{RS} :

$$\langle d_{002} \rangle = d_{002}^{\text{crystal}} - 0.0326 \ln(1 - P_{RS}), \tag{5.3}$$

which is illustrated by the solid line in Fig. 5.7(b). Besides the result of the irradiated samples, this figure also includes data from non-irradiated graphites [15] and other graphitic carbons [18, 22]. Surprisingly, the data of the irradiated samples deviate from Eq. 5.3, which indicates that for these specimens other types of disorder beyond the random stacking faults, such as dislocation loops or the bending of basal planes, should be taken into account as well.

5.5. CONCLUSIONS

The analysis approach adopted in this work enables quantification of the neutron irradiation effects on the atomic structure of graphite. It turns out even low neutron irradiation doses lead to substantial changes of the structural parameters, such as lattice constants, coherent lengths and stacking faults. The extension of this approach to highly irradiated graphites will certainly lead to a better understanding of the structural changes and the resulting modifications of the physical properties.

ACKNOWLEDGEMENTS

SUPPLEMENT

REFINEMENT RESULTS FROM THE TWO-LAYER MODEL

All the refined parameters of the two-layer model for all specimens in this work are listed in Table 5.2.

Table 5.2: Refined parameters of the two-layer model for all specimens.

Sample	$\langle a \rangle$ (Å)	$\langle d_{002} \rangle$ (Å)	L_a (Å)	M	L_c (Å)	P_{RS}	P_{3R}	σ (Å)
1A-1.3	2.4580 (1)	3.3696 (1)	197 (2)	99 (1)	332.4 (3.7)	0.291 (7)	0.041 (6)	0.0929 (7)
2A-2.2	2.4574 (1)	3.3712 (1)	186 (2)	85 (1)	284.9 (2.5)	0.308 (7)	0.035 (6)	0.0949 (7)
3B-1.6	2.4578 (1)	3.3736 (1)	183 (2)	82 (1)	275.6 (2.3)	0.320 (7)	0.035 (6)	0.0953 (7)
4B-2.1	2.4575 (1)	3.3739 (1)	165 (2)	79 (1)	265.0 (2.3)	0.335 (7)	0.030 (6)	0.1001 (7)
5C-1.5	2.4582 (1)	3.3749 (1)	186 (2)	82 (1)	275.9 (2.5)	0.317 (7)	0.039 (6)	0.0969 (7)
6C-2.2	2.4575 (1)	3.3770 (1)	163 (2)	76 (1)	258.0 (2.5)	0.339 (7)	0.030 (6)	0.1031 (7)
7D-1.4	2.4585 (1)	3.3694 (1)	216 (2)	96 (1)	324.9 (2.4)	0.272 (7)	0.051 (6)	0.0825 (7)
8D-2.2	2.4583 (1)	3.3729 (1)	200 (2)	87 (1)	292.6 (2.0)	0.294 (7)	0.042 (6)	0.0869 (7)
9E-1.4	2.4580 (1)	3.3717 (1)	200 (2)	97 (1)	326.1 (3.0)	0.303 (7)	0.044 (6)	0.0897 (7)
10E-2.2	2.4575 (1)	3.3730 (1)	181 (2)	89 (1)	300.4 (2.8)	0.322 (7)	0.036 (6)	0.0940 (7)
11D-0	2.4551 (6)	3.3484 (1)	235 (6)	88 (1)	296.1 (2.2)	0.20 (1)	0.080 (8)	0.0559 (9)
12A-0	2.4569 (1)	3.3561 (1)	236 (5)	82 (1)	275.3 (1.8)	0.233 (8)	0.066 (7)	0.0608 (9)
13A-0	2.4569 (1)	3.3563 (1)	249 (5)	84 (1)	280.8 (1.8)	0.232 (8)	0.064 (7)	0.0607 (8)
14A-0	2.4573 (1)	3.3587 (1)	257 (6)	84 (1)	283.5 (2.0)	0.251 (8)	0.057 (7)	0.0618 (9)
15A-0	2.4563 (1)	3.3536 (1)	242 (5)	78 (1)	261.7 (1.4)	0.224 (8)	0.067 (7)	0.0591 (8)
16B-0	2.4567 (1)	3.3568 (1)	227 (5)	73 (1)	244.4 (1.4)	0.261 (9)	0.061 (7)	0.0636 (8)
17B-0	2.4560 (1)	3.3542 (1)	220 (5)	70 (1)	234.3 (1.3)	0.253 (9)	0.061 (7)	0.0639 (9)
18B-0	2.4564 (1)	3.3575 (1)	220 (4)	72 (1)	242.8 (1.4)	0.251 (8)	0.063 (7)	0.0643 (9)
19B-0	2.4564 (1)	3.3561 (1)	224 (5)	77 (1)	257.0 (1.6)	0.265 (9)	0.057 (7)	0.0654 (8)
20C-0	2.4563 (1)	3.3556 (1)	224 (5)	71 (1)	237.6 (1.3)	0.254 (9)	0.065 (7)	0.0626 (9)
21C-0	2.4567 (1)	3.3571 (1)	225 (4)	77 (1)	258.5 (1.5)	0.252 (8)	0.065 (7)	0.0639 (8)
22E-0	2.4566 (1)	3.3568 (1)	237 (3)	90 (1)	300.4 (1.2)	0.242 (7)	0.069 (6)	0.0626 (7)
23E-0	2.4557 (1)	3.3529 (1)	220 (3)	85 (1)	284.7 (1.1)	0.238 (7)	0.074 (6)	0.0647 (7)
24E-0	2.4557 (1)	3.3524 (1)	226 (3)	82 (1)	274.6 (1.0)	0.237 (7)	0.076 (6)	0.0646 (7)

FITS OF IRRADIATED GRAPHITE SAMPLES UNDER OXIDISING CONDITIONS

Fig. 5.10 displays measured and calculated X-ray diffraction patterns for the irradiated graphite samples 0M02 and 0M16 from Project Blackstone [30], in which the samples have received neutron irradiation combined with simultaneous radiolytic oxidation. The diffraction pattern for the sample 0M02 is very similar to the measured profiles of the low dose irradiated graphite samples shown in the manuscript. The refinement results show that the two-layer model provides a better fit than the single-layer model as observed in the manuscript. On the other hand, the diffraction peaks for the sample 0M16 are very broad indicating a highly disordered structure, which is attributed to a high irradiation dose and/or a high oxidation. In this case, the single-layer model is also adequately capable to reproduce the measured X-ray diffraction pattern as the two-layer model. Therefore, we demonstrate that the single-layer model might be more promising for high dose irradiated graphite specimens.
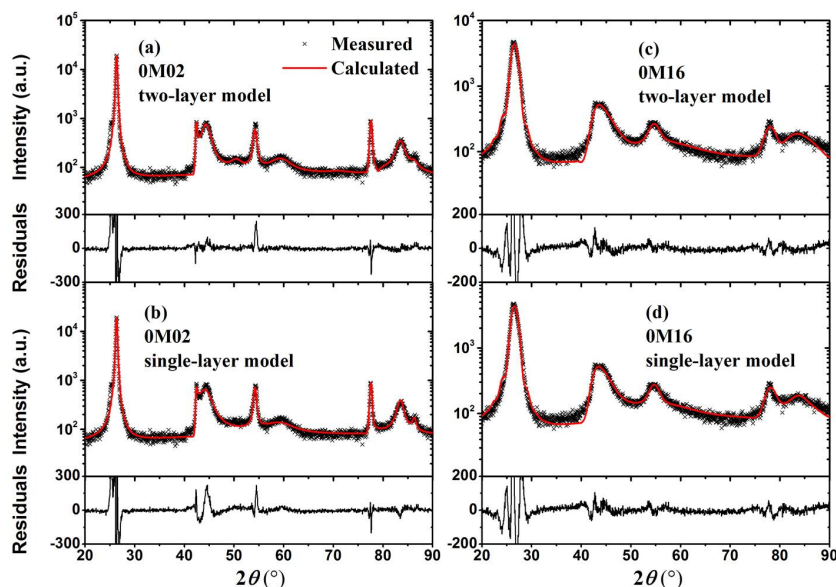
Figure 5.10: Measured and calculated XRD patterns and residuals for the irradiated graphite samples under oxidising conditions 0M02 and 0M16. The data were fitted using the program CARBONXS with the two-layer model and the single-layer model for comparison.

REFERENCES

[1] Z. Zhou, W. G. Bouwman, H. Schut, T. van Staveren, M. Heijna, and C. Pappas, *Influence of neutron irradiation on the microstructure of nuclear graphite: An x-ray diffraction study,* (2016), in preparation.

[2] B. T. Kelly, W. H. Martin, and P. T. Nettley, *Dimensional Changes in Pyrolytic Graphite under Fast-Neutron Irradiation,* Philosophical Transactions of the Royal Society A: Mathematical, Physical and Engineering Sciences **260**, 37 (1966).

[3] B. Kelly and J. Brocklehurst, *High dose fast neutron irradiation of highly oriented pyrolytic graphite,* Carbon **9**, 783 (1971).

[4] P. R. Goggin, R. W. Henson, A. J. Perks, and W. N. Reynolds, *Dimensional changes in the irradiated graphite lattice,* Carbon **1**, 189 (1964).

[5] B. Kelly, *The theory of irradiation damage in graphite,* Carbon **15**, 117 (1977).

[6] T. D. Burchell and L. L. Snead, *The effect of neutron irradiation damage on the properties of grade nbg-10 graphite,* Journal of Nuclear Materials **371**, 18 (2007).

[7] A. Asthana, Y. Matsui, M. Yasuda, K. Kimoto, T. Iwata, and K. Ohshima, *Investigations on the structural disordering of neutron-irradiated highly oriented pyrolytic graphite by x-ray diffraction and electron microscopy,* Journal of Applied Crystallography **38**, 361 (2005).

[8] T. Tanabe, S. Muto, and K. Niwase, *On the mechanism of dimensional change of neutron-irradiated graphite,* Applied Physics Letters **61**, 1638 (1992).

[9] T. Tanabe, S. Muto, Y. Gotoh, and K. Niwase, *Reduction of the crystalline size of graphite by neutron irradiation,* Journal of Nuclear Materials **175**, 258 (1990).

[10] G. E. Bacon and B. E. Warren, *X-ray diffraction studies of neutron-irradiated graphite,* Acta Crystallographica **9**, 1029 (1956).

[11] B. T. Kelly, D. Jones, and A. James, *Irradiation damage to pile grade graphite at 450 °C,* Journal of Nuclear Materials **7**, 279 (1962).

[12] R. W. Henson and W. N. Reynolds, *Lattice parameter changes in irradiated graphite,* Carbon **3**, 277 (1965).

[13] R. W. Henson, A. J. Perks, and J. H. W. Simmons, *Lattice parameter and dimensional changes in graphite irradiated between 300 and 1350 °C,* Carbon **6**, 789 (1968).

[14] B. P. Richards and E. A. Kellett, *Changes in structure of graphite on irradiation under restraint,* Journal of Nuclear Materials **25**, 45 (1968).

[15] Z. Zhou, W. G. Bouwman, H. Schut, and C. Pappas, *Interpretation of x-ray diffraction patterns of (nuclear) graphite,* Carbon **69**, 17 (2014).

[16] H. Shi, J. N. Reimers, and J. R. Dahn, *Structure-refinement program for disordered carbons,* Journal of Applied Crystallography **26**, 827 (1993).

[17] H. Shi, *Disordered carbons and battery applications*, Phd (1993).

[18] V. S. Babu and M. S. Seehra, *Modeling of disorder and x-ray diffraction in coal-based graphitic carbons,* Carbon **34**, 1259 (1996).

[19] D. D. Dijulio and A. I. Hawari, *Examination of reactor grade graphite using neutron powder diffraction,* Journal of Nuclear Materials **392**, 225 (2009).

[20] J. a. Vreeling, O. Wouters, and J. G. V. D. Laan, *Graphite irradiation testing for htr technology at the high flux reactor in petten,* Journal of Nuclear Materials **381**, 68 (2008).

[21] M. Heijna, *The innograph-1c low dose irradiation experiment: extending the htr graphite materials properties curves at 750° C,* Presentation at the 15th International Nuclear Graphite Specialists Meeting, Hangzhou, China (2014).

[22] T. Zheng and J. R. Dahn, *The effect of turbostratic disorder on the staging transitions in lithium intercalated graphite,* Synthetic Metals **73**, 1 (1995).

[23] B. A. Gurovich and K. E. Prikhodko, *Investigation of dose-temperature dependencies of graphite dimensional and lattice parameters changes under electron irradiation,* Radiation Effects and Defects in Solids **154**, 39 (2001).

[24] W. Ruland, *X-ray studies on the structure of graphitic carbons,* Acta Crystallographica **18**, 992 (1965).

[25] C. Karthik, J. Kane, D. P. Butt, W. E. Windes, and R. Ubic, *In situ transmission electron microscopy of electron-beam induced damage process in nuclear grade graphite,* Journal of Nuclear Materials **412**, 321 (2011).

[26] J. H. W. Simmons, *Radiation Damage in Graphite: International Series of Monographs in Nuclear Energy,* Vol. 102 (Elsevier, 2013).

[27] G. B. Neighbour, *Modelling of dimensional changes in irradiated nuclear graphites,* J Phys D Appl Phys **33**, 2966 (2000).

[28] J. E. Brocklehurst and B. T. Kelly, *Analysis of the dimensional changes and structural changes in polycrystalline graphite under fast neutron irradiation,* Carbon **31**, 155 (1993).

[29] G. Hall, B. J. Marsden, and S. L. Fok, *The microstructural modelling of nuclear grade graphite,* Journal of Nuclear Materials **353**, 12 (2006).

[30] M. Brooking, *Project blackstone: Graphite irradiation in a materials test reactor,* Unpublished work (2014).

6

NEUTRON DIFFRACTION PATTERNS AND INTERPRETATION

Neutron diffraction measurements on (nuclear) graphite samples are presented in this Chapter, and the data were analysed using the two-layer model applied for XRD in Chapter 4 and 5. The obtained refined parameters were compared with that from X-ray diffraction and the discrepancy in these two techniques was discussed. The results show that the structure of powder samples is deteriorated when scrapping the bulk material, indicated by the smaller coherent lengths and more stacking faults.

6.1. Introduction

In Chapter 4 and 5, X-ray diffraction patterns from the virgin and irradiated (nuclear) graphite samples are well interpreted using Shi's model and program CARBONXS. The methodology applied in our previous work has been demonstrated to be superior to the conventional Rietveld method because the effects of structural disorder and the penetration depth of X-rays on the shape of the diffraction peaks are taken into account in the refinement. Besides the lattice parameters, the disorder properties can be quantified.

In X-ray diffraction, due to the atomic scattering factor of carbon for X-rays, the intensities of diffraction peaks fall off seriously at high scattering angle, and the (002) peak dominates the measured diffraction pattern. As already mentioned, the fit of the X-ray diffraction patterns to the model is thus mainly governed by the most intensive (002) peak. It is probable that the refined parameters are mostly determined by an individual peak instead of the whole diffraction pattern. In addition, the high penetration depth of X-rays broadens the diffracted peaks asymmetrically. For a proper estimation of this effect in the program CARBONXS, samples for the measurements must be flat plates and the incident beam slits must be chosen so that the beam does not extend beyond the edges of the sample at any angle. Thus the dimension and density of the sample, the beam width and the goniometer radius of the diffractometer must be supplied to take the absorption into account. This may make it tricky to perform the experiments and to obtain an accurate evaluation of the experimental effect.

To evaluate these effects on the obtained structural information, in this work neutron diffraction measurements have been performed on the (nuclear) graphite samples. Since the scattering power of atoms for neutrons is independent on the scattering angle, the diffractograms can show strong well defined diffraction peaks even at high angles. Besides, because of the negligible absorption cross section of carbon for neutrons, the effect of beam absorption can be neglected. In a previous work by DiJulio and Hawari [1], a nuclear graphite has been studied by neutron diffraction and the data were refined by Shi's model. However, the instrumental resolution was not included in the calculation of the diffraction pattern, which is essential to obtain more accurate structural parameters in neutron diffraction experiments. In this work, the resolution of the neutron diffractometer has been successfully included in the program CARBONXS, and the measured diffraction patterns were refined using Shi's two-layer model. Moreover, the resulted parameters have been compared with that from XRD shown in Chapter 4. In addition, the differences in the structure of bulk and powder samples were examined.

6.2. Experimental

Three types of nuclear graphites (PCEA, PGA and RID) and a non-nuclear graphite (1940 PT) were investigated and these graphites have been introduced in Chapter 2. In this work, both powder and bulk samples were measured. The powder samples were collected by scrapping the bulk material with a file, and the bulk samples have a disk shape with a diameter of 20 mm and a thickness of 2 mm.

Neutron diffraction experiments were performed on the instrument 3T2, a high resolution powder diffractometer in Laboratoire Léon Brillouin (LLB), Saclay. The incident neutron wavelength 1.225 Å, and the diffraction patterns for 2θ from 15° to 110° were

collected with interval of 0.05°. In the measurements, the powder material was filled in a cylindrical vanadium sample holder, while the bulk samples were placed directly on the sample stage. To investigate the geometry effect of the flat-plate sample, the bulk samples were measured in two geometries, as illustrated in Fig. 6.1. The measurements configurations are listed in Table. 6.1, where the statistics is the incident beam monitor counts.
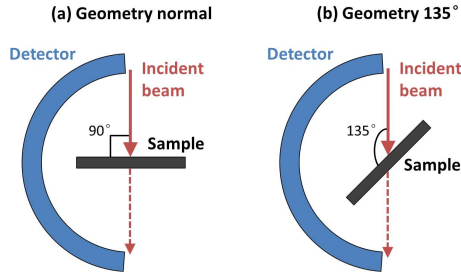
Figure 6.1: Two geometries applied for the neutron diffraction measurements on the bulk samples: the angle between the incident beam and the flat plane of the disk sample is (a) 90° (Geometry normal) or (b) 135° (Geometry 135°).

Table 6.1: The measurements configurations in neutron diffraction.

Graphite	Sample	Geometry	Statistics
PCEA	Powder	-	135000
	Bulk	normal	129000
PGA	Powder	-	89000
	Bulk	normal	129000
	Bulk	135°	64500
RID	Powder	-	89000
	Bulk	135°	129000
1940 PT	Powder	-	126000
	Bulk	135°	129000

6.3. ANALYSIS OF NEUTRON DIFFRACTION PATTERNS

The measured neutron diffraction patterns were analysed by the two-layer model and the refinement program CARBONXS from Shi [2], which we have introduced in Chapter 4 and 5. To do so, several modifications were made on CARBONXS because it is specific for describing XRD patterns and there are several differences in the formulation for X-ray and neutron diffraction. The atomic scattering factor for X-rays was replaced by the neutron scattering length for carbon; the polarization correction for X-rays was removed; the computation for the effect of penetration depth of X-rays was taken out because of negligible absorption cross section of neutrons for carbon.

In addition, it is important to include the instrumental resolution in the calculation

of the neutron diffraction pattern. Fig. 6.2(a) shows the resolution curve of 3T2 diffractometer given by the Full Width of Half Maximum (FWHM) of Cagliotti profile as a function of scattering angle 2θ. It indicates that the broadening of the diffraction pattern resulted from the instrument varies between $\sim 0.2°$–$0.6°$ as a function of 2θ. The resolution function profile can then be calculated according to the value of FWHM at a specific 2θ, as shown the resolution function profile at $2\theta = 20°$ in Fig. 6.2(b). Accordingly, the effect of the instrumental resolution was taken into account by including a convolution of the calculated diffraction pattern and the resolution function in the program CARBONXS.
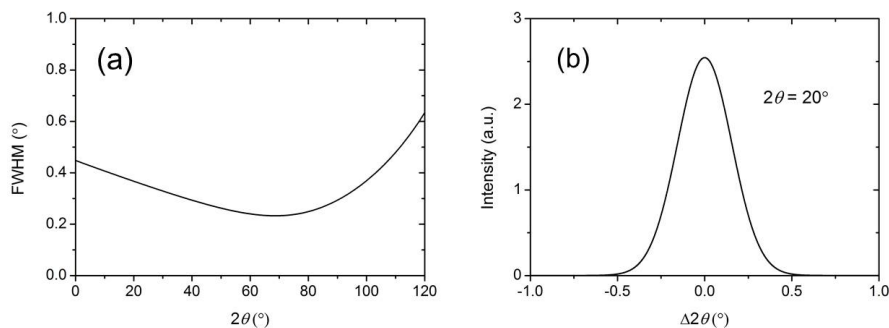
Figure 6.2: (a) 3T2 instrumental resolution curve given by the Full Width of Half Maximum of Cagliotti profile as a function of scattering angle 2θ. (b) Resolution function profile at $2\theta = 20°$.

6.4. RESULTS AND DISCUSSION

6.4.1. GEOMETRY EFFECT

Fig. 6.3 displays the neutron diffraction patterns from the bulk sample of PGA using two different geometry options. Both diffraction patterns show the same position and broadening for each Bragg peak, indicating identical structural information. However, the experimental geometry does influence the relative intensities of diffracted peaks, which is attributed to the preferred orientation in this anisotropic sample.

6.4.2. COMPARISON OF NEUTRON AND X-RAY DIFFRACTION

A comparison of neutron and X-ray diffraction measurements for the PCEA bulk sample is given in Fig. 6.4. In this figure, the measured diffraction intensities (crosses) from both methods have been normalized and are plotted as a function of d-spacing, which is determined by the incident beam wavelength λ and the diffraction angle 2θ, given by $d = \lambda/2\sin\theta$. In X-ray diffraction, the intensities of Bragg peaks drop off significantly as d-spacing decreases because the atomic form factor, which describes the scattering power of an atom for X-rays, decreases at high scattering angles 2θ (i.e. low d-spacing). However, since neutrons are scattered from the nucleus and the form factor is not angle dependent, the neutron diffraction can show strong and well defined Bragg peaks even at the entire range of d-spacing. Moreover, in this work neutron diffraction pattern covers broader d-spacing range providing additional Bragg peaks because the wavelength
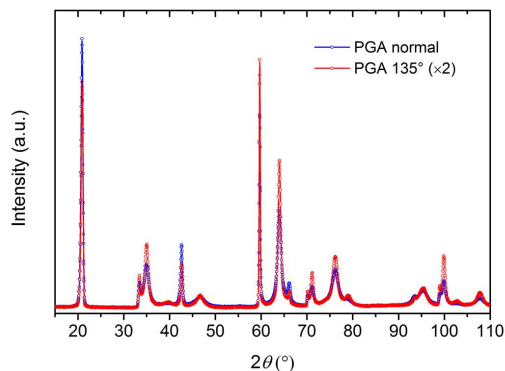
Figure 6.3: The neutron diffraction patterns of PGA bulk sample using different experimental geometries. Since the measurement with geometry 135° was performed with half of the statistics as obtained with geometry normal (see Table 6.1), the intensities of the former pattern are multiplied by 2 for comparison.

of neutrons (1.225 Å) is shorter than that of X-rays (1.542 Å) in the diffraction measurements.
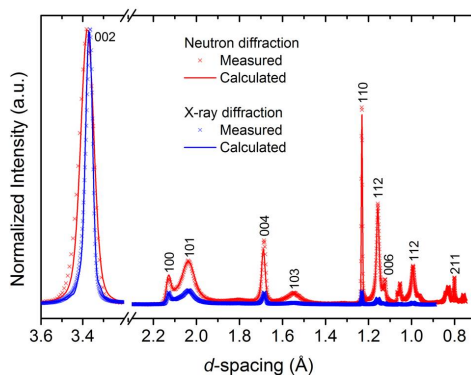
Figure 6.4: The normalized measured neutron and X-ray diffraction patterns for the PCEA bulk sample, represented by the crosses. The data were refined by the two-layer model and program CARBONXS and the solid lines correspond to the fitted patterns.

It is important to mention that the neutron diffraction peaks are much broader than those in the X-ray diffraction pattern, as shown clearly the (002) peaks in Fig. 6.4. This is because that the neutron diffractometer resolution makes an important contribution to the broadening of the peaks and will be discussed later.

In Fig. 6.4, the solid lines show the fitting of both neutron and X-ray diffraction patterns using Shi's two-layer model. Although it seems that both measured patterns are reproduced fairly well, the refined parameters for each graphite sample, as listed in Table 6.2, are different between the two diffraction methods. To clarify the discrepancies,

Neutron diffraction
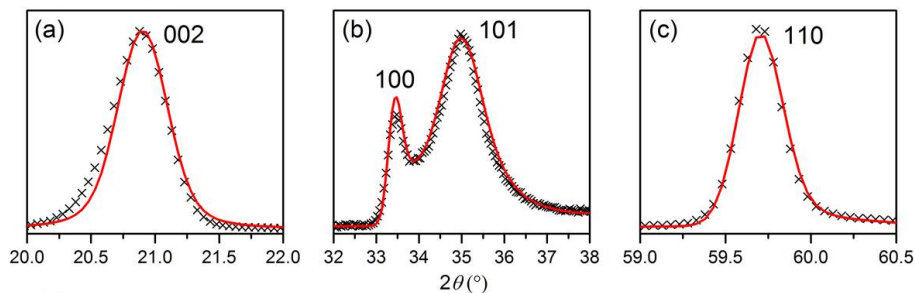
X-ray diffraction
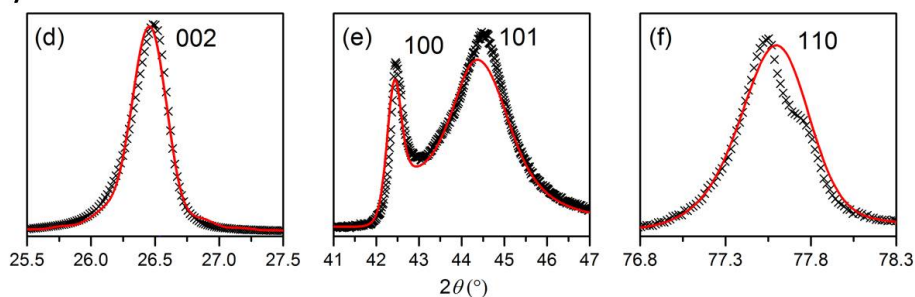
Figure 6.5: Measured (×) and calculated (red line) neutron (a-c) and X-ray (d-f) diffraction patterns at selected regions revealing the fitting details.

the fitting of measured diffraction patterns at several selected regions for the PCEA bulk sample are displayed in Fig. 6.5. (a) and (d) show that the (002) peak broadening for the neutron diffraction is ~ 0.50°, which is much larger than ~ 0.32°, the value for X-rays. The peak broadening in diffraction experiments arises from the instrumental contribution and the sample. In neutron diffraction, as shown in Fig. 6.2, the FWHM of the instrumental resolution function at $2\theta = 21°$ is ~ 0.36°, indicating more than 70% of the (002) peak broadening is attributed to the 3T2 diffractometer. Therefore, it is important to include the instrumental resolution in the neutron diffraction analysis to obtain reliable structural parameters. However, in X-ray diffraction the instrumental broadening is typically less than 0.03°, which is less than 10% of the total broadening of the Bragg peaks and thus can be neglected.

In Fig. 6.5 (a) and (d), the (002) peak in the neutron diffraction appears more symmetric than that in the X-rays. This is because in X-ray diffraction, besides the beam divergence, the high penetration depth of X-rays in the graphite sample causes asymmetric Bragg peaks as well. Even though an estimation of the absorption effect has been taken into account, it seems that the refinement program CARBONXS does not completely succeed in reproducing the asymmetric shape of the (002) peak from X-ray diffraction. The mismatch observed between the calculated and measured (002) peak may lead to inaccurate determination of the peak position and consequently the lattice parameters. Instead, the asymmetry effect can be ignored in neutron diffraction because graphite has a negligible absorption cross section for neutrons. Therefore, the (002) peak shape is

almost symmetric and can be easily reproduced by CARBONXS.

In Fig. 6.5(f), a splitting of the (110) peak can be observed, which is attributed to the presence of both Cu $K_{\alpha 1}$ and $K_{\alpha 2}$ wavelengths of the X-rays. This effect becomes especially important for the narrow diffraction peaks at high scattering angles, e.g. the (110) peak. For this reason, a poor fit was obtained and the (110) peak broadening is overestimated in the X-ray diffraction. However, as shown in Fig. 6.5(c), the neutron diffraction pattern shows a well defined single peak of (110) that is reproduced perfectly by CARBONXS. Since the coherent length L_a is mainly determined from the broadening of $hk0$ peaks, the XRD fitting results lead to smaller values of L_a compared with the neutrons data (see Table 6.2).

Moreover, the shape and intensities of the (100) and (101) peaks are reproduced more accurately in neutron diffraction analysis than that in X-rays, as shown in Fig. 6.5 (b) and (e), representing an epitome of the overall fits. We thus demonstrate that a relatively higher quality of fit can be achieved in the neutron diffraction analysis, which will consequently lead to more reliable quantification of the structural information.

Table 6.2: The refined parameters from fitting using Shi's two-layer modle and the program CARBONXS.

	Sample	χ^2	$\langle a \rangle$	$\langle d_{002} \rangle$	L_a	M	L_c	σ	P_{RS}	P_{3R}
Bulk	PCEA	7.6	2.4625(1)	3.3774(1)	366(5)	78(1)	265.1(4.5)	0.0494(9)	0.208(1)	0.070(1)
			2.4588(3)*	3.3617(6)*	231.5(2.6)*	94.8(0.6)*	318.8(2.1)*	0.0520(5)*	0.206(6)*	0.073(2)*
	PGA	11.8	2.4623(1)	3.3712(1)	439(8)	152(4)	511.3(15.1)	0.0481(8)	0.156(1)	0.069(1)
			2.4596(3)*	3.3590(15)*	244.0(3.4)*	115.6(8.4)*	388.2(28.2)*	0.0471(4)*	0.162(10)*	0.065(4)*
	RID	19.4	2.4626(1)	3.3737(1)	445(5)	151(3)	508.8(11.7)	0.0527(7)	0.165(1)	0.066(1)
			2.4602(2)*	3.3622(15)*	245.5(0.7)*	107.7(0.1)*	362.2(0.4)*	0.0479(1)*	0.162(1)*	0.068(1)*
	1940 PT	14.9	2.4627(1)	3.3870(1)	308(3)	69(1)	234.5(2.8)	0.0604(8)	0.273(1)	0.063(1)
			2.4599(4)*	3.3736(16)*	209(1)*	74.8(0.4)*	252.4(1.4)*	0.0642(4)*	0.265(1)*	0.067(1)*
Powder	PCEA	9.5	2.4612(1)	3.3774(1)	272(3)	50(1)	170.5(1.7)	0.0524(9)	0.243(1)	0.087(1)
	PGA	7.4	2.4611(1)	3.3715(6)	346(4)	65(1)	218.4(3.6)	0.047(1)	0.180(1)	0.094(1)
	RID	12.2	2.4612(1)	3.3727(1)	320(3)	61(1)	205.7(2.3)	0.047(1)	0.186(1)	0.092(1)
	1940 PT	3.5	2.4608(1)	3.3821(6)	263(4)	49(1)	164.2(2.3)	0.058(1)	0.292(6)	0.068(6)

* Values from XRD analysis

6.4.3. DIFFERENCES BETWEEN BULK AND POWDER SAMPLES

The neutron diffraction patterns of the bulk and powder samples for different graphites have been analysed using Shi's two-layer model and program CARBONXS. The obtained parameters are listed in Table 6.2, by which the differences in the structure of bulk and powder samples are revealed.

Fig.6.6 displays the refined values of the interlayer spacing $\langle d_{002} \rangle$ and the in-plane lattice parameters $\langle a \rangle$. For each type of graphite the powder and bulk samples show very similar lattice constants. As we have observed in 4, $\langle a \rangle$ varies within 0.1% around the value of single crystalline graphite 2.461 Å due to the strong covalent bonding in the basal plane. The interlayer spacing $\langle d_{002} \rangle$ varies for different graphite and the value of 1940 PT is much higher than the nuclear graphites.

Fig. 6.7 displays the standard deviation σ of fluctuations in the interlayer spacing as a function of $\langle d_{002} \rangle$. Although no trend is observed in σ for the bulk and powder samples, an increase of σ with $\langle d_{002} \rangle$ is expected.
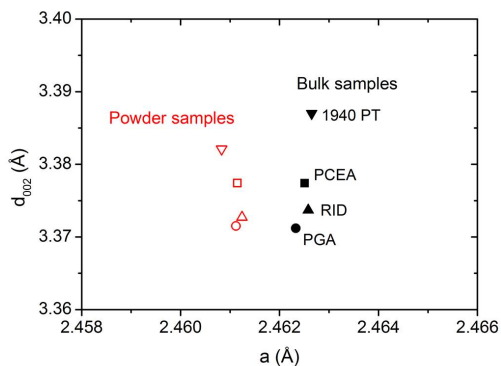
Figure 6.6: Refined average interlayer spacing $\langle d_{002} \rangle$ and the in-plane lattice constant $\langle a \rangle$ for the bulk and powder samples.
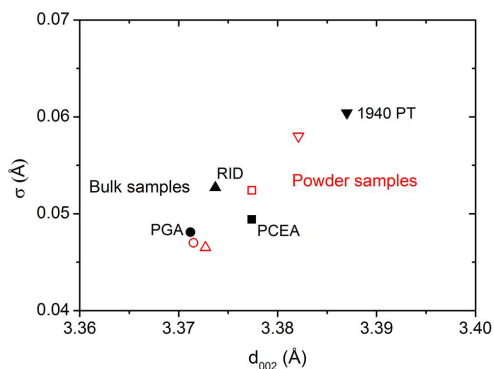
Figure 6.7: Refined standard deviation σ of fluctuations in the interlayer spacing plotted against $\langle d_{002} \rangle$

Fig. 6.8 displays refined values of the coherent lengths L_a and L_c. Both L_a and L_c for the bulk samples vary for different graphites, among which the non-nuclear graphite 1940 PT has the smallest average size of the coherent regions within the structure. This is expected because nuclear graphites require high degree of order containing more perfect layered structures thus larger coherent lengths both in the basal plane and between planes.

A significant difference in the coherent lengths between the bulk and powder samples can be observed in Fig. 6.8. For each graphite, the powder sample has much smaller L_a and L_c than the bulk sample has. It indicates that when scratching the graphite bulk material, some of the coherent regions in the structure may be broken into smaller ones during the mechanical treatment. In addition, the powder samples contain more stacking faults of both random shift P_{RS} and 3R type P_{3R} than the bulk samples, as shown in Fig. 6.9. Similar findings have been demonstrated by G.E. Bacon [3, 4] that for well-
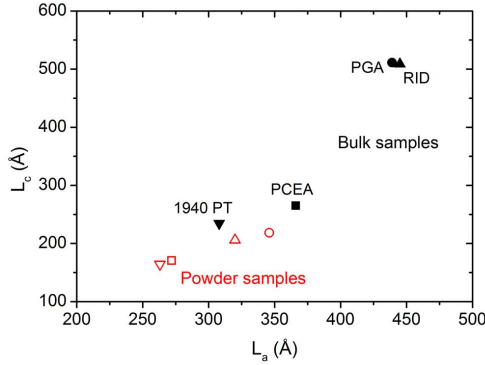
Figure 6.8: Refined coherent lengths L_a and L_c for the bulk and powder samples.

crystallized graphite when the bulk material is reduced to powder by continued grinding, the proportion of ABC structure, i.e. 3R stacking faults, and the probability of layer displacement, i.e. random shift stacking faults, will increase; the coherent lengths both in plane and between planes will decrease. Our results show that like grinding, the scratching treatment can also deteriorate the crystalline perfection of graphite.
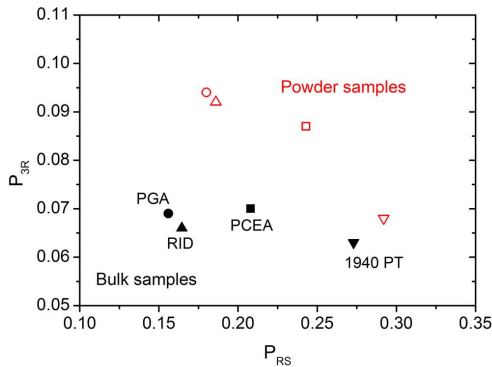
Figure 6.9: Refined stacking disorder parameters P_{RS} and P_{3R} for the bulk and powder samples.

6.5. CONCLUSIONS

The results and analysis presented in this work have demonstrated that the instrumental resolution can be successfully included in Shi's model and the refinement program CARBONXS to interpret the neutron diffraction patterns of graphite samples. Compared with X-ray diffraction, due to the absence of the influence of beam absorption and dual-wavelength, neutron diffraction produces more symmetric Bragg peaks that can be reproduced by Shi's model perfectly, thus leading to more reliable structural parameters.

The results also show the difference in the structure between bulk and powder samples indicating the scratching treatment can deteriorate the crystalline perfection in graphite.

REFERENCES

[1] D. DiJulio and A. Hawari, *Examination of reactor grade graphite using neutron powder diffraction,* Journal of Nuclear Materials **392**, 225 (2009).

[2] H. Shi, J. Reimers, and J. Dahn, *Structure-refinement program for disordered carbons,* Journal of applied crystallography **26**, 827 (1993).

[3] G. Bacon, *A note on the rhombohedral modification of graphite,* Acta Crystallographica **3**, 320 (1950).

[4] G. Bacon, *The reduction of the crystalline perfection of graphite by grinding,* Acta Crystallographica **5**, 392 (1952).

7

FROM NANOPORES TO MACROPORES: FRACTAL MORPHOLOGY OF GRAPHITE

We present a comprehensive structural characterization of two different highly pure nuclear graphites that compasses all relevant length scales from nanometers to sub-mm. This has been achieved by combining several experiments and neutron techniques: Small Angle Neutron Scattering (SANS), high-resolution Spin Echo SANS (SESANS) and neutron imaging. In this way it is possible to probe an extraordinary broad range of 6 orders of magnitude in length from microscopic to macroscopic length scales. The results reveal a fractal structure that extends from ~ 0.6 nm to 0.6 mm and has surface and mass fractal dimensions both very close to 2.5, a value found for percolating clusters and fractured ranked surfaces in 3D.

7.1. Introduction

Graphite has been used as a neutron moderator in several types of nuclear reactors from the Chicago Pile 1 in 1942 to the more recent Very High Temperature Reactor (VHTR) and High Temperature Gas-cooled Reactors (HTGR). This synthetic polygranular material has a very high chemical purity and a complex microstructure, which affects the mechanical properties under extreme conditions and irradiation damage [2].

The crystallite structure and disorder of graphite at the atomic level can be investigated by neutron or X-ray diffraction [3], and the microstructure by TEM, SEM or optical microscopy [4–8]. On the other hand, the bulk mesoscopic structure of the pores can be explored by small angle scattering of X-rays (SAXS) or neutrons (SANS) [9]. Very first SANS measurements on non-irradiated and irradiated nuclear graphites were performed in the 1960's [10] and 1970's [11–13]. These results have been reinterpreted recently [14] to disclose a surface fractal structure from ~ 0.2 to 300 nm, i.e. over three orders of magnitude in length. However, the graphite inhomogeneities can be seen with an optical microscope or even with naked eye. Therefore an exploration over a larger range of length scales is necessary and for this purpose we have combined three neutron-based techniques: SANS, Spin Echo SANS (SESANS) and imaging to cover lengths from nm to mm. We investigated two different highly pure nuclear graphites, and the results show a fractal structure over an extraordinary large scale of lengths that spans 6 orders of magnitude and has fractal dimensions close to 2.5. This value is expected for several cases of percolating clusters [15, 16] and in the most general case of fractured ranked surfaces [17] in three dimensions.

7.2. Methods

7.2.1. Sample

The samples were disk-shape specimens with a thickness of 0.5 mm and a diameter of 16 mm cut from two types of nuclear graphite, designated as RID and PGA. The RID graphite was manufactured by Pechiney SA in the 1960's by baking a paste made of oil coke and pitch, graphitized by electrical heating, and was used at the research reactor of the Reactor Institute Delft. The PGA (Pile Grade A) graphite was manufactured by British Acheson Electrodes, Ltd. and Anglo Great Lakes, from needle shaped coke particles derived from the petroleum industry. It was used in the early gas-cooled reactors in UK and has been object of several investigations [5, 8, 18]. PGA was manufactured by extrusion, which leads to aligned coke particles along a direction $\hat{e}$ and thus to the anisotropic properties. For this reason we produced two series of samples: PGA1 cut perpendicular to $\hat{e}$, and thus isotropic; and PGA2 cut along $\hat{e}$ and thus anisotropic. For the sake of simplicity in the following we will focus on PGA1 and the results from PGA2 are averaged over the whole sample as for the other two samples. In this work, the supplement gives a detailed analysis of the results from the PGA2 sample and the anisotropy effect, which is weak but nevertheless visible.

7.2.2. Neutron-matter interaction

Since neutrons are electrically neutral, they can penetrate into matter deeply, only interacting with the nucleii, and are valuable probes of the structure in the bulk. When a

(a) SANS

(b) SESANS

(c) Neutron imaging
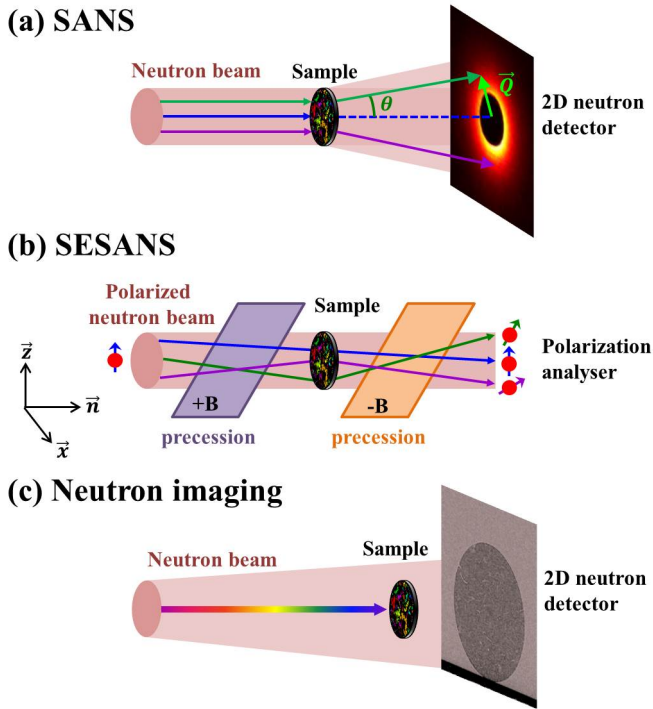
Figure 7.1: (a) Schematic diagram of a SANS experiment. A collimated monochromatic (wavelength λ) neutron beam is scattered by structural inhomogeneities in the sample and recorded by a 2D position-sensitive neutron detector. The magnitude of the scattering vector is $Q = |\vec{Q}| = 4\pi \sin(\theta/2)/\lambda$, with λ the neutron wavelength, and θ the scattering angle. (b) Schematic diagram of a SESANS experiment. A polarized monochromatic neutron beam passes through the setup, where two magnetic fields in opposite direction before and after the sample induce Larmor preccessions. The initial polarization state is completely recovered for the transmitted beam as illustrated by the blue path, whereas scattering changes the final polarization state of the beam. (c) Schematic diagram of a neutron imaging experiment. An incident polychromatic neutron beam is attenuated by the sample and the image recorded by a 2D camera-type neutron detector visualizes the structural inhomogeneities.

beam of thermal neutrons interacts with a sample it may be scattered or absorbed with a respective probability that is given by the scattering lengths and the absorption cross sections of the specific elements and isotopes in the sample (for a comprehensive introduction to neutron scattering see [19]). These transmitted and scattered neutrons deliver structural information from the sample. In the following we will introduce the techniques used in our work.

7.2.3. SMALL ANGLE NEUTRON SCATTERING (SANS)

Fig. 7.1a shows a schematic diagram of a SANS experiment. A neutron beam with a wavelength λ is scattered by the structural inhomogeneities (pores/carbon matrix in the case of graphite) and recorded by a 2D position-sensitive neutron detector. The transmitted beam is captured by a beam-stop made of neutron-absorbing material, illustrated by the

black circular area in the resulting scattering pattern in Fig. 7.1a.

SANS measures the intensity of scattered beam $I(Q)$, i.e. the scattering cross section, as a function of the scattering vector $\vec{Q}$ that is related to the scattering angle θ through $Q = |\vec{Q}| = 4\pi \sin(\theta/2)/\lambda$. $I(Q)$ can be factorized as [19]:

$$I(Q) = \mathcal{B} \cdot P(Q)S(Q). \tag{7.1}$$

Here $\mathcal{B}$ is a pre-factor given by the neutron scattering length density contrast, in our case between the carbon matrix and the pores. $P(Q)$ is the form factor characterizing the morphology/shape of the pores, and $S(Q)$ is the structure factor corresponding to the correlations between pores.

In this work SANS measurements were performed at two instruments, the medium resolution PAXE and the high resolution TPA [20] of the Laboratoire Léon Brillouin (LLB), CEA Saclay, France. On both instruments the neutron beam had a monochromatization of $\Delta\lambda/\lambda = 10\%$. The experiments on TPA were done at λ=0.6 nm, covering the Q range $6 \times 10^{-3} \le Q \le 1 \times 10^{-1}$ nm^{-1}, and on PAXE at λ=0.37, 0.6, and 1.7 nm, respectively, covering the Q range $3 \times 10^{-2} \le Q \le 5$ nm^{-1}. The PAXE data for λ=0.6 nm were brought to absolute units by normalization to the incident beam and were then used to normalise all other data using the large overlap in the Q-ranges illustrated by Fig. 7.2a for the case of PGA1.

7.2.4. SPIN ECHO SMALL ANGLE NEUTRON SCATTERING (SESANS)

The basic principles of SESANS can be found in [21], and Fig. 7.1b represents schematically this technique. In contrast to conventional SANS, SESANS reaches high resolution accessing structural information on micrometres length scales by using a polarized neutron beam. Larmor precessions are induced in two regions with opposite magnetic fields, and if the setup is symmetric, the beam recovers its initial state, leading to a maximum spin echo polarization. Scattering from the sample breaks the symmetry and reduces the echo polarization. SESANS measures the spin echo polarization $P_S(z)$ as a function of the spin echo length z [22], the direction of which is determined by the geometry of the setup and it is always perpendicular to the propagation direction of the neutron beam $\hat{n}$ (see Fig. 7.1b). $P_S(z)$ measures the projected scattering length density correlation function $G'(z)$:

$$P_S(z) = \exp[t\lambda^2(G'(z) - G'(0))/2\pi], \tag{7.2}$$

and $G'(z)$ is the Hankel transformation of the SANS cross section:

$$G'(z) = \int_0^\infty J_0(Qz)I(Q)QdQ, \tag{7.3}$$

where λ is the wavelength of the neutron beam, t is the sample thickness, and J_0 is a zeroth-order Bessel function of the first kind.

The high-resolution neutron Spin Echo SANS experiments were performed on the dedicated instrument of the Reactor Institute Delft [21] at λ=0.205 nm, with $\Delta\lambda/\lambda = 5\%$ and covered length scales from 30 nm to 20 μm.

7.2.5. NEUTRON IMAGING

Fig. 7.1c shows a schematic view of a neutron imaging experiment. The incident poly-chromatic neutron beam passes through a sample. The intensity is attenuated due to absorption and/or scattering and is recorded by a 2D camera-type neutron detector. Since different phases in the sample have different attenuation coefficients, the resulting image visualizes the structural inhomogeneities of the sample.

Neutron imaging was performed on the cold neutron facility, ICON, of the Paul Scherrer Institute, Switzerland [23]. The samples were placed as close as possible to the detector and a resolution of $\sim 30\ \mu$m was obtained. The transmission images were normalized to the empty beam and treated to obtain 8-bit digital images. These were further analysed with the DIPimage Matlab toolbox (http://www.diplib.org/) as described in the supplement.

7.3. RESULTS
7.3.1. SANS
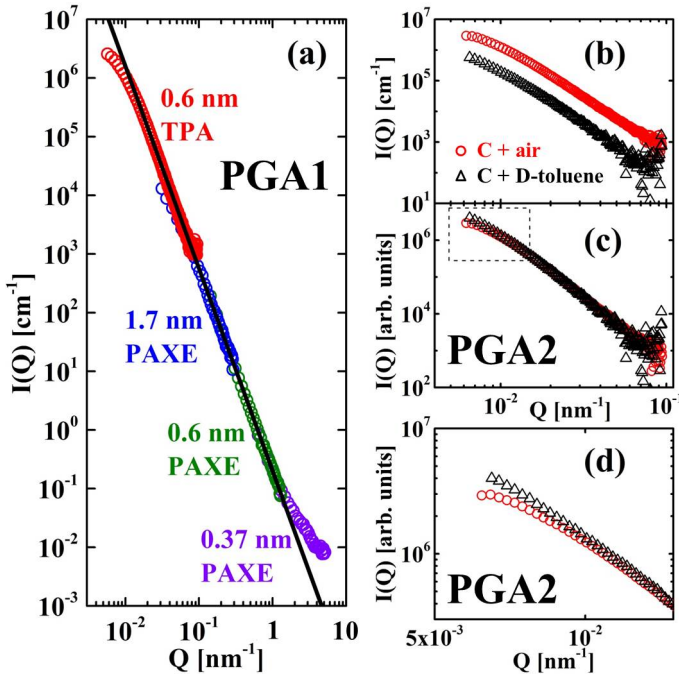
Figure 7.2: (a) Absolute scattering cross section $I(Q)$ of PGA1 for the indicated different instrument and neutron wavelengths. The power law $I(Q) \propto Q^{-\beta}$ with $\beta = 3.45$ is illustrated by the black line. (b)-(d) Contrast variation experiments to investigate the effect of multiple scattering: (b) $I(Q)$ of PGA2 in air (red circles) and of the same sample embedded in deuterated toluene (black triangles). The data are vertically shifted to overlap in (c). A slight difference is found at the very low-Q range, which is enlarged in (d).

The absolute scattering cross section of PGA1, shown in Fig. 7.2a, follows a power law $I(Q) \propto Q^{-\beta}$ with $\beta = 3.45 \pm 0.01$. Similar results have been obtained for the other
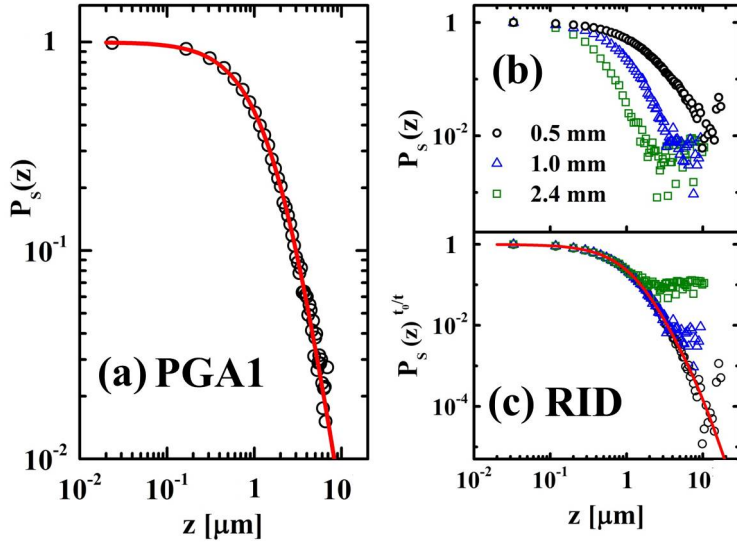
Figure 7.3: Normalized SESANS polarization $P_S(z)$ of (a) PGA1 and (b) RID graphite samples for different sample thicknesses (0.5, 1.0 and 2.4 mm) as a function of the spin echo length z. This effect, which due to the scattering power of the sample and thus to multiple scattering, is taken into account in (c), where $P_S(t)^{t_0/t}$ is plotted versus z, for $t_0 = 1$ mm revealing the same generic curve for all samples. The solid lines in (a) and (b) correspond to the fitting curves from Hankel transform of Eq. 7.1 and 7.6 with the parameters of Table 7.2.

samples and the values of β are given in Table 7.1. Deviations at high-Q's are mainly due to (spin-incoherent) background, whereas at low Q's to multiple scattering. Graphite is a strong neutron scatterer, a property used for nuclear applications, and multiple scattering is not negligible even for the thin samples used in this study, as illustrated by the transmission values given in the supplement. For this reason SANS was also measured by embedding one sample (PGA2) in deuterated toluene, which reduces the scattering contrast. As a consequence the transmission increased and the scattered neutron intensity decreased by almost an order of magnitude as shown in Fig. 7.2b. However, the shape stays unchanged with the exception of the very low-Q range illustrated by Fig. 7.2c, where the two curves are shifted on the log-log scale. In the enlarged view of Fig. 7.2d, it is clear that the bending characteristic for multiple scattering [24] is less pronounced for the sample in deuterated toluene. Thus multiple scattering has an influence on the SANS patterns but does not affect the power law, which is the same for both cases and reflects the genuine structural properties of the sample. Similar behaviour has been found in expanded graphite [25] and sedimentary rocks samples [26].

7.3.2. SESANS

Fig. 7.3a shows the SESANS pattern of PGA1. As already mentioned, SESANS measures the Hankel transformation of $I(Q)$ in the form of normalised (to the direct beam) SESANS polarization P_S, which is a function of the spin echo length z [22]. It probes length ranges from ~ 30 nm to $\sim 20 \, \mu$m, and thus "sees" very large objects, which scatter a large fraction
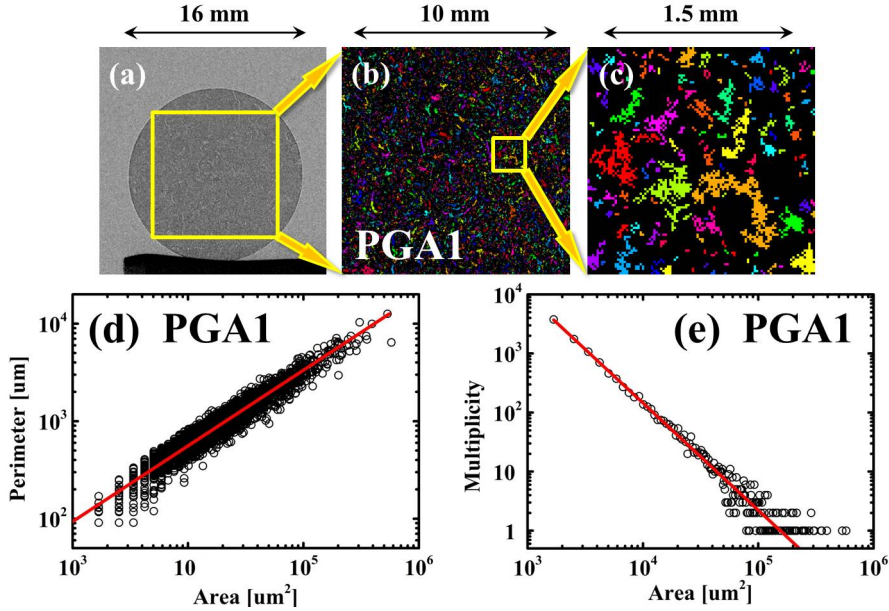
Figure 7.4: : Neutron transmission image of the PGA1 sample (a), within the selected yellow square, the pores are labelled with different colours (b), and a selected region is enlarged in (c). The analysis of the shapes of the pores leads to the Perimeter-Area plot of (d). The red line corresponds to a power law $P \propto A^{\gamma}$ with $\gamma = 0.77$. The pore size distribution is given in (e), which shows a power law $M(A) \propto A^{\tau}$ with $\tau = -1.82$ illustrated by the red line.

of the incoming beam. This is also the case in Fig. 7.3a, where even for the 0.5 mm PGA1 sample at large spin echo lengths z, the entire beam is scattered and $P_S(z > 10\,\mu m) \to 0$. However, even in this extreme case multiple scattering does not alter the results. This effect can indeed be accounted in a way similar to the Beer-Lambert's law in optics and if $P_S(t_0)$ is the SESANS signal for a reference sample thickness t_0, the SESANS signal for any other thickness t is given by: $P_S(t)^{t_0/t} = P_S(t_0)$ [27]. This property was tested on three RID samples with thicknesses of 0.5, 1 and 2.4 mm respectively. As shown in Fig. 7.3b, $P_S(z)$ decreases much faster for the thicker samples. However, when plotting $P_S(t)^{t_0/t}$, with t_0=1 mm, all data follow on the same generic curve shown in Fig. 7.3c, with deviations when P_S is smaller than the experimental error of 10^{-2}. More importantly, these results show that the porous structure extends up to macroscopic length scales, which can be investigated by direct imaging.

7.3.3. Neutron imaging

Fig. 7.4a shows the neutron transmission image of the PGA1 sample (the images for the other samples are in the supplement). The treatment of this image (see supplement) leads to a binary image, where the pores are distinguishable from the carbon matrix. Consequently the pores within the selected yellow square (of size 800×800 pixel) are labelled with different colours according to their sizes and shapes. This leads to Fig. 7.4b,
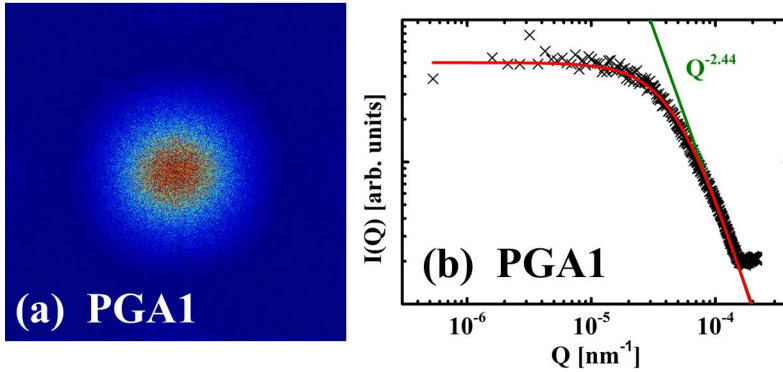
Figure 7.5: :The 2D scattering pattern of PGA1 obtained by 2D-Fourier transform on the selected region illustrated by the yellow square in Fig.7.4a. This leads to the $I(Q)$ curve of (b). The power law at $Q \geq 1.5 \times 10^{-4}$ nm^{-1}, $I(Q) \propto Q^{-2.44}$ illustrated by the green line, has an exponent smaller than 3 indicating a mass fractal. The red line in (b) corresponds to Eq. 7.1 and 7.6 with parameters of Table 7.2.

and a selected region enlarged in (c) reveals a strongly ramified, fractal structure. This structure may be brought in relation with the reported micropores [4–6, 8], that result from calcination and gas evolution during the manufacturing process and have sizes from several micrometres to hundreds of micrometres without preferred orientations. The binary images also lead to an estimation of the porosity ϕ_{image} , which is about 82-85% of the porosity ϕ_D determined from density measurements, considering 2.25 g/cm^3 as the density of single crystalline graphite. Thus pores smaller than the 30 μm (resolution limit of the images) contribute only by 15-18% to the total porosity.

The plot of the pore perimeter P against area A for PGA1 (the plots for other samples are given in the supplement), shown in Fig. 7.4d, reveals a power law $P \propto A^\gamma$ with $\gamma = 0.77 \pm 0.01$ (red line in the figure). This value is higher than 0.5, the value expected for Euclidian geometry, and is thus a signature of fractality. We note that in this figure the points have different multiplicities. The pore size multiplicity $M(A)$ is plotted against A in Fig. 7.4e, where $M(A) \propto A^\tau$ with $\tau = -1.82 \pm 0.03$, illustrated by the red line in the figure, and the values of τ for other samples are listed in Table 7.1. Thus the total volume of pores $V(A)$ with specific area size A is given by: $V(A) \propto M(A) \times A^{3/2} \propto A^\tau \times A^{3/2} = A^{\tau+3/2} \sim A^{-0.3}$. The low value of the exponent indicates that the pores with different sizes have almost the same total volume.

A quantitative analysis of the transmission images involves a 2D-Fourier transform of the region inside the yellow square of Fig. 7.4a, which leads to the 2D scattering pattern of Fig. 7.5a. By radially averaging this intensity, following the same procedure as for the SANS data, the scattering curve of Fig. 7.5b is obtained, with Q calculated as given in the supplement. The resulting $I(Q)$ levels off at low-Q region and crosses over to a power law $I(Q) \propto Q^{-2.44\pm0.09}$ at higher Q's.

7.4. Discussion

These results disclose power laws, which are characteristics of fractal topology: fractal surfaces (of pores or particles) with a surface fractal dimension D_s or mass fractals with a mass fractal dimension D_m [28, 29]. The most direct signature of fractality is the power law of the SANS intensity shown in Fig. 7.2. It is indeed expected that [30, 31]:

$$\text{for a surface fractal:} \quad I(Q) \propto Q^{-(6-D_s)}, \tag{7.4}$$

$$\text{for a mass fractal:} \quad I(Q) \propto Q^{-D_m}, \tag{7.5}$$

where the values of both D_m and D_s are smaller than 3, the dimensionality of the Euclidian space. Expressing the power laws as $I(Q) \propto Q^{-\beta}$, $\beta > 3$ corresponds to a surface fractal and $\beta < 3$ to a mass fractal. All graphites showed $\beta > 3$ leading to the surface fractal dimensions listed in Table 7.1.

Additional confirmation of these results comes from the Perimeter-Area power law

Table 7.1: Power law exponents (β, τ), fractal dimensions (D_s, D_m) and porosity (ϕ_D and ϕ_{image}) derived from SANS and imaging.

Sample	SANS		Imaging			Porosity	
	β	D_s	Ds	D_m	τ	ϕ_D	ϕ_{image}
PGA1	3.45 (1)	2.55 (1)	2.54 (2)	2.44 (9)	-1.82 (3)	22.7(5)%	18.6%
PGA2	3.43 (1)	2.57 (1)	2.50 (2)	2.54 (9)	-1.80 (4)	22.7(5)%	17.8%
RID	3.45 (1)	2.55 (1)	2.56 (2)	2.45 (9)	-1.74 (3)	27.1(5)%	23.0%

$P \propto A^\gamma$ of Fig. 7.4d, where the exponent γ is directly related to the surface fractal dimension D_s through $\gamma = (D_s - 1)/2$ [32–34], leading to $D_s = 2.54 \pm 0.02$ for PGA1. Similar results were obtained for the samples and all deduced values of D_s are listed in Table 7.1 and are consistent with those obtained from SANS. Therefore imaging and SANS "see" the same surface self-similar fractal structure although they probe length scales more than 3 orders of magnitude apart.

On the other hand, the power law of $I(Q)$ derived from the Fourier transformed images leads to an exponent significantly smaller than 3 (Fig. 7.5b), which is in line with a mass fractal and not surprising at this very low Q-limit. The deduced values of D_m are given in Table 7.1, and for all samples $D_m \approx D_s$.

The experimental results indicate that the pores of the graphite samples have a fractal (i.e. rough) surface while their assembly forms a mass fractal. To be specific, one can consider that the pore structure consists of many pore-building blocks, which characterize the network of the pore clusters with a mass fractal property at the length scale above the size of the primary block. Moreover, the pore building block itself is bounded by a rough surface with fractal morphology. In this case the scattering function reflects

Table 7.2: Parameters for the fractal model assuming $D_s = D_m$.

Sample	SANS $D_s = D_m$ (fixed)	Imaging ξ (μm) (fitted)	SESANS ℓ (μm) (fitted)	$\mathscr{B}$ (cm^{-1}) (fitted)	$S(Q=0)$ (calculated)	Global $\mathscr{B}$ (cm^{-1}) (fitted)	$\mathscr{B}$ (cm^{-1}) (calculated)
PGA1	2.55	18.9 (4)	2.27 (10)	$6.6(1) \times 10^{10}$	134(15)	$7.56(5) \times 10^{10}$	$6.3(9) \times 10^{10}$
PGA2	2.57	17.0 (5)	2.64 (25)	$8.4(1) \times 10^{10}$	74(5)	$1.87(1) \times 10^{11}$	$9.8(5) \times 10^{10}$
RID	2.55	18.7 (4)	1.87 (6)	$3.0(1) \times 10^{10}$	214(17)	$4.64(4) \times 10^{10}$	$4.2(5) \times 10^{10}$

both mass and surface fractal properties and Eq. 7.1 can be factorized as [31, 35]:

$$\mathscr{B} = \phi_D \Delta\rho^2 V_p = \phi_D \Delta\rho^2 4\pi \ell^3/3 \tag{7.6a}$$

$$P(Q) = (1 + Q^2\ell^2)^{(D_s-6)/2} \tag{7.6b}$$

$$S(Q) = 1 + \frac{D_m \Gamma(D_m-1)}{(2Q\ell)^{D_m}}(1 + \frac{1}{(Q\xi)^2})^{(1-D_m)/2}. \tag{7.6c}$$
$$\cdot \sin[(D_m-1)\arctan(Q\xi)],$$

where $\Delta\rho$ (=7.5·10^{10} cm^{-2} for carbon-air) is the scattering length density contrast, V_p the volume of a primary pore building block, ℓ the associated length, $P(Q)$ the form factor, characteristic of the surface fractal morphology of the pores, $S(Q)$ the structure factor corresponding to the mass fractal structure and Γ the gamma function. Besides the fractal dimensions D_m and D_s, two characteristic lengths are introduced: an upper cut-off length ξ and the length of the primary pore-building block ℓ, which marks the cross-over between mass and surface fractal scattering.

In order to fit all experimental results with this model in the most reliable way we adopted the following strategy : (1) the values of D_s were fixed to those of Table 7.1, derived from SANS; (2) the values of D_m and ξ were derived from the scattering patterns of the Fourier transformed images. These are given in Table 7.1, which shows that $D_m \approx D_s$. For the sake of simplicity we assumed $D_m = D_s$ in the following. (3) With D_m, D_s and ξ fixed, ℓ was determined by fitting the SESANS data, that fill the gap between SANS and imaging and probe the cross-over between mass and surface fractal scattering. For this purpose the Hankel transform was performed numerically on Eq. 7.1 (combined with Eq. 7.6) through Eq. 7.3; then the data were fitted using Eq. 7.2 with only two floating parameters: length ℓ and the prefactor $\mathscr{B}$, and the resulting values are given in Table 7.2. The fits are illustrated by the solid lines in Fig. 7.3 and describe excellently the experimental findings.

 The final step is to combine SANS, SESANS and imaging, which is done in Fig. 7.6. In this figure the lines correspond to the best fit of Eq. 7.6 with the parameters of Table 7.2. The Q values for which $Q\xi = 1$ and $Q\ell = 1$ are also indicated. We stress that the model provides excellent quantitative description of the experimental findings. Indeed the prefactors $\mathscr{B}$ given in Table 7.2, which are deduced from fitting all data (global) are in excellent agreement with the calculated values from the fitted values of ℓ through Eq. 7.6a. Therefore, a consistent picture of the fractal microstructure of graphite is obtained over an extraordinary large range of length scales of 6 orders of magnitude (~0.6 nm $\leq 2\pi/Q \leq 0.6$ mm). Table 7.2 shows that the fractal dimensions and cut-off lengths ξ are almost the same for all samples, which might be because both PGA and RID are made
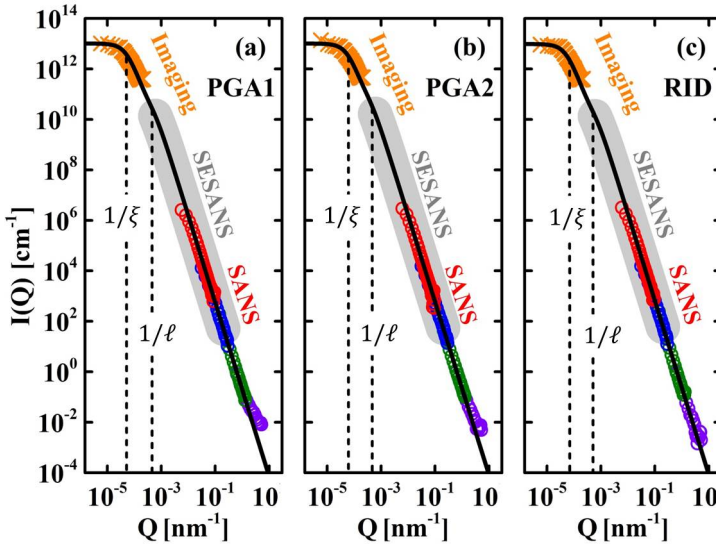
Figure 7.6: Scattering curves for (a) PGA1 (b) PGA2 and (c) RID over for the whole Q range investigated. The circles represent the SANS data; the orange crosses are from the Fourier transformation of the neutron images; and the gray shaded zone represent the Q-range covered by SESANS. The black lines correspond to the best fit of the Eq. 7.6 with the parameters of Table 7.2. The dotted lines correspond to $Q = 1/\xi$ and $1/\ell$ respectively.

out of petroleum coke [12]. A trend is only seen in the values of ℓ, which is the parameter that reflects the particularities of the microstructure and also the anisotropy of PGA2 (see supplement). It has been shown that the fractal anisotropy can be found in graphite at low densities (expanded graphite) and that in fact under densification such anisotropy is lost [25, 36].

In the literature besides the micropores mentioned above, so-called Mrozowski cracks have been reported [4, 5, 7], that result from the anisotropic thermal shrinkage of the layered graphite structure during cooling from graphitization temperatures. These have lengths from nm to μm that are in the range probed by SESANS and SANS. It is therefore tempting to attribute the surface fractal scattering to these cracks, as suggested recently [14], and ℓ to the cross-over between cracks and micropores.

In contrast to optical or electron microscopy, the scattering techniques used in this work cannot distinguish between cracks and pores. However, they provide a statistical average of the correlations over the (macroscopic) samples and reveal the most generic features of the structure. In this way it is possible to describe the complex and poly-disperse patterns of Fig. 7.4 with the scattering law of Eq. 7.6 involving a restricted number of parameters, which enables quantitative comparisons between different samples and systems. Besides the extraordinary large length scales over which fractality has been observed, the fractal dimensions found in this work are comparable to those expected for percolating clusters [15, 37], for which heuristic arguments suggest that mass fractals should be bounded by their own natural fractal surface and $D_m = D_s$ [15]. The porosity values of Table 7.1 indicate indeed a topology close to that of a percolating cluster [37].

Similar fractal exponents have been deduced for fracturing ranked surfaces in 3D [17], that could serve as a model for Mrozowski cracks. Therefore the identity $D_m = D_s \sim 2.5$ is not coincidence but the consequence of the high degree of disorder, ramification and connectivity of the pore structure. Under neutron irradiation surface fractality disappears [14], and similar behaviour may be expected for the oxidised samples. The methodology developed in this work thus can be applied to further investigate the effect of irradiation damage and/or oxidation on the structural properties of graphite.

Fractal scattering has also been reported for carbon nanopores [38, 39], rocks [26] or cement [40]. The particularity of this work is in the extraordinarily broad length scale of six orders of magnitude over which fractal scaling is quantitatively valid. The combination of several techniques, from imaging to scattering and the methods can be applied to the investigation of other complex systems with a hierarchy of length scales such as biological materials, concrete and rocks, materials for CO2 sequestration, Li batteries, fuel cells or solar cells.

7.5. ACKNOWLEDGMENTS

7.6. SUPPLEMENT

TRANSMISSIONS OF THE SANS AND SESANS MEASUREMENTS

The transmissions for the SANS and SESANS experiments are listed in Table 7.3. The values vary between different instruments, neutron wavelengths and collimations. On PAXE and TPA, neutron counts were accumulated, with and without the samples, inside the small area of the neutron detector that corresponded to the direct beam, which was attenuated to avoid saturation of the counting electronics. In SESANS the direct beam with and without samples was measured as part of the standard measuring procedure.

Table 7.3: Transmission values determined in SANS and SESANS

Sample (thickness [mm])	PAXE(SANS)			TPA(SANS)	SESANS
	λ=0.37 nm	λ=0.6 nm	λ=1.7 nm	λ=0.6 nm	λ=0.205 nm
PGA1 (0.5)	99.5%	96.9%	48.0%	33.6%	97.6%
PGA2 (0.5)	97.6%	96.5%	52.2%	42.8%	97.4%
PGA2 (0.5)+D-toluene	-	-	-	52.1%	-
RID (0.5)	99.4%	97.5%	45.4%	36.4%	97.5%
RID (1.0)	-	-	-	-	94.7%
RID (2.4)	-	-	-	-	86.5%

SANS RESULTS OF PGA2 AND RID

The SANS patterns of PGA2 and RID are given in Fig. 7.7.
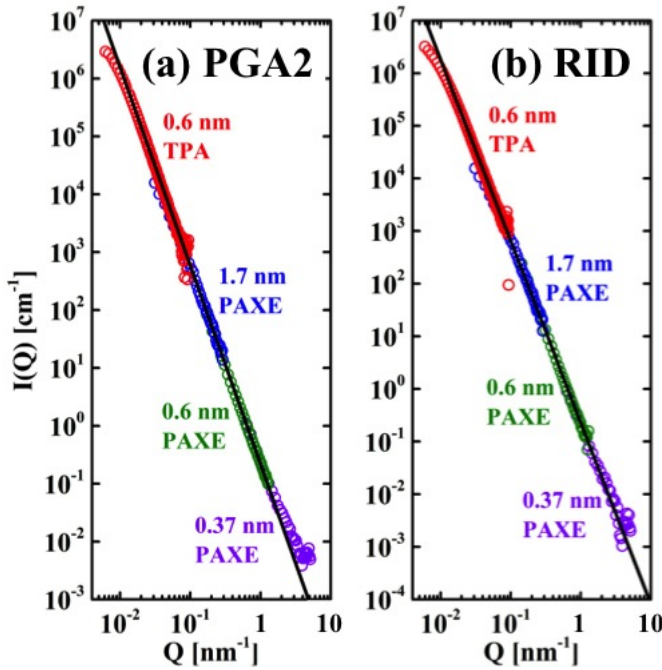
Figure 7.7: Absolute scattering cross sections $I(Q)$ of (a) PGA2 and (b) RID graphites measured on the SANS instruments PAXE and TPA for the indicated different neutron wavelengths. The results follow a power law $I(Q) \propto Q^{-\beta}$ with $\beta = 3.43 \pm 0.01$ and $\beta = 3.45 \pm 0.01$ for PGA2 and RID samples, respectively, illustrated by the black lines.

ANALYSIS OF THE NEUTRON IMAGES

Fig. 7.8 displays the histograms of the 8-bit in grey scale digital neutron images of all samples. The high counts with grey-scale at 0 (i.e. black) are due to the sample holder at the bottom of the image. The spectra show two peaks, which are due to the carbon matrix and the background-pores, respectively. These are fitted by two Gaussian functions and the threshold values, determined from the intersection points, are used to produce the binary images. We note that a slightly different choice of the threshold does not change the results. The movie illustrates the dependence on the binary images on the choice of the threshold. After having introduced this threshold the pores have been labelled and measured, leading to the images of Fig. 4 and 7.9. The plots of the pore perimeter P against area A for PGA2 and RID are shown in Fig. 7.10a and c, reveal a power law $P \propto A^{\gamma}$, and the exponent γ is directly related to the surface fractal dimension D_s as given in Table 1 in the manuscript. We note that in these figures the points have different multiplicities, and the pore size multiplicity $M(A)$ is plotted against A in Fig. 7.10b and d; $M(A) \propto A^{\tau}$ with τ given in Table 1 in the manuscript.
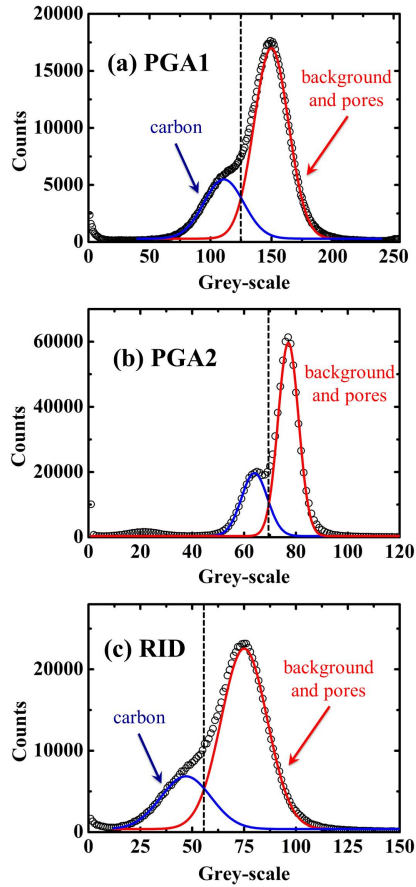
Figure 7.8: Histograms of the neutron images of (a) PGA1, (b) PGA2 and (c) RID samples. The blue and red lines illustrate the peaks corresponding to the carbon matrix and the background-pores, respectively. The vertical black dashed lines indicate the threshold values chosen for the subsequent data analysis.
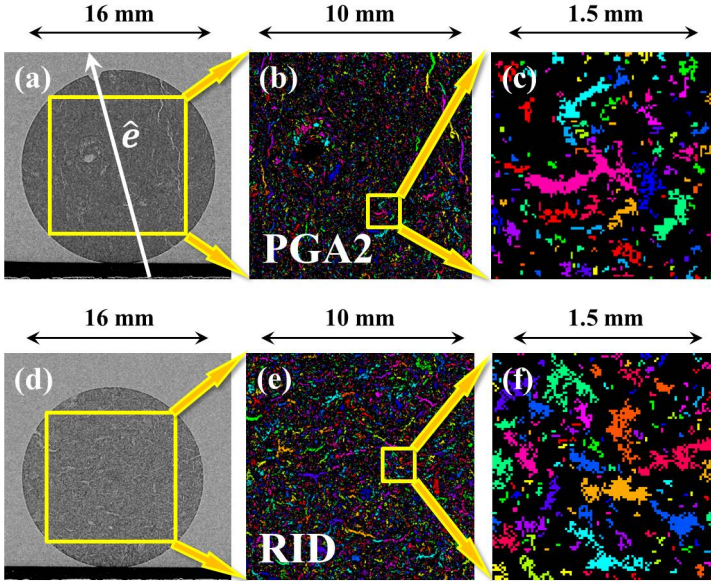
Figure 7.9: Neutron images from the (a) PGA2 and (d) RID samples. By introducing a threshold a binary image is obtained with the selected yellow squares shown in (b) and (e), where the pores are labelled by different colors and the selected regions are enlarged in (c) and (f) respectively. The vector $\hat{e}$ indicates the extrusion direction.
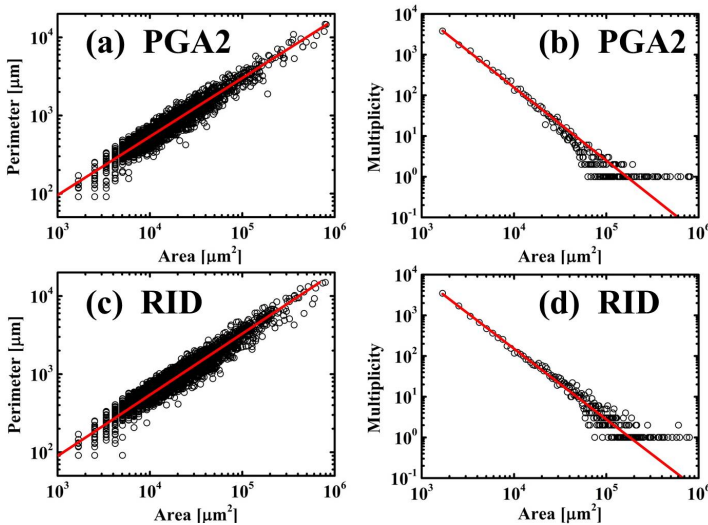
Figure 7.10: Perimeter-Area relationships for (a) PGA2 and (c) RID samples revealing power laws: $P \propto A^{\gamma}$ with $\gamma = 0.75 \pm 0.01$ and 0.78 ± 0.01 respectively (red lines); (b) and (d) are corresponding to the pore size distributions, which follow the power law $M(A) \propto A^{\tau}$ with $\tau = -1.80 \pm 0.04$ and -1.74 ± 0.03 respectively (red lines).
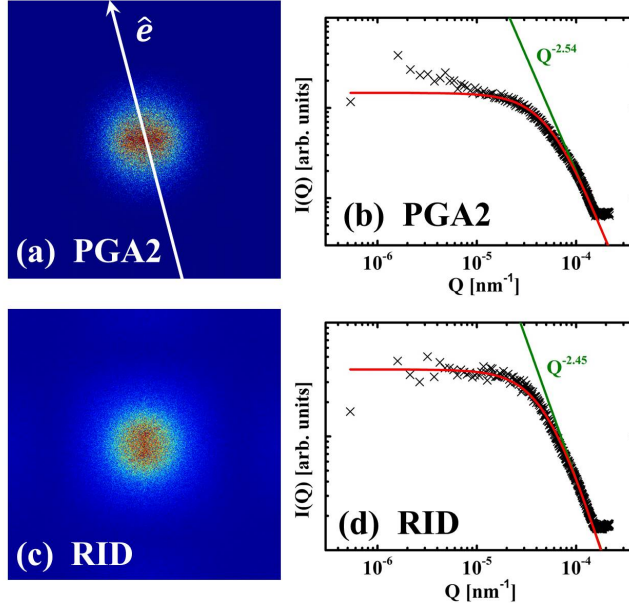
Figure 7.11: 2D scattering patterns of (a) PGA2 and (c) RID obtained by 2D-Fourier transforming the regions in the yellow squares of Fig. 7.9a and d. The resulting $I(Q)$ curves are given in (b) and (d), respectively. The power laws illustrated by the green lines lead to the D_m values of Table 1. The red lines correspond to Eq. 4 with the parameters of Table. 2. The vector $\hat{e}$ indicates the extrusion direction.

The Fourier transformation of the images leads to $I(Q)$ patterns in units of reciprocal pixels j. Each pixel has a width of $l_{pixel} = 2.9 \times 10^4$ nm and the total number of pixels from the center of the yellow square in Fig. 3a and Fig, 7.9a and d is $N/2$, with $N = 800$. Thus the maximum momentum transfer is $Q_{max} = 2\pi/l_{pixel}$ and the value of Q corresponding to a distance of j pixels from the center of the yellow square is:

$$Q(j) = \frac{2\pi j}{l_{pixel}(N/2)} \tag{7.7}$$

Fig. 7.11 gives the results from the Fourier transformed images of the PGA2 and RID samples.

ANISOTROPIC STRUCTURE OF PGA2

PGA is produced by extrusion along a direction $\hat{e}$ and is thus anisotropic. As mentioned at the manuscript two samples were obtained labelled PGA1 (isotropic) and PGA2 (anisotropic) by cutting the raw bulk material perpendicular to or along $\hat{e}$ as illustrated by Fig. 7.12. SANS, SESANS and imaging confirmed the isotropic structure of PGA1, while revealed a slight anisotropy for PGA2. The results of PGA1 were given in the main text and here we will discuss in detail the results of PGA2.
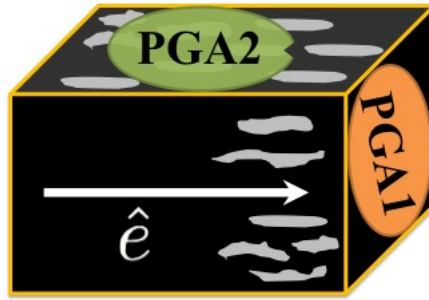
Figure 7.12: Schematic diagram for the way PGA graphite was cut indicating the orientations of PGA1 and PGA2 samples respectively. The vector $\hat{e}$ indicates the extrusion direction.

The SANS patterns of PGA2 show a slight anisotropy of the scattered intensity as illustrated by Fig. 7.13, with the amplitude of the scattering being slightly higher perpendicular to $\hat{e}$ than along $\hat{e}$. The deduced I(Q) curves have the same shape but different intensities, with $I_\perp(Q) \sim 1.6 I_\parallel(Q)$, where $I_\perp(Q)$ corresponds to the intensity perpendicular to $\hat{e}$ and $I_\parallel(Q)$ to the intensity along $\hat{e}$ respectively.
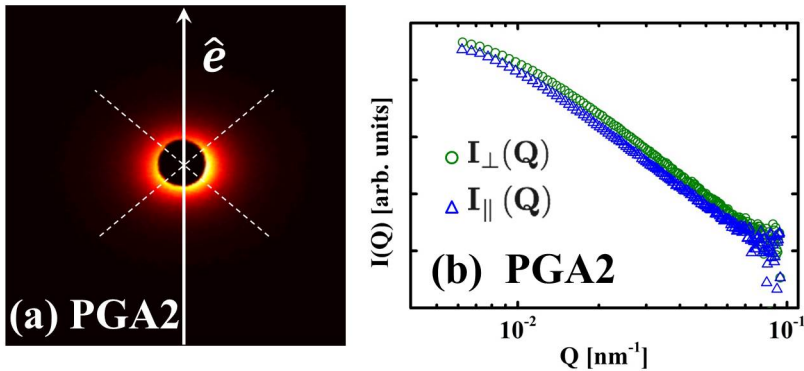
Figure 7.13: (a) Scattering pattern of PGA2 measured on the SANS instrument TPA, where the white arrow indicating the extrusion direction $\hat{e}$. (b) Scattering curves perpendicular to (green) or along (blue) $\hat{e}$ were obtained separately by averaging radially the intensities at different regions, which are illustrated by the dash white lines.

The 2D Fourier transformation of the neutron image of PGA2, displayed in Fig. 7.11 a, also shows a slight anisotropy. The corresponding $I_\perp(Q)$ and $I_\parallel(Q)$ curves can be obtained similarly to the SANS treatment of Fig. 7.13, and the results are given in Fig. 7.14 leading to $I_\perp(Q) \sim 1.2 I_\parallel(Q)$.
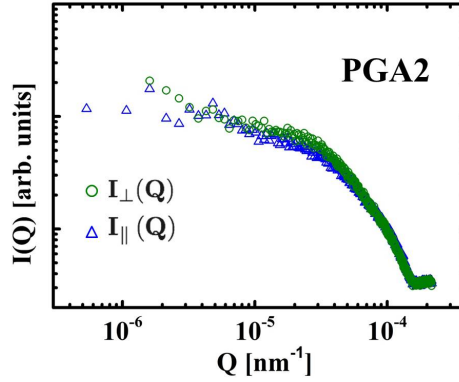
Figure 7.14: $I(Q)$ curves obtained by averaging the intensity of the anisotropic Fourier transform image of PGA2 (shown in Fig 7.11a) along different directions. The green circles correspond to $I_\perp(Q)$ and the blue triangles to $I_\parallel(Q)$.

As mentioned above SESANS probes the structure in the specific spin echo length direction $\hat{z}$, which is determined by the geometry of the setup and $\hat{z} \perp \hat{n}$, with $\hat{n}$ the propagation direction of the neutron beam. In the case of the isotropic sample PGA1, $\hat{n} \parallel \hat{e}$ and thus $\hat{z} \perp \hat{e}$. In this case, just like in SANS and imaging the orientation of the (disk-shaped) sample was not important. In the case of the anisotropic sample PGA2, $\hat{n} \perp \hat{e}$ and two extreme cases are possible: $\hat{z} \perp \hat{e}$ and $\hat{z} \parallel \hat{e}$ depending on the specific orientation of the sample. The results are shown in Fig. 7.15 a and b, and the two fits lead to an average SESANS curve, which has also been fitted by the fractal model, shown in c. The deduced fitting parameters are listed in Table 7.4. (in the text we only used the averaged PGA2 values). As seen in Table 7.4 the anisotropy of the structure leads to different values of ℓ, which are ~30% larger for $\hat{z} \parallel \hat{e}$ than for $\hat{z} \perp \hat{e}$, both for PGA2 and PGA1. This ratio is consistent with the difference in the $I_\perp(Q)$ and $I_\parallel(Q)$ following Eq. 4.

Table 7.4: The parameters of PGA samples deduced from the analysis of the SESANS data.

Sample	$D_s = D_m$ (fixed)	ξ (μm) (fixed)	ℓ (μm) (fitted)	$\mathscr{B}$ (cm^{-1}) (fitted)
PGA1 ($\hat{z} \perp \hat{e}$)	2.55	18.9	2.27 (10)	$6.6(1) \times 10^{10}$
PGA2 ($\hat{z} \parallel \hat{e}$)	2.57	17.0	3.07 (11)	$1.2(1) \times 10^{11}$
PGA2 ($\hat{z} \perp \hat{e}$)	2.57	17.0	2.42 (24)	$7.3(1) \times 10^{10}$
PGA2 (avg.)	2.57	17.0	2.64 (25)	$8.4(1) \times 10^{10}$
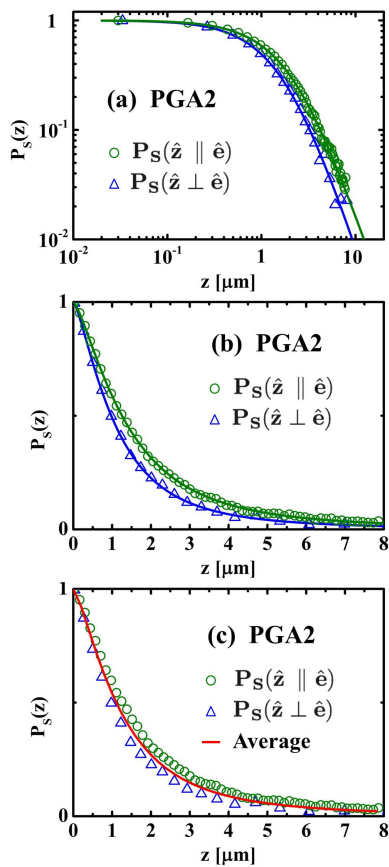
Figure 7.15: Spin Echo SANS polarizations $P_S(z)$ of PGA2 for $\hat{z} \parallel \hat{e}$ and for $\hat{z} \perp \hat{e}$ in a (a) log-log and (b) linear-linear scale. The solid lines correspond to the fitting curves from Hankel transform of Eq. 4 with the parameters given in Table 7.4. The two fits lead to the average curve, which has been also fitted by Eq. 4 shown by the red line in (c), and the fitted parameters are given in Table 7.4.

7.7. Appendix: unpublished data

In this work, in addition to the RID and PGA graphites, PCEA and 1940 PT graphites have also been investigated by SANS and SESANS. The SANS patterns of PCEA and 1940 PT samples are given in Fig. 7.16. For each graphite, the samples were cut along different directions as the case of PGA graphite. The measured scattering cross section curves of different samples (red and blue data points) overlap indicating the isotropy of the structure. The scattering behaviour of both graphites follows a power law $I(Q) \propto Q^{-\beta}$ with $\beta = 3.55 \pm 0.01$ and $\beta = 3.44 \pm 0.01$ for PCEA and 1940 PT samples, respectively. Therefore the surface fractal dimensions D_s can be obtained and the values are listed in Table. 7.5.
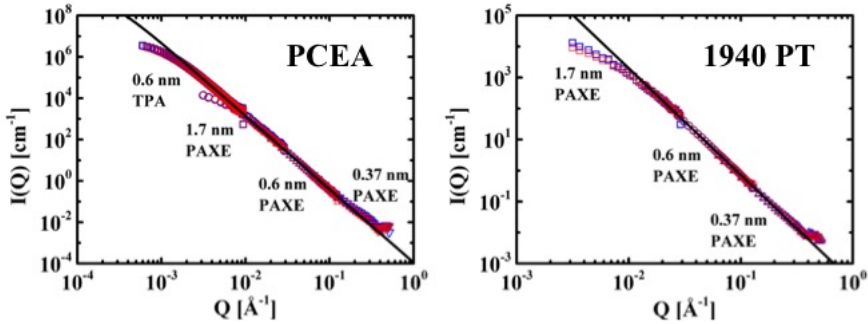

Figure 7.16: Absolute scattering cross section $I(Q)$ of PCEA and 1940 PT graphites measured on the SANS instruments TPA and PAXE for the indicated different neutron wavelengths. The results follow a power law $I(Q) \propto Q^{-\beta}$ with $\beta = 3.55 \pm 0.01$ and $\beta = 3.44 \pm 0.01$ for PCEA and 1940 samples, respectively. The black lines correspond to the best fit of the Eq. 7.6 with the parameters in Table. 7.5.

To interpret the SESANS data of PCEA and 1940 PT graphites shown in Fig. 7.17, the same fractal model and analysis strategy discussed in this chapter has been used. (1) The values of D_s can be derived from SANS; (2) $D_m = D_s$ was assumed; (3) with D_m and D_s fixed, ℓ and ξ were determined by fitting the SESANS data. The fits are illustrated by the solid lines in Fig. 7.17 and the parameters are listed in Table. 7.5. We note that the SESANS data for the PCEA graphite saturates at large spin echo length z, indicating the scattering intensity level off in the probing range, leading to the determination of the value of ξ. In contrary, the value of ξ for the 1940 graphite cannot be estimated because the scattering intensity saturates outside of the SESANS range, and this behaviour is similar with the case of RID and PGA graphites.

Table 7.5: Parameters for the fractal model assuming $D_s = D_m$.

| Sample	SANS $D_s = D_m$ (fixed)	ξ (μm) (fitted)	SESANS ℓ (μm) (fitted)	$\mathcal{B}$ (cm^{-1}) (fitted)	Global $\mathcal{B}$ (cm^{-1}) (fitted)	$\mathcal{B}$ (cm^{-1}) (calculated)
PCEA	2.45	6.9 (5)	0.41 (4)	$3.8(1) \times 10^8$	$7.9(5) \times 10^8$	$3.5(5) \times 10^8$
1940 PT	2.56	4.7 (100)	4.0 (10)	$3.1(1) \times 10^{11}$	$1.7(5) \times 10^{12}$	$3.1(5) \times 10^{11}$
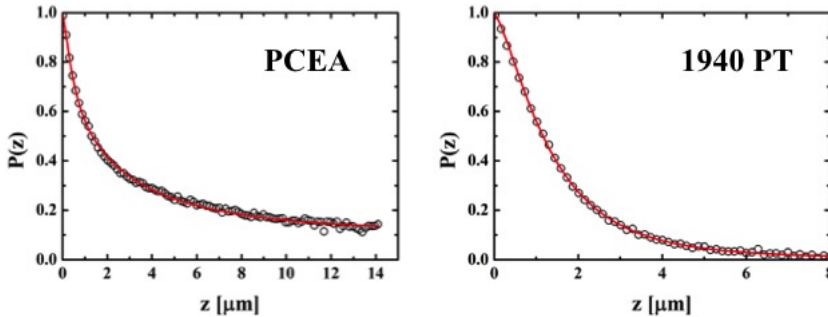
Figure 7.17: Normalized SESANS polarization of PCEA and 1940 PT graphite samples as a function of the spin echo length z. The red lines correspond to the fit curves from Hankel transform of Eq. 7.1 and the Eq. 7.6 with the parameters in Table. 7.5

REFERENCES

[1] Z. Zhou, W. G. Bouwman, H. Schut, S. Desert, J. Jestin, S. Hartmann, and C. Pappas, *From nanopores to macropores: Fractal morphology of graphite,* Carbon **96**, 541 (2016).

[2] G. Haag, Tech. Rep. Jülich-4183 (2005).

[3] Z. Zhou, W. G. Bouwman, H. Schut, and C. Pappas, *Interpretation of x-ray diffraction patterns of (nuclear) graphite,* Carbon **69**, 17 (2014).

[4] K. Y. Wen, T. J. Marrow, and B. J. Marsden, *The microstructure of nuclear graphite binders,* Carbon **46**, 62 (2008).

[5] A. N. Jones, G. N. Hall, M. Joyce, A. Hodgkins, K. Wen, T. J. Marrow, and B. J. Marsden, *Microstructural characterisation of nuclear grade graphite,* J. Nucl. Mater. **381**, 152 (2008).

[6] J. Kane, C. Karthik, D. P. Butt, W. E. Windes, and R. Ubic, *Microstructural characterization and pore structure analysis of nuclear graphite,* J. Nucl. Mater. **415**, 189 (2011).

[7] C. Karthik, J. Kane, D. P. Butt, W. E. Windes, and R. Ubic, *Microstructural characterization of next generation nuclear graphites,* Microsc. Microanal. **18**, 272 (2012).

[8] P. J. Hacker, G. B. Neighbour, and B. McEnaney, *The coefficient of thermal expansion of nuclear graphite with increasing thermal oxidation,* J. Phys. D: Appl. Phys **33**, 991 (2000).

[9] E. Hoinkis, *Small angle scattering of neutrons and x-rays from carbons and graphites,* in *Chemistry & Physics of Carbon,* Vol. 25, edited by P. A. Thrower (CRC Press, 1996) p. 71.

[10] D. G. Martin and R. W. Henson, *Scattering of long wavelength neutrons by defects in neutron-irradiated graphite,* Phil. Mag. **9**, 659 (1964).

[11] D. G. Martin and J. Caisley, *Some studies of effect of irradiation on neutron small-angle scattering from graphite,* Carbon **15**, 251 (1977).

[12] D. G. Martin and J. Caisley, *Inference of coke source of nuclear graphites from neutron small-angle scattering measurements,* J. Nucl. Mater. **67**, 318 (1977).

[13] D. G. Martin and J. Caisley, *Some studies of effect of thermal and radiolytic oxidation on neutron small-angle scattering from nuclear graphites,* Carbon **16**, 199 (1978).

[14] Z. Mileeva, D. K. Ross, and S. M. King, *A study of the porosity of nuclear graphite using small-angle neutron scattering,* Carbon **64**, 20 (2013).

[15] R. M. Bradley, P. N. Strenski, and J. M. Debierre, *Surfaces of percolation clusters in three dimensions,* Phys. Rev. B **44**, 76 (1991).

[16] H. Saleur and B. Duplantier, *Exact determination of the percolation hull exponent in two dimensions,* Phys. Rev. Lett. **58**, 2325 (1987).

[17] K. J. Schrenk, N. A. M. Araujo, J. S. Andrade, and H. J. Herrmann, *Fracturing ranked surfaces,* Scientific Reports **2** (2012).

[18] B. Marsden and A. J. Wickham, *Characterization, treatment and conditioning of radioactive graphite from decommissioning of nuclear reactors,* (2006).

[19] B. T. M. Willis and C. J. Carlile, *Experimental neutron scattering* (Oxford Univ. Press, 2009).

[20] S. Desert, V. Thevenot, J. Oberdisse, and A. Brulet, *The new very-small-angle neutron scattering spectrometer at laboratoire leon brillouin,* J. Appl. Crystallogr. **40**, S471 (2007).

[21] M. T. Rekveldt, J. Plomp, W. G. Bouwman, W. H. Kraan, S. Grigoriev, and M. Blaauw, *Spin-echo small angle neutron scattering in delft,* Rev. Sci. Instrum. **76** (2005).

[22] R. Andersson, L. F. van Heijkamp, I. M. de Schepper, and W. G. Bouwman, *Analysis of spin-echo small-angle neutron scattering measurements,* J. Appl. Crystallogr. **41**, 868 (2008).

[23] A. P. Kaestner, S. Hartmann, G. Kuhne, G. Frei, C. Grunzweig, L. Josic, F. Schmid, and E. H. Lehmann, *The icon beamline - a facility for cold neutron imaging at sinq,* NIMA **659**, 387 (2011).

[24] J. Schelten and W. Schmatz, *Multiple-scattering treatment for small-angle scattering problems,* J. Appl. Crystallogr. **13**, 385 (1980).

[25] F. Balima, V. Pischedda, S. Le Floch, A. Brulet, P. Lindner, L. Duclaux, and A. San-Miguel, *An in situ small angle neutron scattering study of expanded graphite under a uniaxial stress,* Carbon **57**, 460 (2013).

[26] A. P. Radlinski, E. Z. Radlinska, M. Agamalian, G. D. Wignall, P. Lindner, and O. G. Randl, *Fractal geometry of rocks,* Phys. Rev. Lett. **82**, 3078 (1999).

[27] M. T. Rekveldt, W. G. Bouwman, W. H. Kraan, O. Uca, S. V. Grigoriev, K. Habicht, and T. Keller, *Elastic neutron scattering measurements using larmor precession of polarized neutrons,* Neutron Spin Echo Spectroscopy: Basics, Trends and Applications **601**, 87 (2003).

[28] D. F. R. Mildner and P. L. Hall, *Small-angle scattering from porous solids with fractal geometry,* J. Phys. D: Appl. Phys **19**, 1535 (1986).

[29] P. W. Schmidt, *Small-angle scattering studies of disordered, porous and fractal systems,* J. Appl. Crystallogr. **24**, 414 (1991).

[30] H. D. Bale and P. W. Schmidt, *Small-angle x-ray-scattering investigation of submicroscopic porosity with fractal properties,* Phys. Rev. Lett. **53**, 596 (1984).

[31] J. Teixeira, *Small-angle scattering by fractal systems,* J. Appl. Crystallogr. **21**, 781 (1988).

[32] B. B. Mandelbrot, *The fractal geometry of nature* (Freeman, New York, 1983).

[33] A. P. Pentland, *Fractal-based description of natural scenes,* IEEE Transactions on Pattern Analysis and Machine Intelligence **6**, 661 (1984).

[34] M. Beech, *The projection of fractal objects,* Astrophys. Space Sci. **192**, 103 (1992).

[35] H. W. Wang, L. M. Anovitz, A. Burg, D. R. Cole, L. F. Allard, A. J. Jackson, A. G. Stack, and G. Rother, *Multi-scale characterization of pore evolution in a combustion metamorphic complex, hatrurim basin, israel: Combining (ultra) small-angle neutron scattering and image analysis,* Geochim. Cosmochim. Acta **121**, 339 (2013).

[36] F. Balima, S. Le Floch, A. San-Miguel, P. Lindner, A. Brulet, L. Duclaux, and V. Pischedda, *Shear effects on expanded graphite under uniaxial pressure: An in situ small angle neutron scattering study,* Carbon **74**, 54 (2014).

[37] S. C. van der Marck, *Percolation thresholds and universal formulas,* Phys. Rev. E **55**, 1514 (1997).

[38] P. Pfeifer, F. Ehrburger-Dolle, T. P. Rieker, M. T. Gonzalez, W. P. Hoffman, M. Molina-Sabio, F. Rodriguez-Reinoso, P. W. Schmidt, and D. J. Voss, *Nearly space-filling fractal networks of carbon nanopores,* Phys. Rev. Lett. **88** (2002).

[39] Z. Mileeva, D. K. Ross, D. Wilkinson, S. M. King, T. A. Ryan, and H. Sharrock, *The use of small angle neutron scattering with contrast matching and variable adsorbate partial pressures in the study of porosity in activated carbons,* Carbon **50**, 5062 (2012).

[40] A. J. Allen, J. J. Thomas, and H. M. Jennings, *Composition and density of nanoscale calcium-silicate-hydrate in cement,* Nature Mat. **6**, 311 (2007).

8

APPENDIX: HANKEL TRANSFORMATION

8.1. FORMALISM OF HANKEL TRANSFORMATION

In Chapter 7, small angle neutron scattering techniques including SANS and SESANS have been used to investigate the structure of graphite, and the measured data are interpreted by a fractal model. Actually SESANS and SANS data can be directly related and it is possible to transform one into the other. Here we first provide the formalism of the transformation, and the equations are rewritten after [1].

SESANS measures the projection of correlation function $G'(z)$ through the spin echo polarization $P(z)$, which is given by:

$$P(z) = e^{\frac{t\lambda^2}{2\pi}(G'(z) - G'(0))},$$
(8.1)

and $G'(z)$ is the Hankel transformation of $I(Q)$ the cross section measured in a conventional SANS experiment as a function of the scattering vector Q given by:

$$G'(z) = \int_0^\infty J_0(Qz) I(Q) Q dQ$$
(8.2)

and

$$G'(0) = \int_0^\infty I(Q) Q dQ.$$
(8.3)

The normalized projection of correlation function $G(z)$ is thus given by:

$$G(z) = G'(z)/G'(0).$$
(8.4)

In above equations, z is the spin echo length at which the correlation function is probed, λ the wavelength of the neutron beam, t the sample thickness, and J_0 a zeroth-order Bessel function of the first kind. The inverse transformation is:

$$I(Q) = \int_0^\infty J_0(Qz) G'(z) z dz$$
(8.5)

8.2. Structural models: the single sphere model and the random two phase media model

By the use of the above equations, the Hankel transformation between $I(Q)$ and $G(z)$ is performed for two structural models, known as the single sphere model and random two phase media model.

The single sphere model

For a single sphere with a radius R, $I(Q)$ is given by [2]:

$$I(Q) = \frac{4}{3}\pi R^3 (\Delta\rho)^2 \left[\frac{3(\sin(QR) - QR\cos(QR))}{(QR)^3} \right]^2, \tag{8.6}$$

where $(\Delta\rho)^2$ is the neutron scattering length density contrast between two phases. The corresponding normalized projection of correlation function $G(z)$ is given by [1]:

$$G(z) = \Re \left[\sqrt{1 - \left(\frac{z}{2R}\right)^2} \left(1 + \frac{1}{2}\left(\frac{z}{2R}\right)^2\right) + 2\left(\frac{z}{2R}\right)^2 \left(1 - \frac{z}{4R}\right)^2 \ln\left(\frac{z/R}{2 + \sqrt{4 - (z/R)^2}}\right) \right] \tag{8.7}$$

where $\Re$ gives the real part.

The random two phase media model

For a random two phase media model, $I(Q)$ is given by [1]:

$$I(Q) = \frac{4a^3\pi(1 + 2H)(\Delta\rho)^2}{(1 + (Qa)^2)^{(\frac{3}{2} + H)}} \tag{8.8}$$

and the normalized projection of correlation function $G(z)$ is given by:

$$G(z) = \frac{2}{\Gamma(H + 1/2)} \left(\frac{z}{2a}\right)^{H + 1/2} K_{H + 1/2}\left(\frac{z}{a}\right) \tag{8.9}$$

where $(\Delta\rho)^2$ is the neutron scattering length density contrast between two phases, a represents a characteristic size of the random inhomogeneities, H is the so called Hurst exponent, which is a measure for the space filling capacity of the structure, Γ is the Gamma function, and $K_n(x)$ is the Modified Bessel function of the second kind.

For the sake of simplicity, the Hankel transformation between $I(Q)$ and $G(z)$ for the two models was performed by assuming $(\Delta\rho)^2 = 1$ with unit of length to the power of -4.

8.3. Simulations of Hankel transformation

Fig. 8.1 and 8.2 show the calculated Hankel transformation between $G(z)$ and $I(Q)$ for the single sphere model with radius $R = 10$ μm and for the random two phase media model with $a = 3$ μm and $H = 0.2$. Fig. 8.1(a) and 8.2(a) show that for both models $I(Q)$ can be transformed into $G(z)$ properly by combing Eq. 8.2, 8.3 and 8.4. Fig. 8.1(b) and
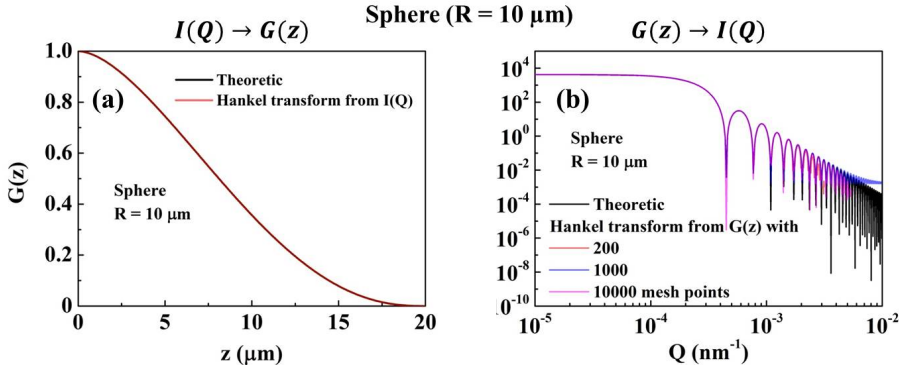
Figure 8.1: (a) $G(z)$ for the single sphere model with $R = 10$ μm from Eq. 8.7 (black line) and the Hankel transform of $I(Q)$ by combing Eq. 8.6 with 8.2, 8.3 and 8.4 (red line); (b) $I(Q)$ from Eq. 8.6 (black line) and the Hankel transform of $G(z)$ by combing Eq. 8.7 with 8.3, 8.4 and 8.5 (color lines). The number of mesh points of $G(z)$ influences the quality of the Hankel transformation, and this effect is evaluated by taking 200, 1000, and 10000 mesh points for $G(z)$.

8.2(b) show that the transformation from $G(z)$ to $I(Q)$ by combing Eq. 8.3, 8.4 and 8.5 is validated at low Q range, however, deviations from the theoretical $I(Q)$ can be clearly observed at high Q range. We note that increasing the number of mesh points in $G(z)$ can only improve the quality of the transformation in a limited way.
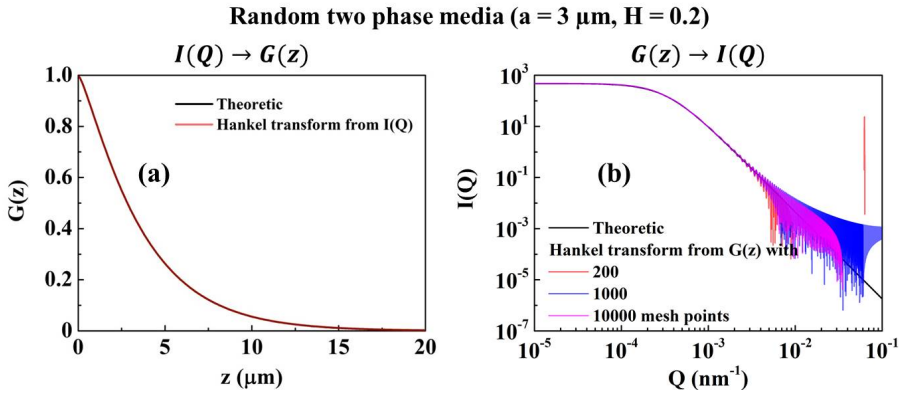

Figure 8.2: (a) $G(z)$ for the random two phase media model with $a = 3$ μm and $H = 0.2$ from Eq. 8.9 (black line) and the Hankel transform of $I(Q)$ by combing Eq. 8.8 with 8.2, 8.3 and 8.4 (red line); (b) $I(Q)$ from Eq. 8.8 (black line) and the Hankel transform of $G(z)$ by combing Eq. 8.9 with 8.3, 8.4 and 8.5 (color lines). The number of mesh points of $G(z)$ influences the quality of the Hankel transformation, and this effect is evaluated by taking 200, 1000, and 10000 mesh points for $G(z)$.

To examine possible limitations of the Hankel transform from $G(z)$ to $I(Q)$, $G(z)$ of the random two phase media model with different values of a ($a = 1, 3, 5, 10, 20$) is calculated through Eq. 8.9 (see Fig.8.3). Next the corresponding Hankel transformation using Eq. 8.3, 8.4 and 8.5 are compared with the theoretic $I(Q)$, which is calculated through Eq.
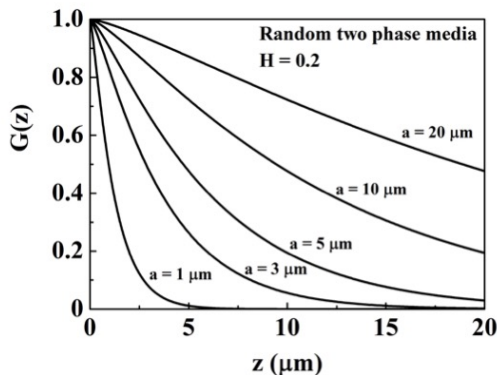
Figure 8.3: $G(z)$ for the random two phase media model ($H = 0.2$) with $a = 1, 3, 5, 10, 20\ \mu m$.

8.8. The results shown in Fig. 8.4) suggest that the validity of the Hankel transformation from $G(z)$ to $I(Q)$ depends on the value of a. As a increases, the transformation results are only reliable in a limited low Q range. As illustrated in Fig. 8.3, it is concluded that the Hankel transformation from $G(z)$ to $I(Q)$ is only valid if $G(z)$ approaches to 0 in the probe range of the SESANS experiment (30 nm $\leq z \leq$ 20 μm).
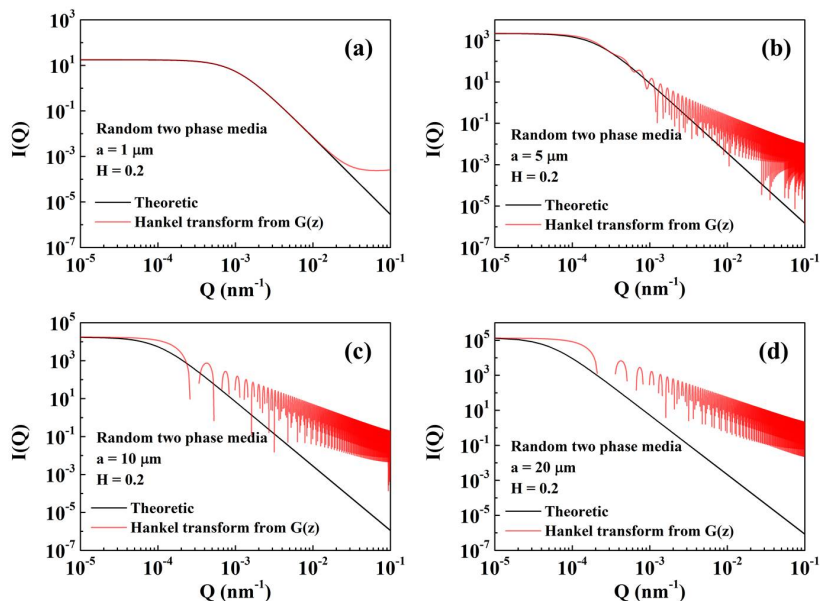
Figure 8.4: Theoretic $I(Q)$ from Eq. 8.8 (black lines) and the Hankel transform of $G(z)$ by combing Eq. 8.9 with 8.3, 8.4 and 8.5 (red lines) for the random two phase media model ($H = 0.2$) with (a) $a = 1\ \mu m$, (b) $a = 5\ \mu m$, (c) $a = 10\ \mu m$, and (d) $a = 20\ \mu m$. The case of $a = 3\ \mu m$ can be found in Fig. 8.2(b).
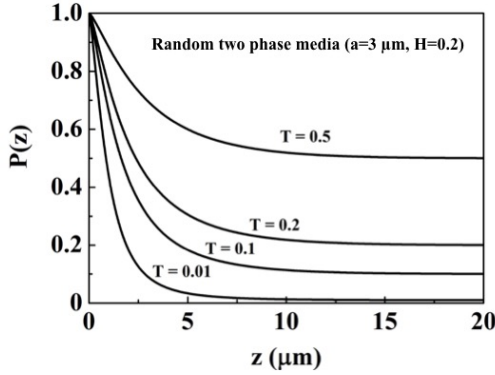
Figure 8.5: $G(z)$ for the random two phase media model ($H = 0.2$) with $a = 1, 3, 5, 10, 20 \ \mu$m.

In a SESANS experiment, when $G(z) \to 0$, it can be deduced from Eq. 8.1 and 8.4 that the measured polarisation $P(z) \to e^{-\frac{t\lambda^2}{2\pi} G'(0)} = T$, where T is the so called saturation level indicating the fraction of neutrons that does not scatter when traversing the sample. Thus the relationship between measured $P(z)$ and $G(z)$ can be formulated as:

$$G(z) = 1 - \frac{\ln(P(z))}{\ln(T)} \tag{8.10}$$

Fig. 8.5 shows $P(z)$ calculated from Eq. 8.10 for a random two phase media ($a = 1 \ \mu$m and $H = 0.2$) with different values of T. It is clear that $P(z)$ saturates at the value of T.
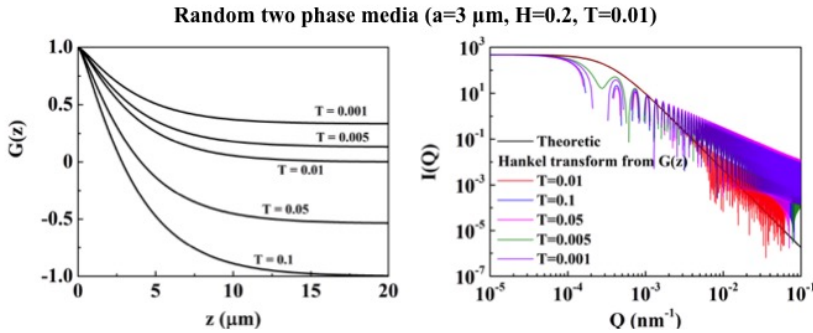
Figure 8.6: (a) $G(z)$ calculated from measured $P(z)$ in SESANS through Eq. 8.10 for the random two phase media model ($H = 0.2$, $a = 3 \ \mu$m and $T = 0.01$) by taking different values of T. (b) Hankel transform of $G(z)$ given in (a) compared with the theoretic $I(Q)$.

As mentioned above, the Hankel transformation is only valid when $G(z)$ obtained from SESANS measurement approaches at 0 in the probe range. Therefore, it is necessary that the measured $P(z)$ saturates at a specific value of T. However, in real measurements if T is very small, the precise value of T is difficult to determine due to the

experimental uncertainties. A wrong value of T will lead to inaccurate $G(z)$ and consequently the resulting $I(Q)$ from Hankel transform is unreliable. To investigate this effect, the case of the random two phase media model with $T = 0.01$ is studied, of which $P(z)$ is shown in Fig. 8.5. $G(z)$ is simulated through Eq. 8.10 by assuming different values of T, as shown in Fig. 8.6(a). Next the Hankel transform is performed on each $G(z)$, and the obtained $I(Q)$ is compared with the theoretic curve, as shown in Fig. 8.6(b). It is obvious that only the Hankel transformation of $G(z)$ with the "real" value of T is valid.

In summary, the Hankel transform between SANS and SESANS measurements has been studied, and the simulation results reveal the limitations when converting a SESANS data to SANS data. Only when the measured polarisation $P(z)$ in a SESANS experiment saturates at a specific value T that can be determined precisely, the Hankel transformation from $G(z)$ to $I(Q)$ is valid.

8.4. HANKEL TRANSFORMATION ON REAL DATA

In this work, it has been attempted to convert the SESANS data for the graphite samples to a conventional SANS measurement through the Hankel transform. Fig. 8.7 displays the SESANS data for RID and PCEA graphite samples. For the RID sample, the measured $P(z)$ decreases and approaches to 0 as the spin echo length z increases. The Hankel transformation was performed on $G(z)$ calculated from $P(z)$ by assuming $T = 0.02$ (since T is hard to determine from the measurement). The resulting curve shown in Fig. 8.8 is plotted together with SANS and imaging data and the fractal model from Chapter 7. The results show that the transformed SESANS data are not valid because the measured $P(z)$ does not saturate at a specific value in the probed range. On the other hand, the measured $P(z)$ of the PCEA sample seems to saturate at $T = 0.14$, and the transformed SESANS data are close to the model, as shown in Fig. 8.9.
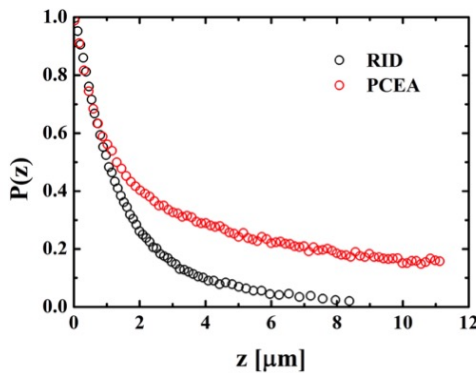
Figure 8.7: SESANS measurements of the RID and PCEA graphite samples.
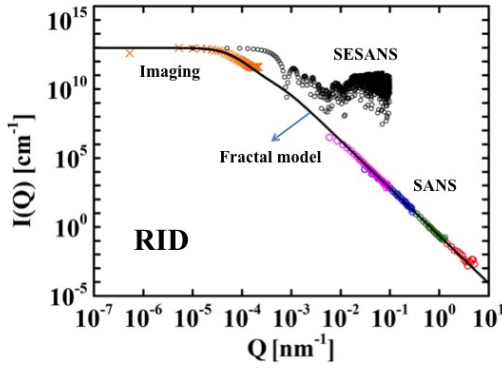
Figure 8.8: Scattering curves for the RID graphite sample. The SESANS data are obtained by performing the Hankel transform on the measured $P(z)$ with $T = 0.02$.
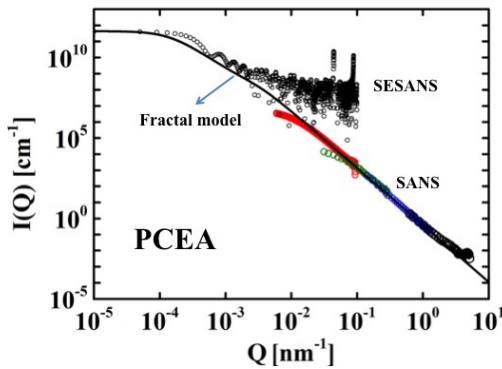
Figure 8.9: Scattering curves for the PCEA graphite sample. The SESANS data are obtained by performing the Hankel transform on the measured $P(z)$ with $T = 0.14$.

REFERENCES

[1] R. Andersson, L. F. van Heijkamp, I. M. de Schepper, and W. G. Bouwman, *Analysis of spin-echo small-angle neutron scattering measurements,* J. Appl. Crystallogr. **41**, 868 (2008).

[2] A. J. Jackson, *Introduction to small-angle neutron scattering and neutron reflectometry,* (2008).

SUMMARY

Graphite is an important moderator material in nuclear reactors due to its high purity, thermal stability, ease of machining and relative low cost. During the reactor operations, fast neutrons induce changes in the dimensional, mechanical and physical properties of the graphite, which are determined by the its structure. A comprehensive characterization of the structure is thus needed to predict the changes for long-term safe operation of the reactors. For this purpose, several techniques such as X-ray/neutron diffraction, (spin echo) small angle neutron scattering and neutron imaging have been used to achieve an investigation on the graphite structure from atomic level to macro length scale.

The atomic structure of graphite has been studied by X-ray/neutron diffraction (Chapter 4-6). The interpretation of the diffraction patterns for graphites is not trivial, because the inherent disorder and anisotropy of the structure significantly affect the shape and intensities of the reflections. For this reason, the Rietveld refinement, which is the standard method to analyse the diffraction data, cannot reproduce the diffraction profiles properly. To overcome this limitation, in this work a structural model proposed by Shi has been applied. This approach has considered two models: a two-layer model for graphitic carbons and a single-layer model for disordered carbons. Both models involve several parameters that are incorporated in the refinement program CARBONXS for reproducing the diffraction patterns of carbon materials. Besides the basic average lattice constants $\langle a \rangle$ and $\langle d_{002} \rangle$, the approach introduces two different characteristic lengths, one along the c-axis L_c and the other in the basal plane L_a, for quantifying the volumes over which X-rays/neutrons scatter coherently. The stacking faults and turbostratic disorder in the structure are taken into account by introducing two parameters, P_{RS} for the probability of the stacking faults with random shift between adjacent layers (turbostratic disorders), and P_{3R} for the probability of the ABC stacking faults (only in the two-layer model). These stacking faults induce fluctuations in the local interlayer spacing which are characterized by a parameter σ corresponding to the strains along the c-axis. All these parameters are refined by performing a least-squares fit between the measured and calculated diffraction patterns.

The two-layer model and program CARBONXS provide a significant improvement in fitting the X-ray diffraction patterns of virgin (nuclear) graphite samples compared with the standard Reitveld refinement. The results show that $\langle d_{002} \rangle$ is the essential indicator of the perfection/graphitization degree of the structure. The smaller $\langle d_{002} \rangle$ the larger coherent lengths L_c and L_a, which are a measure of the boundaries of coherent regions thus indicating the disorder in the microstructure. The value of $\langle d_{002} \rangle$ for nuclear graphites is found to be close to 3.360 Å, which is slightly larger than the value for a perfect graphite crystal 3.354 Å. This indeed implies that nuclear graphites are still highly disordered despite the fact that they are manufactured in a very high temperature (2600-3000°). In addition to 15-25% random shift P_{RS} and about 7% ABC stacking faults P_{3R},

the standard deviation of interlayer spacing fluctuations $\sigma \gg \langle d_{002} \rangle - 3.354$, indicating other disorder in the graphite structure, such as dislocations, crosslinks, vacancies and interstitial defects. In particular, a generic behaviour illustrating the relation between $\langle d_{002} \rangle$ and P_{RS} has been validated for all graphite and graphitic carbons.

With Shi's approach, the neutron irradiation effects on the structure of graphite has been investigated. The XRD patterns of both virgin and low dose (~ 1.3 and ~ 2.2 dpa), high temperature (750°) irradiated graphites were analysed by both the two-layer and single-layer models. The results show that the structure of the graphite samples can be described by both models, however, on the basis of the overall agreement between the fits and measurements, the two-layer model provides superior performance in the case of low dose irradiated samples studied in this work. The refined parameters for the two-layer model have been reviewed for revealing the neutron irradiation effects. The results show that for the lattice constants, $\langle a \rangle$ remains unchanged while $\langle d_{002} \rangle$ increases by ~0.5% and seems to approaches saturation at ~ 2.2 dpa. The increase of $\langle d_{002} \rangle$ is attributed to the interstitials cause by the atom displacements during irradiation. Up to the dose of ~1.5 dpa, L_a decreases because the graphite lattice of coherent regions tends to lose ordering in the basal plane, which is attributed to the induced in-plane defects, as well as the breaking, bending and displacement of the basal planes. The comparison of the relative changes of $\langle d_{002} \rangle$ and L_c indicates that the number of layers in the coherent region rises, which is attributed by two possible causes: (1) the formation of interstitial dislocation loops and/or (2) the closing of micro-cracks between slightly disoriented coherent regions. However, when the irradiation dose increases from ~1.5 to ~2.2 dpa, L_c starts to decrease, which indicates the fragmentation of the coherent regions into smaller ones. These results are in good agreement with previous observations from electron microscopy. On the other hand, the stacking order of the layers within the coherent regions is deteriorated by the neutron irradiation, indicated by the increase of P_{RS} and the decrease of P_{3R}. Additionally, the results show that the relation between $\langle d_{002} \rangle$ and P_{RS}, which is validated for non-irradiated graphites and graphitic carbons, cannot be applied for irradiated graphite samples. The average interlayer spacing cannot be described by the probability for the random stacking faults only, which indicates the presence of other types of disorder, e.g dislocation loops or the bending of the basal planes.

To complement and verify the XRD results, neutron diffraction experiments have been performed on the virgin graphites. In this work the difference in the structure of powder and bulk samples has been also studied to meet the interest of investigating the graphite dust formed during the operation of Pebble Bed Reactor. To analyse the measured neutron diffraction patterns, Shi's approach was also applied. For this purpose, several modifications have been made on the program CARBONXS to convert it from an X-ray specific to a neutron specific. In addition, the instrumental resolution of neutron diffractometer has been successfully included in analysis. Compared with X-ray diffraction, due to the absence of the influence of beam absorption and dual-wavelength, neutron diffraction produces more symmetric Bragg peaks that can be reproduced by Shi's model perfectly, thus leading to more reliable structural parameters. The results show that the structure of powder samples is deteriorated when scrapping the bulk material, indicated by the smaller coherent lengths and more stacking faults.

The investigation on the structure of graphite has been extended to micro and macro

length scales by combining other neutron techniques, such as small angle neutron scattering (SANS), spin echo SANS (SESANS) and neutron imaging (Chapter 7). In these measurements, the contrast arises from the difference in the neutron scattering/absorption cross section of pores (cracks) and carbon matrix. The power law behaviour has been observed in the data of SANS and neutron imaging, indicating a fractal structure (both surface and mass) of the pores. To interpret the experimental findings quantitatively, a fractal model has been applied to fit the data from all techniques. The obtained high quality of the fits and consistent parameters reveal a global picture of the fractal microstructure of graphite over an extraordinary large range of length scales of 6 orders of magnitude ($\sim$0.6 nm $\leq 2\pi/Q \leq$ 0.6 mm). To be specific, the pore structure consists of many pore-building blocks, which characterize the network of the pore clusters with a mass fractal property at the length scale above the size of the primary block. Moreover, the pore building block itself is bounded by a rough surface with fractal morphology. Thus in this study, two characteristic lengths ℓ and ξ have been quantified: ℓ marks the cross-over between mass and surface fractal scattering, and is proposed to be the cross-over between cracks (small and in the filler particles) and micropores (formed by gas evolution during manufacturing); ξ is a cut-off length indicating the average diameter for the pore clusters. In addition, the measured surface and mass fractal dimensions are both very close to 2.5, a value found for percolating clusters and fractured ranked surfaces in 3D.

In summary, the combination of several X-ray and neutron techniques leads to new insights in the structure of graphite. The methodology used in this work is promising for investigating irradiated graphites, which will certainly lead to a better understanding of the structural changes and the resulting modifications of the physical properties. In addition, the approach can be applied to the investigation of other complex systems with a hierarchy of length scales such as biological materials, concrete and rocks, materials for CO_2 sequestration, Li batteries, fuel cells or solar cells.

SAMENVATTING

Grafiet is een belangrijk materiaal voor moderatoren in kernreactoren van wege zijn hoge zuiverheid, thermische stabiliteit, eenvoudige bewerkbaarheid en betrekkelijk lage prijs. Gedurende het bedrijf van de reactor veroorzaken snelle neutronen veranderingen in de afmetingen en de mechanische en natuurkundige eigenschappen van het grafiet, die door zijn structuur bepaald worden. Een veelzijdige karakterisering van de structuur is daarom nodig om de veranderingen te voorspellen teneinde een langdurig veilig functioneren van de reactoren te bereiken. Voor dit doel zijn verscheidene technieken zoals Röntgen/neutronenverstrooiing, (spin echo) kleine hoek neutronenverstrooiing en neutronentransmissieafbeelding gebruikt om te komen tot een onderzoek van de grafietstructuur vanaf atomair niveau tot op macroscopische lengteschalen.

De atomaire structuur van grafiet is bestudeerd met Röntgen/neutronenverstrooiing (Hoofdstuk 4-6). De interpretatie van de verstrooiingspatronen is niet triviaal voor grafietmaterialen, omdat de inherente wanorde en anisotropie van de structuur de vorm en intensiteiten van de reflecties significant beïnvloeden. Om deze reden kan de Rietveldverfijning, wat de standaard methode is om verstrooiingsdata te analyseren, de diffractieprofielen niet goed genoeg reproduceren. Daarom is in dit werk een model voor de structuur toegepast, zoals voorgesteld door Shi. Bij deze benadering zijn twee modellen beschouwd: een twee-lagen model voor grafitische koolstof en een enkellaags model voor wanordelijk koolstof. Beide modellen vergen meerdere parameters die verwerkt zijn in het verfijningsprogramma CARBONXS om de verstrooiingspatronen van koolstofmaterialen te berekenen. Behalve de basale gemiddelde roosterconstanten $\langle a \rangle$ en $\langle d_{002} \rangle$ introduceert deze benadering twee verschillende karakteristieke lengten, de ene langs de c-as L_c en de andere in het grondvlak L_a, om de volumes te kwantificeren waarover Röntgenstralen of neutronen coherent verstrooien. De stapelfouten en turbostratische wanorde in de structuur worden in rekening gebracht door twee parameters te introduceren, P_{RS} voor de kans op een stapelfout met toevallige verschuiving tussen naburige lagen (turbostratische wanorde), en P_{3R} voor de kans op ABC stapelfouten (alleen in het twee-lagen model). Deze stapelfouten veroorzaken fluctuaties in de lokale afstand tussen lagen, die gekarakteriseerd worden door een parameter σ, die correspondeert met de spanningen langs de c-as. Al deze parameters worden verfijnd door een kleinste-kwadraten aanpassing tussen de gemeten en berekende verstrooiingspatronen toe te passen.

Het twee-lagen model en het programma CARBONXS bieden een significante verbetering in het fitten van de Röntgenverstrooiingspatronen van maagdelijke monsters van (nucleair) grafiet vergeleken met de standaard Rietveld verfijning. De resultaten tonen aan dat $\langle d_{002} \rangle$ de essentiele indicator is van de graad van perfectie of grafitisatie van de structuur. Hoe kleiner $\langle d_{002} \rangle$ hoe groter coherentielengten L_c and L_a, die een maat zijn voor de afmetingen van coherente gebieden en daarmee de mate van wanorde in de microstructuur aangeven. De waarde van $\langle d_{002} \rangle$ voor nucleaire grafieten wordt dicht bij

3.360 Å gevonden, wat iets groter is dan de waarde voor een perfect grafietkristal 3.354 Å. Dit impliceert inderdaad, dat nucleaire grafieten nog sterk wanordelijk zijn, ondanks dat zij gemaakt zijn bij een zeer hoge temperatuur (2600-3000°). Naast de 15-25% random verschuivingskans P_{RS} en ongeveer 7% ABC stapelfoutenkans P_{3R}, is de standaard afwijking in de fluctuaties in de afstand tussen lagen $\sigma \gg \langle d_{002}\rangle - 3.354$ een aanwijzing voor andere typen wanorde in de grafietstructuur, zoals dislocaties, bindingen tussen de lagen, vacatures en interstitielen. In het bijzonder is een generiek gedrag, dat de relatie tussen $\langle d_{002}\rangle$ en P_{RS} illustreert, geldig bevonden voor alle grafiet en grafitische koolstof.

Met Shi's aanpak zijn de effecten van neutronenbestraling op the structuur van grafiet onderzocht. De XRD patronen van zowel maagdelijke als met lage dosis (~ 1.3 en ~ 2.2 dpa) op hoge temperatuur (750°) bestraalde grafieten werden geanalyseerd met zowel het twee-lagen als het enkele-laagsmodel. De resultaten tonen, dat de structuur van de grafietmonsters beschreven kan worden door beide modellen. Echter, op basis van de algehele overeenkomst tussen de fits en de metingen presteert het twee-lagen model superieur in het geval van de met lage dosis bestraalde monsters, die in dit werk bestudeerd werden. De verfijnde parameters voor het twee-lagen model zijn onderzocht om te bekijken of zij de effecten van neutronenbestraling zichtbaar maken. De resultaten laten zien, dat de roosterconstanten $\langle a\rangle$ onveranderd blijven terwijl $\langle d_{002}\rangle$ toeneemt met ~0.5% en verzadiging lijkt te bereiken bij ~ 2.2 dpa. De toename van $\langle d_{002}\rangle$ wordt toegeschreven aan de interstitielen veroorzaakt door de verplaatsing van atomen tijdens de bestraling. Tot een dosis van ~1.5 dpa neemt L_a af, omdat het grafietrooster van coherente gebieden neigt de ordening in het grondvlak te verliezen, wat wordt toegeschreven aan de geinduceerde defecten in het vlak, evenals aan het breken, buigen en verschuiven van de grondvlakken. Vergelijking van de relatieve veranderingen van $\langle d_{002}\rangle$ en L_c geeft aan, dat het aantal lagen in de coherente gebieden toeneemt, wat wordt toegeschreven aan twee mogelijke oorzaken: (1) de vorming van interstitiele dislocatielussen en/of (2) het sluiten van microscheuren tussen coherente gebieden met enigszins afwijkende orientatie. Wanneer de bestralingsdosis echter toeneemt van ~1.5 tot ~2.2 dpa, begint L_c af te nemen, wat wijst op fragmentatie van de coherente gebieden in kleinere gebieden. Deze resultaten zijn in goede overeenkomst met eerdere waarnemingen met elektronenmicroscopie. Aan de andere kant wordt de stapelingsordening van de lagen binnen de coherente gebieden slechter door de neutronenbestraling, zoals aangegeven door de toename van P_{RS} en de afname van P_{3R}. Bovendien laten de resultaten zien, dat de relatie tussen $\langle d_{002}\rangle$ en P_{RS}, die geldt voor onbestraalde grafieten en grafitische koolstof, niet toegepast kan worden op bestraalde grafietmonsters. De gemiddelde afstand tussen lagen kan niet beschreven worden door de kans op stapelfouten alleen, wat wijst op de aanwezigheid van andere manieren om de ordening te breken, b.v. dislocatielussen of buiging in de grondvlakken.

Om de XRD resultaten aan te vullen en te verifieren zijn neutronverstrooiingsexperimenten gedaan aan de maagdelijke grafieten. Hierbij is het verschil in structuur tussen poeder en bulkmonsters ook bestudeerd om het belang te bepalen van onderzoek van het grafietstof, dat wordt gevormd gedurende de werking van "Pebble Bed"reactoren. Om de gemeten neutronenverstrooiingspatronen te analyseren werd weer Shi's aanpak gebruikt. Voor dit doel zijn verscheidene wijzigingen aangebracht in het programma CARBONXS om het te converteren van Röntgenstralingspecifiek tot neutronenspecifiek.

Bovendien is de instrumentele resolutie van de neutronendiffractometer in de analyse opgenomen. In vergelijking met Röntgenverstrooiing , dankzij de afwezigheid van de invloed van bundelabsorptie en een tweede golflengte, produceert neutronenverstrooiing meer symmetrische Bragg pieken, die perfect door Shi's model gereproduceerd kunnen worden, daarmee leidend tot betrouwbaarder structuurparameters. De resultaten laten zien, dat de structuur van poedermonsters verslechterd wanneer het van het bulkmateriaal afgeschraapt wordt, zoals blijkt uit de kortere coherentielengten en de toename van stapelfouten.

Het onderzoek naar de structuur van grafiet is uitgebreid naar micro- en macrolengteschalen door het te combineren met andere neutronentechnieken, zoals kleinehoek neutronenverstrooiing (SANS), spin-echo SANS (SESANS) en neutronenbeeldvorming (Hoofdstuk 7). In deze metingen ontstaat contrast door het verschil in neutronenverstrooiing/absorptie werkzame doorsnede van poriën (scheuren) en de koolstof matrix. Machtwetgedrag is waargenomen in de data van SANS en neutronenbeeldvorming, wijzend op een fractale structuur (zowel oppervlak als volume) van de poriën. Om de experimentele bevindingen kwantitatief te interpreteren is een fractaal model toegepast om de data van alle technieken te fitten. De verkregen hoge kwaliteit van de fits en de consistente parameters onthullen een globaal beeld van de fractale microstructuur van grafiet over een buitengewoon groot bereik aan lengte schalen van 6 ordes van grootte ($\sim$0.6 nm $\leq 2\pi/Q \leq$ 0.6 mm). Om precies te zijn bestaat de poriestructuur uit veel porievormende bouwstenen, die het netwerk van porieclusters karakteriseren met een volumefractaal op lengteschalen groter dan de afmeting van het primaire blok. Bovendien wordt de poriebouwsteen zelf begrensd door een ruw oppervlak met fractale morfologie. Zo zijn in dit onderzoek twee karakteristieke lengtes ℓ en ξ gekwantificeerd: ℓ markeert de overgang tussen volume- en oppervlakfractaalverstrooiing en wordt voorgesteld, dat dit de overgang tussen scheuren (klein en in de vullingsdeeltjes) en microporiën (gevormd door gasontwikkeling gedurende fabricage) is; ξ is een afkaplengte die de gemiddelde diameter van de porieclusters aangeeft. Bovendien liggen de gemeten oppervlak- en volumefractale dimensies beide dicht bij 2.5, een waarde gevonden voor percolerende clusters en breukvlakken in 3D.

Resumerend, de combinatie van verschillende Röntgen- en neutronentechnieken leidt tot nieuwe inzichten in de structuur van grafiet. De methodologie, die in dit werk gebruikt is, belooft veel voor het onderzoek van bestraald grafiet, wat zeker zal leiden tot een beter begrip van de structurele veranderingen en de resulterende modificaties van de fysische eigenschappen. Bovendien kan de aanpak toegepast worden in het onderzoek van andere complexe systemen met een hierarchie aan lengteschalen zoals biologische materialen, beton en gesteente, materialen om CO_2 vast te leggen, Li batterijen, brandstofcellen en zonnecellen.

ACKNOWLEDGEMENTS

First of all, I would like to thank my promotor, Prof. dr. C. Pappas. She offered me the opportunity to come to Delft for pursuing my PhD degree. I thank her not only for her guidances that helped shape this work, but also for her concern on my daily life and my future. I am especially grateful to my co-promotors Dr. W.G. Bouwman and Dr. H. Schut for their great help in the development of this research. As my daily supervisor, Wim has shown his concern for me and always been supportive in every respect. I thank him for his encouragement and appreciate the innumerable valuable discussions we had. Henk has always been greatly helpful in providing perceptive suggestions in the work discussions. He likes to draw all kinds sketches for recording, understanding and explaining almost everything, and I really enjoyed that every time. I would like to thank him for his help in revising the manuscript. To finish, I would also like to thank him for organizing my bachelor party.

I would like to express my gratitude to Prof. dr. Z. Li from Tsinghua University, where I obtained my bachelor and master degrees. My research was performed in the frame of a cooperation project between TU Delft and Tsinghua, and Prof. Li has been in a sense my supervisor in China. I thank him for his help during my stay in Tsinghua and for sharing his experience in both work and life.

This research work involved a large number of experiments and extensive data analysis that would not have been accomplished without the contribution and support of many colleagues. I would like to thank Prof. Paul Mummery, Dr. Maureen Haverty, and Prof. Tadashi Maruyama for providing us some of the graphite samples, Jan de Roode and Anton Lefering for their kind help on the sample preparation, Michel Steenvoorden and Kees Goubitz for the experimental support on the X-ray diffraction measurements, Marnix Wagemaker for his help on the GSAS refinement program. I would also like to thank Florence Porcher for her help with the neutron diffraction measurements as well as for driving me to LLB everyday when I was in Saclay, Lambert van Eijck, Jacques Jestin and Sylvain Desert for their help on the small angle neutron scattering measurements and for the discussions on the data reduction, Chris Duif for his help on the spin-echo small angle neutron scattering and Stefan Hartmann for his support for the neutron imaging/tomography experiments. I would also like to thank Annie Brulet, Lucas van Vliet, Niels van Dijk and Ad van Well for enlightening discussions on the data analysis

and interpretation. Thanks to Jeroen Plomp, Wicher Kraan, Theo Rekveldt, Ignatz de Schepper and Ekkes Brück for sharing their valuable comments on this research during the work discussions.

A special thanks goes to Jouke Heringa, who not only provided technical support on my computers, MATLAB or Fortran, but also helped me read numerous Dutch letters, make phone calls or fill forms. I also thank him for helping translate the summary of my thesis from English to Dutch.

I am also grateful to the secretaries Nicole, Ilse and Trudy for their administrative support, especially Nicole for arranging the paper work when I came to Delft and for finding me a place to live when I first arrived. I also would like to thank all other colleagues of the NPM2 and FAME groups for the open and enjoyable working atmosphere, which I really appreciated.

Finally, I would like to thank my friends with whom I shared great moments of my life during these years in Delft, Yongjia Li, Haiqiang Wang, Yili Mo, Xinyuan Mao, Ke Tao, Zhijie Ren, Hao Cui, Ping Liu. I would also like to express my sincere gratitude to my roommates Tianshi Lu and Yanqing Hou. We shared a lot of fun, happiness and good time together and became so good friends. A special thanks goes to Xiaoyu Zhang, who is a trusted friend forever.

Last but not the least, I would like to express my gratitude to my family, parents, grandparents, who have been a constant source of love, concern, support and strength all these years. A special thanks goes to my wife, Shan Shen, for her love, patience and understanding.

LIST OF PUBLICATIONS

PUBLICATIONS RELATED TO THIS THESIS

- **Z. Zhou**, W.G. Bouwman, H. Schut, T.O. van Staveren, M.C.R. Heijna, C.Pappas, *Influence of neutron irradiation on the microstructure of nuclear graphite: An X-ray diffraction study*, in preparation. (Chapter 5)

- **Zhou Zhou**, Wim G Bouwman, Henk Schut, Sylvain Desert, Jacques Jestin, Stefan Hartmann, Catherine Pappas, *From nanopores to macropores: Fractal morphology of graphite*, Carbon 96, 541 (2016). (Chapter 7)

- **Z. Zhou**, W.G. Bouwman, H. Schut, C. Pappas, *Interpretation of X-ray diffraction patterns of (nuclear) graphite*, Carbon 69, 17 (2014). (Chapter 4)

OTHER PUBLICATIONS

- Z. Hu, Z. Li, **Z. Zhou**, C. Shi, H. Schut, C. Pappas, *Positron and thermal desorption studies on He ion implanted nuclear graphite*, Journal of Physics: Conference Series 505, 012014 (2014).

- Xiaodong Wu, **Zhou Zhou**, Duan Weng, Bin Wang, *Effects of tungsten oxide on the activity and thermal stability of a sulfate-derived titania supported platinum catalyst for propane oxidation*, Journal of Environmental Sciences 24, 458 (2012)

- Xiaodong Wu, Fan Lin, Lei Wang, Duan Weng, **Zhou Zhou**, *Preparation methods and thermal stability of Ba-Mn-Ce oxide catalyst for NOx-assisted soot oxidation*, Journal of Environmental Sciences 23, 1205 (2011)

- Xiaodong Wu, **Zhou Zhou**, Duan Weng, Fan Lin, *Role of stable nitrates stored on BaCoCe in soot catalytic oxidation*, Catalysis Communications 11, 749 (2010)

PRESENTATIONS

- *Combined fractal analysis of the structure of graphite from neutron imaging and small angle neutron scattering.* Zhou Zhou, Wim Bouwman, Henk Schut, Catherine Pappas, Sylvain Desert, Jacques Jestin, Stefan Hartmann
  The 10th World Conference on Neutron Radiography (WCNR-10), Grindelwald, Swizerland, October 5-10, 2014

- *Fractal structure of nuclear graphite from nm to mm: a neutron's view.* Zhou Zhou, Wim Bouwman, Henk Schut, Catherine Pappas, Sylvain Desert, Jacques Jestin, Stefan Hartmann
  The 15th International Nuclear Graphite Specialists (INGSM15), Hangzhou, China, September 15-18, 2014

- *Structure of nuclear graphite revealed by neutrons and X-rays: from atomic to macroscopic scales.* Zhou Zhou, Wim Bouwman, Henk Schut, Catherine Pappas, Florence Porcher, Sylvain Desert, Jacques Jestin, Maureen Haverty, Paul Mummery, Stefan Hartmann
  The 13th International Nuclear Graphite Specialists (INGSM13), Meitingen, Germany, September 23-26, 2012

CURRICULUM VITÆ

Zhou Zhou was born on January 12, 1987, in Shimen, Hunan Province, China. In 2005, after graduation from The First High School of Shimen, he attended Tsinghua University in Beijing, and majored at the School of Materials Science and Engineering. There he obtained his bachelor degree in 2009 on a thesis entitled *"Study on the preparation and sulphur resistance of Pt/ZrO$_2$-TiO$_2$ oxidation catalyst"*. He obtained his master degree in 2011 on a thesis entitled *"Study on modification of Pt/TiO$_2$ catalyst by WO$_3$ for propane oxidation"*. In August 2011 he moved to Delft, The Netherlands, to start his Doctoral study in the group of Neutron and Positron Methods in Materials (NPM2) at the Delft University of Technology. His research work focused on the investigation of the structure of (nuclear) graphite using X-ray and neutron techniques under the supervision of Prof. Dr. C. Pappas. The results of this research are presented in this thesis entitled *"The structure of (nuclear) graphite: from the atomic to the macro scales"*. At present, he is working within NPM2 as a postdoc on the development of a neutron imaging station.